PROCESSING OF HEAVY-RARE-EARTH-LEAN Nd-Fe-B PERMANENT MAGNETS FOR HIGH-TEMPERATURE APPLICATIONS

Matic Korent

Doctoral Dissertation
Jožef Stefan International Postgraduate School
Ljubljana, Slovenia

Supervisor: Dr. Kristina Žagar Soderžnik, Jožef Stefan Institute, Jamova cesta 39, 1000 Ljubljana, Slovenia
Co-Supervisor: Prof. Spomenka Kobe, Jožef Stefan Institute, Jamova cesta 39, 1000 Ljubljana, Slovenia

Evaluation Board:
Prof. Paul McGuiness, Chair, Institute of Metals and Technology, Ljubljana, Slovenia
Prof. Carlo Burkhardt, Member, Institute for Precious and Technology Metals, Pforzheim, Germany
Asst. Prof. Matej Komelj, Member, Jožef Stefan Institute, Ljubljana, Slovenia

MEDNARODNA PODIPLOMSKA ŠOLA JOŽEFA STEFANA
JOŽEF STEFAN INTERNATIONAL POSTGRADUATE SCHOOL

Matic Korent

PROCESSING OF HEAVY-RARE-EARTH-LEAN Nd-Fe-B PERMANENT MAGNETS FOR HIGH-TEMPERATURE APPLICATIONS

Doctoral Dissertation

PROCESIRANJE TRAJNIH Nd-Fe-B MAGNETOV Z NIZKO VSEBNOSTJO TEŽKIH REDKIH ZEMELJ ZA VISOKO-TEMPERATURNE APLIKACIJE

Doktorska disertacija

Supervisor: Dr. Kristina Žagar Soderžnik

Co-Supervisor: Prof. Spomenka Kobe

Ljubljana, Slovenia, December 2021

Acknowledgements

Firstly, I would like to thank both my supervisors, Dr. Kristina Žagar Soderžnik and Prof. Spomenka Kobe, for the guidance, help and support during my PhD study. Thank you for sharing your knowledge and experience with me and showing me a high level of scientific expertise.

During my PhD, I was given an opportunity to spend three months at National Institute of Magnetic Materials, in Tsukuba, Japan. I would like to thank Prof. Hono's group for the hospitality during my stay and for a wonderful experience since I have met successful and world-renowned scientists of Magnetic Society.

Thanks go also to magnetic group members of the Department for Nanostructured materials at the Jožef Stefan Institute. Especially in permanent magnet group meetings, I have learned a lot from presentations, comments and questions of my colleagues.

Special thanks also go to Dr. Marko Soderžnik for introducing me to the world of magnetism.

Last, but not least, I would like to express the highest gratitude and appreciation to my wife Anja, my family and friends for all the encouragement and support throughout my PhD study.

Abstract

Permanent magnets are materials that generate a magnetic field in free space without electricity or other external energy sources. They are essential components of modern technologies, used in many electrical devices. Nowadays, they are included in technology for renewable sources of energy, such as electrical vehicles, generators and wind turbines.

For such applications, Nd-Fe-B magnets are the most suitable choice due to their high energy product $(BH)_{max}$. The largest $(BH)_{max}$ value above 400 kJ/m^3 was reported for high-performance anisotropic Nd-Fe-B magnets. However, the coercivity at room temperature and its thermal stability is still a weak point of Nd-Fe-B magnets. To withstand high temperatures and demagnetization fields during the operation of a motor, the coercivity at room temperature must be improved. Adding heavy rare earths (HREs) such as Dy and/or Tb results in the formation of a high-anisotropy phase (HRE, $Nd)_2Fe_{14}B$ that leads to enhanced coercivity. The drawbacks of using HREs are reduced saturation magnetization, high price and risk of supply, since they are predominantly mined in China. Therefore, high-performance Nd-Fe-B magnets with a reduced amount of HREs or even without HREs needs to be considered.

In this thesis four different topics are introduced with one common denominator – melt-spun Nd-Fe-B ribbons. The first topic relates to a first-author paper entitled "Magnetic properties and microstructure evolution of hot-deformed Nd-Fe-B magnets produced by low-pressure spark-plasma sintering". In this work the hot-deformed Nd-Fe-B magnets are produced from commercial Nd-Fe-B ribbons. The spark-plasma-sintering technique is used as it enables a deformation process under low pressures at 40 MPa. The initial stages of the hot-deformed process are investigated by means of microstructural observations and magnetic measurements. Hot-deformed magnets with different deformation ratios are produced and their remanence dependence on the deformation ratios was investigated. In the initial stages of the hot-deformation process, the cone-like shape of the magnet is observed for the first time. In addition, at different regions of a cone-like hot-deformed magnet, various degrees of alignment of both the ribbons and the grains are detected. The experimental data are qualitatively interpreted in the frame of a simple Stoner-Wohlfarth model, which reveals reasonable magnetic properties while applying a low pressure.

In the second topic a newly developed, economically efficient method for processing rare-earth Nd-Fe-B magnets based on spark plasma sintering is presented in a first-author paper entitled "Toward Low-Energy Spark-Plasma Sintering of Hot-Deformed Nd-Fe-B magnets". This technique makes it possible to retain the technologically essential properties of the magnet by consuming about 30% of the energy, compared to the conventional spark-plasma-sintering process. A magnet with an anisotropic microstructure is fabricated from MQU-F commercial ribbons with a low energy consumption during the deformation process and compared to the conventionally prepared hot-deformed magnet, which consumed 3-times more energy. Both magnets are post-annealed at 650 °C for 120 min in a vacuum. After the post-annealing process, the low-energy processing (LEP) hot-deformed magnet shows a coercivity of 1327 kAm^{-1} and remanent magnetization of 1.27 T. In comparison, the high-energy processing (HEP) hot-deformed magnet had a coercivity of 1337 kAm^{-1}

and a remanent magnetization of 1.31 T. A complete microstructural characterization and detailed statistical analyses reveal a better texture orientation for the HEP hot-deformed magnet processed with a higher energy consumption, which is the main reason for the difference in the remanent magnetization between the two hot-deformed magnets. The results show that although the LEP hot-deformed magnet was processed with three times less energy being consumed than in a typical hot-deformation process, it still has only an 8% lower maximum energy product.

The third topic relates to a third first-author paper entitled "Significant coercivity enhancement of hot-deformed bulk magnets by two-step diffusion process using a minimal amount of Dy", where a two-step grain-boundary-diffusion process is implemented on a hot-deformed Nd-Fe-B magnet with the addition of a minimal amount of Dy. The coercivity of a 5.6-mm-thick Nd-Fe-B hot-deformed magnet was increased from 1.13 T to 2.5 T while maintaining a large remanent magnetization of 1.32 T using $Nd_{50}Dy_{30}Cu_{20}$ and $Nd_{80}Cu_{20}$ alloys for the first and second steps of the diffusion process, respectively. Only 0.45 wt.% of Dy was used in the high-coercivity bulk magnet which is only ≈10 % of that used in the conventional Dy-alloyed sintered magnets with a comparable coercivity. In addition to the high room-temperature value of coercivity, an excellent temperature coefficient of coercivity of –0.41 %/°C was realized in the final diffusion-processed hot-deformed magnet. Consequently, this work paves a way towards the development of bulk high-coercivity Dy-lean Nd-Fe-B magnets.

Last, but not least, the fourth topic presents an invention that relates to the improvement of the coercivity of a commercial magnetic melt-spun Nd-Fe-B ribbons with a small intergranular phase fraction and a process for the production of polymer-bonded magnets by the diffusion of a low-temperature eutectic alloy (Nd-Cu). The coercivity of the commercial Nd-Fe-B powder is not satisfactory for certain applications, while commercial powders for the fabrication of polymer-bonded magnets with high coercivity are significantly more expensive due to the added HRE. This invention presented the improvement of the magnetic properties (coercivity) of economically more favourable melt-spun Nd-Fe-B ribbons with a very small proportion of intergranular phase. The solution for coercivity enhancement was the diffusion of low-temperature-eutectic alloy (Nd-Cu), which resulted in a 15 % coercivity improvement of the final polymer-bonded magnet compared to that prepared from standard, low-cost, magnetic, melt-spun Nd-Fe-B ribbons.

Povzetek

Trajni magneti so materiali, ki ustvarjajo magnetno polje brez vira električne ali drugih oblik energije in so ključni sestavni element sodobnih električnih napravah. Danes so vključeni predvsem v obnovljivo tehnologijo, kot so električna vozila in generatorji za vetrne turbine.

Za zgoraj navedene aplikacije so magneti Nd-Fe-B najprimernejša izbira zaradi njihovih visokih vrednosti maksimalnih energijskih produktov $(BH)_{max}$. O največji vrednosti $(BH)_{max}$, več kot 400 kJ/m^3, so poročali pri visoko zmogljivih anizotropnih magnetih Nd-Fe-B. Največja pomanjkljivost teh magnetov sta nizka vrednost koercitivnosti pri sobni temperaturi in njena temperaturna stabilnost. Da bi bila vrednost koercitivnosti zadovoljiva pri povišanih temperaturah in visokih razmagnetilnih poljih med delovanjem motorja, je potrebno izboljšati njeno vrednost pri sobni temperaturi. Ena od možnosti je dodatek težkih redkih zemelj (HRE), kot sta Dy ali/in Tb, kar povzroči nastanek visoko anizotropne faze (HRE, Nd)$_2$Fe$_{14}$B, katere rezultat je povišana koercitivnost. Kljub izdatno povišani koercitivnosti, so pomanjkljivosti uporabe HRE zmanjšana vrednost magnetnega nasičenja, visoka cena in tvegana dobava, saj le te pretežno rudarijo na Kitajskem. Zato je potrebno razmišljati o procesiranju visokozmogljivih magnetov Nd-Fe-B z zmanjšano vsebnostjo težkih redkih zemelj ali celo brez dodatka težkih redkih zemelj.

V tej disertaciji so predstavljene štiri različne tematike s skupnim imenovalcem – ultra-hitro kaljeni magnetni trakci Nd-Fe-B. Prva tematika predstavlja članek s prvim avtorstvom z naslovom "Magnetic properties and microstructure evolution of hot-deformed Nd-Fe-B magnets produced by low-pressure spark-plasma sintering ". V tem članku so vroče deformirani magneti Nd-Fe-B pripravljeni iz komercialnih ultra-hitro kaljenih trakcev Nd-Fe-B. Uporabljena je metoda sintranja s sunkovnim tokom (SPS), ki omogoča izvajanje procesa deformacije pri nizkih tlakih (40 MPa). Začetne faze vroče deformiranega procesa so bile raziskane s pomočjo mikrostrukturnih opazovanj in magnetnih meritev. Vroče deformirani magneti so bili proizvedeni z različnimi deformacijskimi razmerji. Na ta način je bila raziskana odvisnost vrednosti remanence od deformacijskega razmerja. V začetnih fazah procesa vroče deformacije je bila opazna stožčasta oblika magneta. Poleg tega se v različnih regijah mikrostrukture takšnega magneta pojavijo različne stopnje poravnave tako trakcev kot zrn. Pridobljeni eksperimentalni podatki so bili interpretirani v okviru preprostega modela Stoner-Wohlfarth, ki razkriva dobre magnetne lastnosti pri uporabi nizkega tlaka.

V drugi tematiki je predstavljena na novo razvita ekonomsko učinkovita metoda za obdelavo magnetov redkih zemlj, Nd-Fe-B, ki temelji na sintranju s sunkovnim tokom in je predstavljena v članku z naslovom "Toward Low-Energy Spark-Plasma Sintering of Hot-Deformed Nd-Fe-B magnets". Ta tehnika omogoča ohranitev tehnološko bistvenih lastnosti proizvedenega magneta kljub temu, da se ob tem porabi približno 30% energije v primerjavi s klasičnim postopkom sintranja s sunkovnim tokom. Magnet z anizotropno mikrostrukturo je bil izdelan iz komercialnih trakov MQU-F z nizko porabo energije med procesom deformacije v primerjavi s konvencionalno pripravljenim vroče deformiranim magnetom, kjer se porabi trikrat več energije. Oba magneta sta bila naknadno termično obdelana pri

650 °C 120 minut v vakuumu. Po termični obdelavi je deformiran magnet pripravljen z nizko energijskim procesiranjem (LEP) izkazal koercitivnost 1327 kAm^{-1} (1.66 T) in remanentno magnetizacijo 1,27 T medtem, ko je magnet pripravljen z visoko energijskim procesiranjem (HEP) izkazal koercitivnost 1337 kAm^{-1} (1.67 T) in remanentno magnetizacijo 1,31 T. Celokupna mikrostrukturna karakterizacija in detajlna statistična analiza razkrivajo boljšo teksturo zrn vroče deformiranega magneta, procesiranega z večjo porabo energije, kar je glavni razlog za razliko v vrednosti remanentne magnetizacije med obema vroče deformiranima magnetoma. Rezultati kažejo, da čeprav je bil LEP vroče deformiran magnet procesiran s trikrat nižjo porabo energije, kot v konvencionalnem procesu vroče deformacije, ima še vedno le 8% nižjo vrednost maksimalnega energijskega produkta.

Tretja tematika predstavlja tretji članek s prvim avtorstvom z naslovom "Significant coercivity enhancement of hot-deformed bulk magnets by two-step diffusion process using a minimal amount of Dy", kjer se je izvajal dvostopenjski proces difuzije po mejah med zrni na vroče deformiranemu magnetu Nd-Fe-B z dodatkom minimalne količine Dy. Vrednost koercitivnosti vroče deformiranega magneta Nd-Fe-B debeline 5,6 mm debelega magneta se je zvišala z 1,13 T na 2,5 T, hkrati pa ohranila visoko remanentno magnetizacijo 1,32 T z uporabo zlitin $Nd_{50}Dy_{30}Cu_{20}$ in $Nd_{80}Cu_{20}$ za prvi in drugi korak difuzijskega procesa. Le 0,45 m.% Dy je bilo porabljenega pri procesu difuzije v vroče deformiranemu magnetu, kar je le ≈10 % delež Dy, ki se porabi v običajnih sintranih magnetih Nd-Fe-B z dodanim Dy, s primerljivo vrednostjo koercitivnosti. Poleg visoke vrednosti koercitivnosti pri sobni temperaturi, končen difuzijsko procesiran vroče deformiranem magnet poseduje tudi odličen temperaturni koeficient koercitivnosti –0,41 %/°C. Posledično to delo utira pot k razvoju magnetov Nd-Fe-B z nizko vsebnostjo Dy in z visoko vrednostjo koercitivnosti.

Zadnji del te disertacije predstavlja izum, ki se nanaša na izboljšanje koercitivnosti komercialnih ultra-hitro kaljenih magnetnih trakcev Nd-Fe-B z majhnim deležem intergranularne faze in na postopek za proizvodnjo polimerno vezanih magnetov z difuzijo nizkotemperaturne evtektične zlitine (Nd-Cu). Koercitivnost komercialnih trakcev Nd-Fe-B za določene aplikacije ni zadovoljiva, medtem ko so komercialni magnetni trakci za izdelavo polimerno vezanih magnetov z visoko koercitvnostjo, zaradi dodatka težkih redkih zemelj, bistveno dražji. Ta izum predstavlja izboljšanje magnetnih lastnosti (koercitivnosti) ekonomsko ugodnejših ultra-hitro kaljenih magnetnih trakcev Nd-Fe-B, z majhnim deležem intergranularne faze. Rešitev za povečanje koercivnosti je difuzija nizkotemperaturne evtektične zlitine (Nd-Cu), ki pripomore k 15 % izboljšanju vrednosti koercitivnosti končnega polimerno vezanega magneta v primerjavi z magnetom, ki je pripravljen iz standardnih nizkocenovnih magnetnih trakcev Nd-Fe-B.

Contents

List of Figures

List of Tables

Abbreviations

BSE	... Backscattered electrons
B	... Boron
Co	... Cobalt
Cu	... Copper
Tc	... Curie temperature
$CaCu_5$	... Df
DC	... Direct current
d-HDDR	... Dynamic-hydrogenation disproportionation desorption recombination
Dy	... Dysprosium
Ga	... Gallium
GB	... grain boundary
GBDP	... grain boundary diffusion process
HRE	... Heavy-rare-earth
HRE-GBDP	... Heavy-rare-earth grain boundary diffusion process
HDDR	... hydrogenation-disproportionation-desorption-recombination
Mg	... Magnesium
Mn	... Mangan
$(BH)_{max}$	... maximum energy product
Nd	... Neodymium
Ni	... Nickel
RE	... Rare-earth
$RE_2(TM)_{17}$	... Rare-earth (transition metal)
Sm_2Co_{17}	... Samarium Cobalt
$SmCo_5$	... Samarium Cobalt
SmFeN	... Samarium Iron Nitride
SPS	... Spark-plasma-sintering
Sr	... Strontium
Tb	... Terbium
TM	... Transition metal

Symbols

θ	. . . angle between an external magnetic field and magnetic moment
K_1	. . . anisotropy constant
N_{eff}	. . . averaged local effective demagnetization factor
H_c	. . . coercivity
α_ψ	. . . Crystalline energy
T_c	. . . Curie temperature
A	. . . current loop surface area
N_d	. . . demagnetizing coefficient (factor)
H_d	. . . demagnetizing field
Q	. . . density of flux
E	. . . energy of a magnetic moment
B_s	. . . induction saturation
H	. . . magnetic field
B	. . . magnetic induction or magnetic flux density
m	. . . magnetic moment
μ_0	. . . magnetic permeability in vacuum
M	. . . magnetization
M_r	. . . remanent magnetization (remanence)
α_K	. . . nucleation effect of inhomogeneity
B_r	. . . residual induction or retentivity
M_s	. . . saturation magnetization
χ	. . . susceptibility
I	. . . total current
V	. . . volume

Chapter 1

Introduction

1.1 Development of Permanent Magnets

Permanent magnets are materials that preserve their properties after being exposed to an external magnetic field. They are able to produce a strong magnetic field without applying an electric current and exhibit a strong net magnetization [1]. The first application of a permanent magnet was as the needle in the compass. Today, they are essential components in everyday applications, such as energy conversion, transportation, and many others.

Permanent magnets are some of the earliest functional materials, already known in ancient times. The first discovered natural permanent magnet was a lodestone, composed mainly of magnetite [2]. In the late 1500s, Sir William Gilbert first reported on the magnetic properties of ferrous materials and explained how steel and iron can be magnetized by lodestones [3]. The discovery of the electromagnet in 1825 by André-Marie Ampére was a milestone event for the beginning of the industrial revolution. Combined with Maxwell's equations, the linking of mechanical work to electromagnetism was introduced. By the end of the 1800s, the magnetic properties and requirements to operate of electric motors and generators were already well known [4]–[6].

Magnetic materials started to develop more rapidly in the 20$^{\text{th}}$ Century.

Figure 1.1 shows the development of permanent magnets in the last 100 years and the progress of their maximum energy product $(BH)_{\text{max}}$, which defines the maximum amount of energy stored in a magnet [7]. At the beginning of the century, a cobalt-steel magnet with almost double the coercivity compared to previous magnets was used for the first time in Japan [8]. From this type of magnets, a family of iron-aluminum-nickel-cobalt alloy magnets, also called Alnico, was developed by Mishima in Japan [8]. This type of magnet has a small temperature dependence of magnetic properties due to a high Curie temperature and maximum energy product above 80 kJ/m^3 [8], [9]. At one point, the Alnicos were the most widely used permanent magnet materials, until they were largely replaced by newly developed permanent magnets, i.e. ferrites.

In 1952, the Phillips company from the Netherlands introduced to the market a new type of permanent magnets – ferrites. These magnets are divided into two groups – soft and hard ferrites. Soft ferrites with general composition $MOFe_2O_3$ where M stands for Mg, Ni, Mn, Zn have a cubic crystal structure and Curie points ranging from 300 to 600 °C. Hard ferrites also called hexaferrites with general chemical composition $MO_6Fe_2O_3$, where M stands for Ba, Sr, or Ca have a hexagonal crystal structure, a large uniaxial crystal anisotropy and a Curie temperature of 450 °C [8]. The ferrites can have a maximum energy product above 40 kJ/m^3 [10].

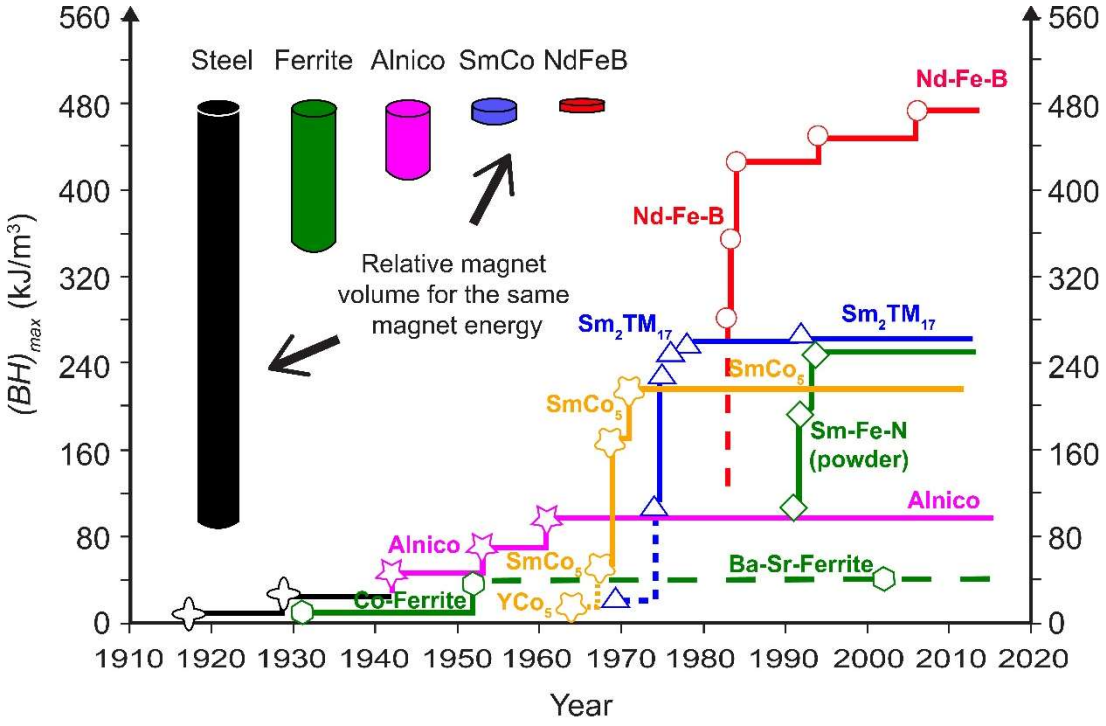

Figure 1.1: Development of permanent magnets [7].

In the late 1960s, the first rare-earth permanent magnet composed from the rare-earth element samarium (Sm) and transition-metal element cobalt (Co) was developed, based on the research on the anisotropy of the YCo_5 magnet by K.J. Strnat at U.S. Air Force Materials Laboratory at Wright-Patterson Air Force Base [11]. This $SmCo_5$ compound was the first high-performance permanent magnet with a hexagonal $CaCu_5$-type crystal structure (Figure 1.2:) and an anisotropy constant of 7.7×10^6 J/m^3. Besides, the magnet possessed a large magnetocrystalline anisotropy ($\mu_0 H_A$) of 28 T, a high Curie temperature (T_c) of 720 °C, saturation magnetization (M_s) of 1.14 T and a maximum energy product $(BH)_{max}$ above 160 kJ/m^3 (

Figure 1.1). Today, the sintered $SmCo_5$ magnet can have a coercivity up to 1900 kA/m (2.4 T) and a 0.9 T remanence. [8], [12].

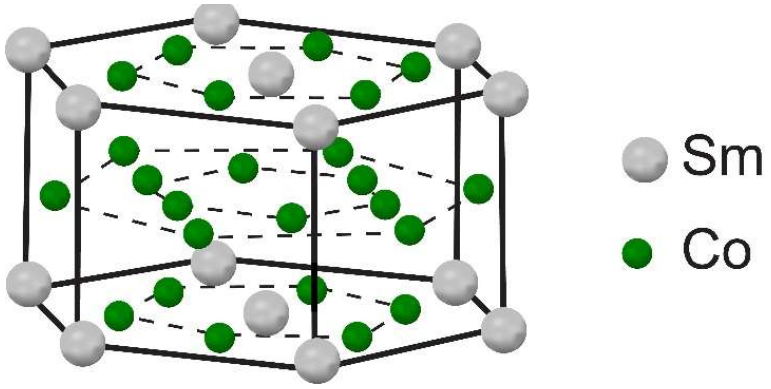

Figure 1.2: Hexagonal crystal structure of $SmCo_5$ compound [13].

Typically, to fully magnetize the permanent magnets an external magnetic field several times higher than the coercive field is required. But, $SmCo_5$ magnets have an unusual

advantage where they can be initially magnetized by an external field that is smaller than the intrinsic coercive field of the magnet. This behaviour of easy magnetization is explained by domain walls, which move easily in an applied field. Consequently, it means that M_s can be achieved in relatively low applied fields. On the other hand, this type of magnet is difficult to demagnetize due to a strong barrier to nucleation. Therefore, the $SmCo_5$ type magnet has a nucleation-controlled type of coercivity [8], [14].

The development of rare-earth permanent magnets continued and in 1972 a Sm_2Co_{17} compound was introduced [15]. This magnetic material comes from a family of a new rare-earth-based intermetallic compounds $RE_2(TM)_{17}$, which have either hexagonal (Th_2Ni_{17}) or rhombohedral (Th_2Zn_{17}) crystal structure shown in Figure 1.3. The first structure type is typical for heavy rare earths, meanwhile the second type is typical for light rare earths. The stoichiometry of the Sm_2Co_{17} compound is closely related to the $CaCu_5$ structure because this phase consists of $CaCu_5$-like subcells and differs only in the stacking of these subcells [16]. Despite a close relation with the $SmCo_5$ structure, the Sm_2Co_{17} compound possesses higher magnetization per unit weight due to higher transition-metal concentration. The Curie temperatures, between 600 °C and 940 °C, are even higher than for $SmCo_5$, which makes this type of magnet appropriate for usage in high-temperature applications [15], [17]. First, Sm_2Co_{17} magnets exhibited coercivity of 800 kA/m (1 T) and a maximum energy product of 260 kJ/m^3. Today these values are much higher - the coercivity above 2000 kA/m (2.5 T), maximum energy product above 250 kJ/m^3, and remanence up to 1.1 T [7], [18]. The high coercivity is a result of domain-wall pinning, which means that the Sm_2Co_{17}-type magnet has a pinning-controlled coercivity.

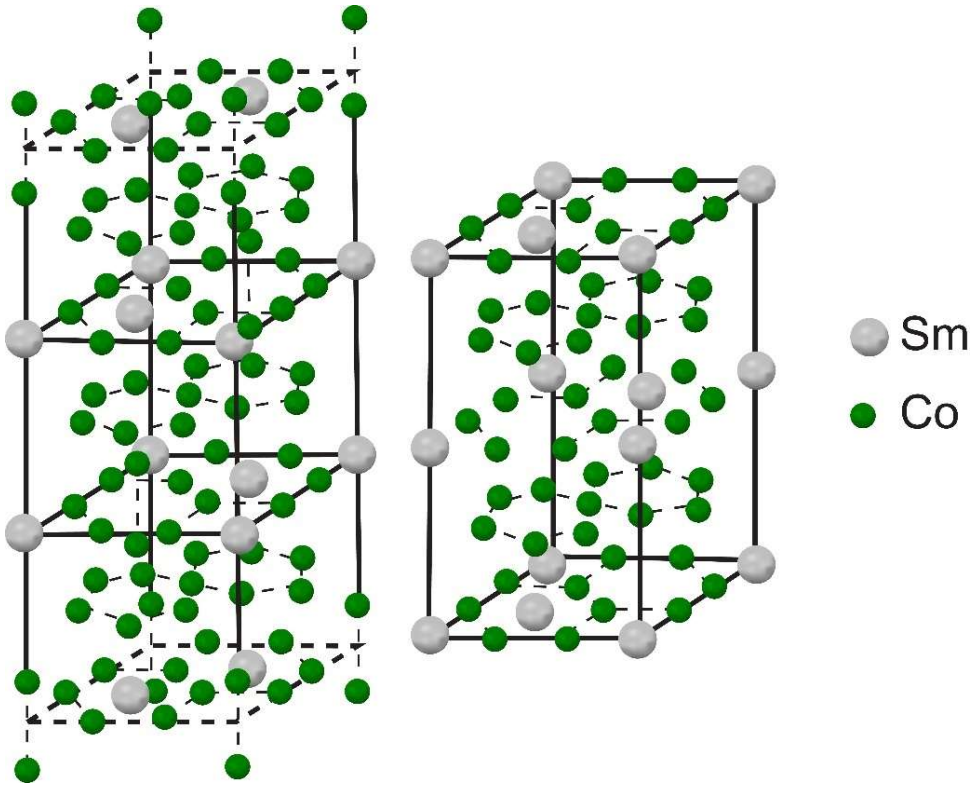

Figure 1.3: Rhombohedral (a) and hexagonal (b) crystal structure of Sm_2Co_{17} compound [13].

The $Sm_2(Co,Fe,Cu,TM)_{17}$ compound was the final development stage of Sm-Co magnets [19]. However, the economic crises in the 1970s and problems with cobalt supply forced the

research groups to invent a new type of rare-earth permanent magnets. They needed to find an appropriate replacement for samarium-cobalt magnets that were suitable for high-temperature applications. The research was focused on rare-earth transition-metals permanent magnets, produced from less-expensive constituents. Several attempts were made to develop rare-earth(RE)-iron permanent magnets with coercivities comparable to these of Sm-Co magnets [8], [19]. The first experiments were performed in the 1970s by Clark and Rhyne [20], [21]. They prepared (Tb,Dy,Sm,Gd,Y)Fe_2 compounds by melt-spinning technique. The amorphous $TbFe_2$ melt-spun ribbons were annealed to provide the crystalline microstructure with a high coercivity of 270 kA/m (0.34 T) [20]. Between 1980 and 1982, Croat et al. successfully prepared (Pr,Nd)-Fe melt-spun ribbons with a coercivity up to 690 kA/m (0.87 T) [22]–[25]. At the same time, Das and Koon et al. reported on the development of $La_{0.05}Tb_{0.05}Fe_{0.74}B_{0.16}$ alloys where the coercivity reached 700 kA/m (0.88 T) after crystallization at 630 °C [26], [27]. In 1983 and 1984 Hadjipanayis et al. studied different rare-earth-iron-metalloid systems and obtained a coercivity of 1200 kA/m (1.51 T), a maximum energy product of more than 100 kJ/m^3 in melt-spun $Pr_{0.16}Fe_{0.76}Si_{0.03}B_{0.05}$ compound after an annealing process [28], [29]. In 1984 the $Nd_2Fe_{14}B$ phase was developed independently by Croat et al. in General Motors Research Laboratories and Sagawa et al. from Sumitomo Special Metals Corporation. Those two companies followed different routes to successfully process a new family of rare earth permanent magnets and filed a series of patents of which the conditions are complex. Croat et al. reported on high-coercivity (~1600 kA/m (2 T)) melt-spun $Nd_{0.135}(Fe_{0.945}B_{0.055})_{0.865}$ ribbons with maximum energy product of 110 kJ/m^3 [30], [31]. Meanwhile, Sagawa et al. produced a $Nd_{0.15}Fe_{0.77}B_{0.08}$ magnet by the traditional sintering process method used for Sm-Co magnets. They prepared an ingot with composition $Nd_{0.15}Fe_{0.77}B_{0.08}$ by induction melting. The ingot was crushed in a nitrogen atmosphere and milled to the particle size of approximately 3 µm. The particles were aligned in a magnetic field and pressed perpendicularly to the aligned direction. Such green compacts were sintered at 1080 °C for 1 h and post-sintered at 630 °C for 1 h. The magnet possessed a coercivity of 960 kA/m (1.2 T) and a maximum energy product of 290 kJ/m^3 [32].

The origin of the best magnetic properties of Nd-Fe-B magnets among permanent magnets is in the $Nd_2Fe_{14}B$ hard magnetic matrix phase with a body-centred tetragonal crystallographic structure and $P4_2/mnm$ space group, which is closely related to the hexagonal $CaCu_5$-type crystal structure [33]. This compound has uniaxial magnetocrystalline anisotropy with the easy direction of magnetization along the *c*-axis [32], [33]. There a four $Nd_2Fe_{14}B$ units with 68 atoms per unit cell are arranged in two crystallographically inequivalent Nd sites, six inequivalent Fe sites and one B site (Figure 1.4) [31], [34], [35].

Today, the Nd-Fe-B permanent magnets have a maximum energy product above 400 kJ/m^3 (

Figure 1.1), meanwhile the typical coercivity retains 960 kA/m (1.2 T), which is only ~ 15 % of the theoretical magnetocrystalline anisotropy of $Nd_2Fe_{14}B$ phase ($\mu_0 H_A$ ~7.5 T) [36], [37]. Although the maximum energy product getting close to the theoretical value (512 kJ/m^3 [32], [38]) of $Nd_2Fe_{14}B$ phase, the coercivity as a most important extrinsic magnetic property is still far away from the theoretical limit, which means that here is still a lot of room for improvement [39].

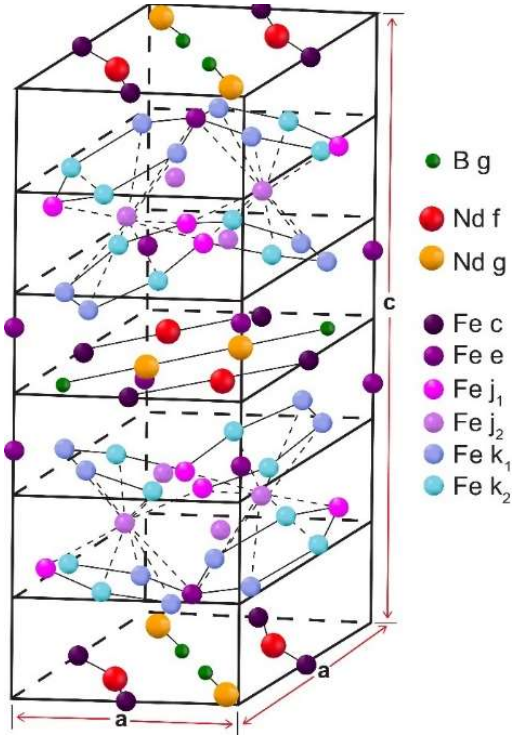

Figure 1.4: Tetragonal crystal structure of $Nd_2Fe_{14}B$ compound [34].

1.2 Magnetism Fundamentals

Magnetization (M) is a property of a material that depends on the individual magnetic moments of its magnetic origins. It originates in the spin and orbital magnetic moments of the electrons in the atoms and represents the sum of magnetic moments per unit of volume on the atomic scale [40].

Two different modes of electron motion impact the magnetic moment - orbital and spin motion. The orbital motion of the electron around the nucleus can be naively interpreted as the circulation of a charge and looks similar to the current in a wire loop without resistance. The magnetic moment of an electron circulating around the nucleus is therefore defined with the following Eq. (1.1) [41]–[43]:

$$\mu = (area\ of\ loop) \cdot (current) \tag{1.1}$$

where the area of the loop is defined as πr^2 and r is the atomic radius. To provide the value of μ, the electron velocity and shape and size of the orbit must be determined. In the Bohr theory of the atom, the electron moves in a circular orbit of radius r with the velocity v. The charge carried by an electron is e, which means that current is then defined as $ev/2\pi r$. Therefore [41]–[43]:

$$\mu(orbit) = \frac{evr}{2} \tag{1.2}$$

The theory has an additional postulate where the angular momentum of the electron is defined as an integral multiple of $h/2\pi$, where ħ stand for Planck's constant. Consequently [41]–[43]:

$$mvr = n\frac{h}{2\pi} \tag{1.3}$$

where n is the orbital quantum number, and m is the mass of an electron. The combination of Eq. (1.2) and Eq. (1.3), gives the following equation [41]–[43]:

$$\mu(orbit) = \frac{eh}{4\pi m} \tag{1.4}$$

where the magnetic moment is in the first Bohr orbit (n = 1) [8]. The magnetic moment contributed by the spin was firstly proposed by Uhlenbeck and Goudsmit in 1925 [44]. They claimed the electron possesses an intrinsic angular momentum, assign as spin, which contributes to an increase of magnetic moment in electron. Using Eq. (1.4), where $e = 1.60 \cdot 10^{-19}$ C, $h = 6.62 \cdot 10^{-34}$ Js, and $m = 9.11 \cdot 10^{-31}$ kg, the value magnetic moment due to spin is following [41]–[43]:

$$\mu(spin) = 9.27 \cdot 10^{-2}\ Am^2 = \mu_B \tag{1.5}$$

Due to the equal equations for the calculation of magnetic moments due to spin and orbit, the value of both magnetic moments is equal in the first Bohr orbit. This value of the magnetic moment is an important quantity in magnetism, that is why this amount of magnetic moment was provided by an exclusive symbol μ_B with an appropriate name – Bohr magneton [41]–[43].

Each electron in an atom has its own magnetic moment, and the sum of all electronic moments is the magnetic moment of the atom, which gives two different possibilities:

1. The atom has no net magnetic moment if the magnetic moments of electrons are orientated in a direction to cancel one another out. The material with no net magnetic moment is called diamagnetic.
2. The atom has not net magnetic moment equal to zero, also called a magnetic atom, if the magnetic moments of electrons only partially cancel each other out. The materials with net magnetic moments are ferro-, antiferro-, ferri- or paramagnetic [40], [42], [43].

When the magnetic material is exposed to an external magnetic field, H, its response is called the magnetic induction or magnetic flux density, B, which is defined in the following equation (Eq. (1.6)) [45], [46]:

$$B = \mu_0(M + H) \tag{1.6}$$

where μ_0 is permeability in free space. The SI unit of magnetic induction or flux density is T and the unit of the magnetization and external field is A/m. The flux density is in general different inside from that of the outside of the material. Based on the difference of the material's internal and external flux density, the classification of magnetic material can be made. If the flux density outside of the material is higher than inside, the material is called diamagnetic. The atoms or ions of this material have zero magnetic dipole moment. Bi and He are examples of diamagnetic material. The paramagnetic (Al, Na) or antiferromagnetic (FeO, MnO) material has a slightly higher density flux inside the material than outside. These two materials have atoms or ions with a magnetic dipole moment. In antiferromagnetic material, the dipole moments are oriented antiparallel meanwhile in paramagnetic material the dipole moments are randomly orientated. The last option is ferromagnetic or ferrimagnetic material where the flux density outside of the material is much lower than inside. The magnetic moments in this material is manage to line up in the same direction. The magnetic dipoles align parallel like in the case of an

antiferromagnetic material, however, some of the moments are larger than others which means that the overall magnetic dipole moment is not equal to zero. The schematic shows ordering of the magnetic dipoles in different types of magnetic materials in Figure 1.5 [45].

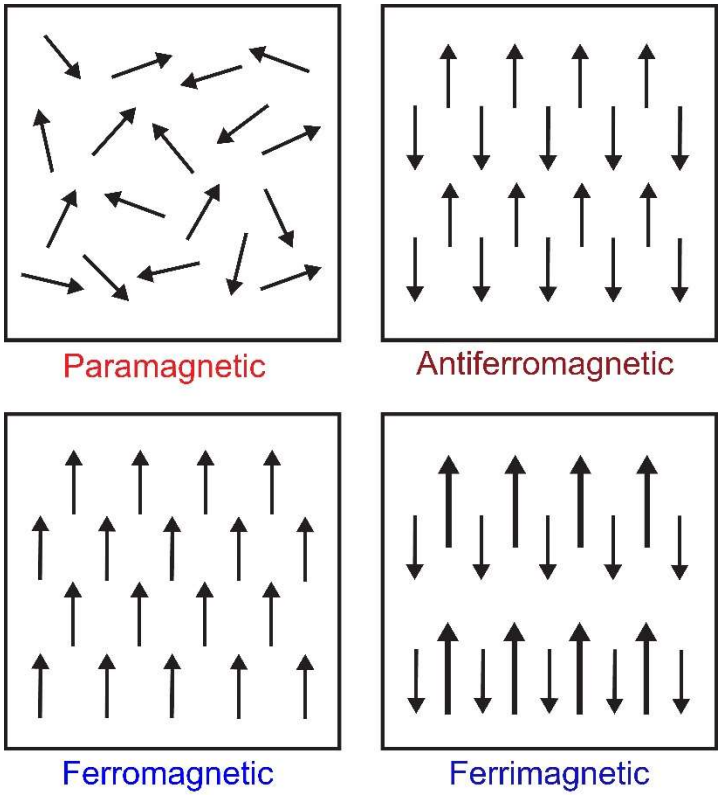

Figure 1.5: Magnetic dipoles ordering in different types of magnetic materials [45].

1.2.1 Susceptibility and permeability

The magnetic material is not defined by the magnetic induction or magnetization property, but also by properties on which these two quantities vary with the applied field. One of these properties is susceptibility (χ) that describes the responsiveness of the material to an applied magnetic field. It is defined as the quotient between magnetization and applied field (Eq. (1.7)) [45], [47]:

$$\chi = \frac{M}{H} \tag{1.7}$$

Another important property is permeability which is defined as the quotient between flux density and applied field and indicates how permeable is the material to the magnetic field (Eq. (1.8)) [45]:

$$\mu = \frac{B}{H} \tag{1.8}$$

In the SI units, the permeability is in henry/m unit, meanwhile, susceptibility is dimensionless. The relationship between these two properties describes the following Eq. (1.9) [45]:

$$\frac{\mu}{\mu_0} = 1 + \chi \tag{1.9}$$

where μ_0 is the permeability in a vacuum.

Figure 1.6 shows the magnetization curves (M vs H) characteristic for paramagnetic, and diamagnetic material. All of the M-H magnetization curves are linear and rather large applied fields are required for minor changes in magnetization. All these types of magnetic materials possess no magnetization if the applied field is removed. The diamagnetic material has a small negative slope of magnetization curve, which means the susceptibility is negative and small ($\approx$ - 10^{-5}). The permeability of diamagnets is less than 1. In the case of a paramagnetic or antiferromagnetic material, a susceptibility has a small positive slope resulting in a small and positive susceptibility ($\approx 10^{-2} - 10^{-5}$). The value of the permeability of these two types of magnets is more than 1 [45], [47].

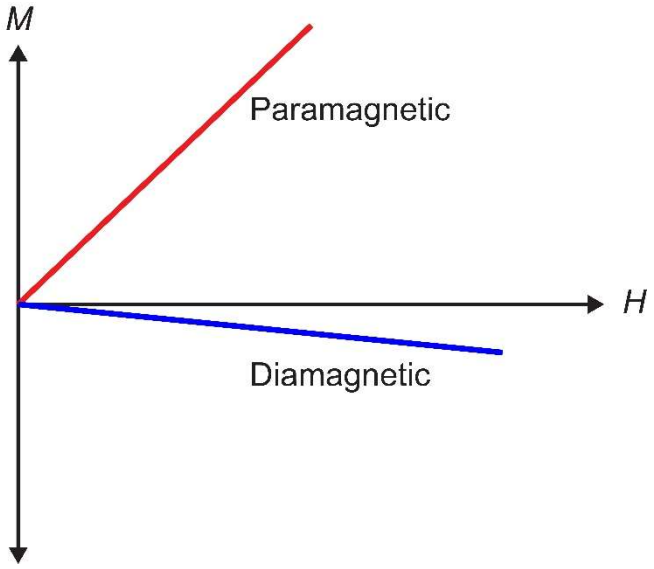

Figure 1.6: Magnetization curves for different types of magnetic materials [8], [45].

1.2.1.1 Hysteresis

Figure 1.7 shows the magnetization curve of ferrimagnetic and ferromagnetic material. In this case, the axis scales are completely different resulting in much higher magnetization of material at a much smaller applied field. The curve is nonlinear and susceptibility and permeability are functions of an applied field. Both values are large and positive [8], [45].

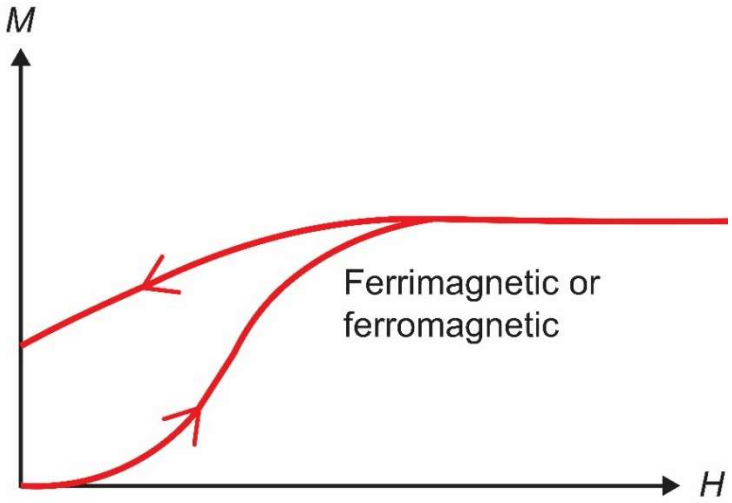

Figure 1.7: Magnetization curve of ferrimagnetic or ferromagnetic material [8], [45].

At a certain applied field where the magnetization becomes constant, a saturation magnetization value (M_s) is achieved. At that point, any further increase of the applied field causes a minor increase in magnetization. After the saturation magnetization is achieved, the magnetization does not drop to zero even though the applied field is reduced to zero or changed in the opposite direction. The chart of B or M versus H shown in Figure 1.8 is called hysteresis loop. The magnetic material is in origin unmagnetized. After the applied field is initiated and increased in the positive direction, the magnetic induction or flux density goes from 0 to saturation magnetization (M_s). If the applied field H is reduced to zero, after the saturation magnetization is achieved, the magnetization decreases from M_s to remanent magnetization (M_r). Using the reversed applied field, the magnetization will decrease to zero at the point where the reverse field equals the intrinsic coercivity (H_c). The value of coercivity determines whether the ferromagnetic material is magnetically soft or hard. The magnetically soft material is easily magnetized and demagnetized, meanwhile, a hard magnet requires a large field to achieve the point of coercivity [8], [45].

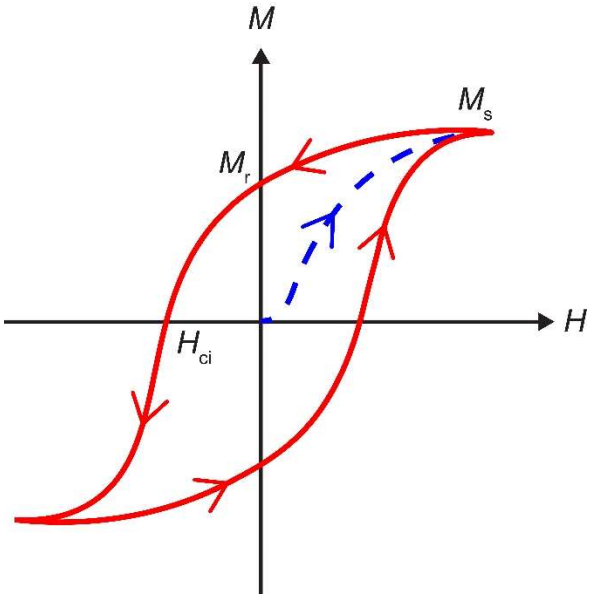

Figure 1.8: M vs H hysteresis loop [48].

Figure 1.9 shows a hysteresis loop plotted as B versus H. The magnetic material is unmagnetized at the origin. After the applied field is initiated and increased in the positive direction, the magnetic induction goes from 0 to induction saturation (B_s). After the saturation is achieved, the value of B continues to increase parallel with an increase of H, because H forms part of B [8], [45]. If the H is reduced to zero, after the saturation is achieved, the induction decreases from B_s to residual induction or retentivity (B_r). Using the reversed applied field, the induction will decrease to zero at the point where the reverse field equals coercivity (H_c).

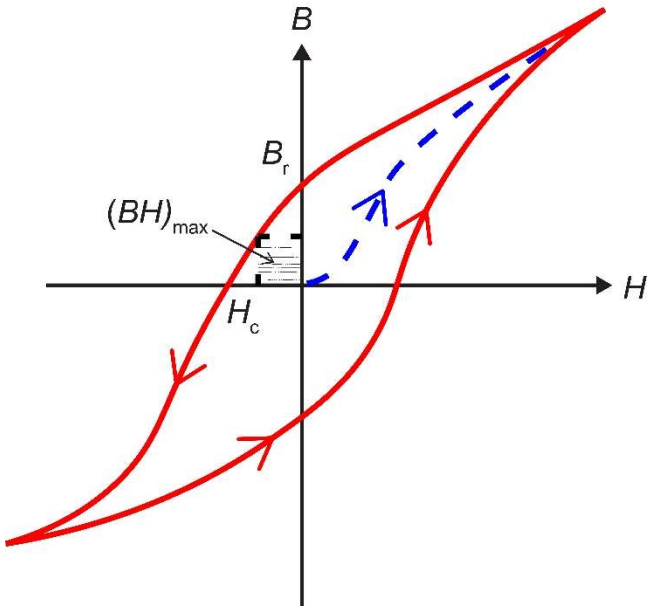

Figure 1.9: B vs H hysteresis loop [48].

The second quadrant normally describes the quality of the magnetic material. The largest rectangular area under the hysteresis loop in the second quadrant is called the maximum energy product. It is the point where the product of B and H reaches the highest value and it is measured in kJ/m^3 [8], [45], [48].

Ferrimagnetic or ferromagnetic material differs in the applied field required to achieve saturation magnetization. A magnetic material that can be easily magnetized is magnetically soft meanwhile the materials where large fields are required to achieve the saturation magnetization are magnetically hard. Some of the magnetic materials can be even soft or magnetically hard which depends on their physical condition. In Figure 1.10, curve (a) represents this type of material as magnetically soft well-annealed material meanwhile curve (b) as magnetically hard heavily cold-worked state material, and (c) as magnetically hard material [8].

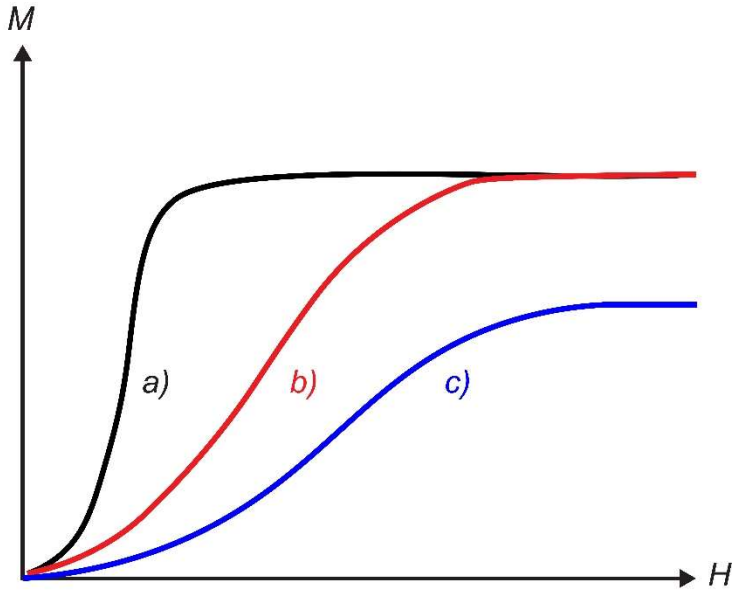

Figure 1.10: Different types of magnetic curves [8].

1.2.2 Anisotropy

There are several factors that affect the shape of the hysteresis loop; however, magnetic anisotropy is a main factor for the final shape of the loop. The anisotropy explains a difference in the magnetic properties of the material with respect to the direction of measurements of these properties. The various forms of magnetic anisotropy are listed below [8], [45], [46]:

- Magnetocrystalline anisotropy (or crystal anisotropy);
- Shape anisotropy;
- Stress anisotropy (magnetostriction);
- Induced magnetic anisotropy;
- Exchange anisotropy.

All these different anisotropies contribute to the shape of the hysteresis loop; however, two anisotropies stand out here (crystal and shape anisotropy) which will be described in the following chapters.

1.2.2.1 Magnetocrystalline anisotropy

This form of magnetocrystalline anisotropy is mainly formed due to spin-orbit coupling caused by the spin-orbit interaction of the electrons. Two neighbouring spins exchange interact as a spin-spin coupling. In this way, neighbouring spins lie antiparallel or parallel to one another, which makes this type of coupling very strong. However, the spin-spin coupling does not contribute to the crystal anisotropy due to the associated energy which is isotropic. This energy does not affect the direction of the spin axis relative to the crystal structure and consequently on magnetocrystalline anisotropy. It affects only the angle of adjacent spins [8], [46].

Another type of coupling is lattice-orbit coupling, which is also very strong due to the strongly attached orientations of orbits in the crystal lattice. This means that even a large magnetic field cannot change them.

The third coupling type is between the orbital and spin motion of the electron. The energy required to overcome the orbit-spin coupling is equal to the anisotropy energy, which is also the energy required to rotate the spin system of the domain away from the easy direction. In this case, a low energy is required to rotate spins, which is why this type of coupling is weak.

The last coupling type is between the spin and lattice, which is also weak because the lattice consists of a number of atomic nuclei where each nuclei is surrounded by a cloud of orbital electrons [8].

The magnetocrystalline energy is rather small in comparison with the exchange energy. It also decreases faster than the magnetization with an elevated temperature and goes to zero at the Curie temperature. However, the direction of magnetization is associated with the crystal anisotropy due to exchange interaction, which forces the magnetic moments to align parallel one to another. Besides, the anisotropy strongly affects the coercive field, which drops to zero together with the anisotropy [8], [46].

The superiority of rare-earth permanent magnets is strongly connected with their high magnetocrystalline anisotropy, which conditions the high stability of the magnetization direction with respect to the crystal axes [49]. This anisotropy is the intrinsic property independent of shape and grain size that can be seen by the measurement of magnetization curves along different crystal directions [50]. It has been shown that depending on the

orientation of the field with respect to crystal lattice a different applied field is sufficient to reach saturation magnetization (Figure 1.11) [51]:

- *Easy axis* is the direction in the crystal, where a small applied field is needed to reach the point of saturation magnetization.
- *Hard axis* is the direction in the crystal, where a high applied field is needed to reach the point of saturation magnetization [51].

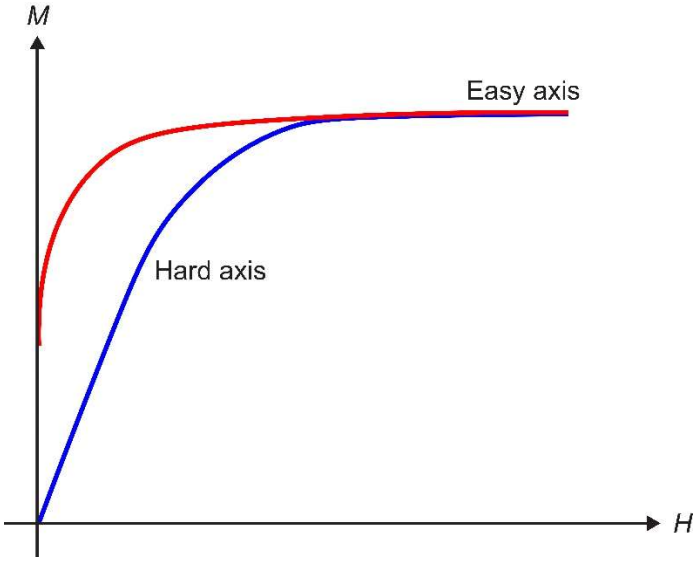

Figure 1.11: Magnetization curves along hard and easy axes [50].

The magnetocrystalline anisotropy is also the source of coercivity and hysteresis which categorize the magnets into soft or hard magnetic materials [49]. This anisotropy is uniaxial in typical permanent magnets which means that magnetic energy can be expressed with the following equation in the lowest (or second) order [49]:

$$E = K_1 V \sin^2 \theta \tag{1.10}$$

where K_1 denotes the first uniaxial anisotropy constant, θ the angle between the crystallographic c-axis and magnetization and V the volume of the magnet. If the magnetization is nonuniform (ferromagnetic grain boundaries), the K_1 can alternatively represent an anisotropy-energy density. The units of E and K_1 are J/m^3 [8], [49].

1.2.2.2 Shape anisotropy

Most of the materials have magnetocrystalline anisotropy; however, the polycrystalline specimen with no preferred orientation of the grains possesses no net crystal anisotropy. If the sample has an exactly spherical shape, the same external field is required to magnetize it to the same extent in each direction. If this condition is not met, then the sample will be easier to magnetize along the long axis (or easy axis) than along the short axis. The reason for this phenomenon is a stronger demagnetizing field H_d along the short axis which means that the external field should be stronger along the short axis direction to provide a uniform field within the specimen [8], [45], [46].

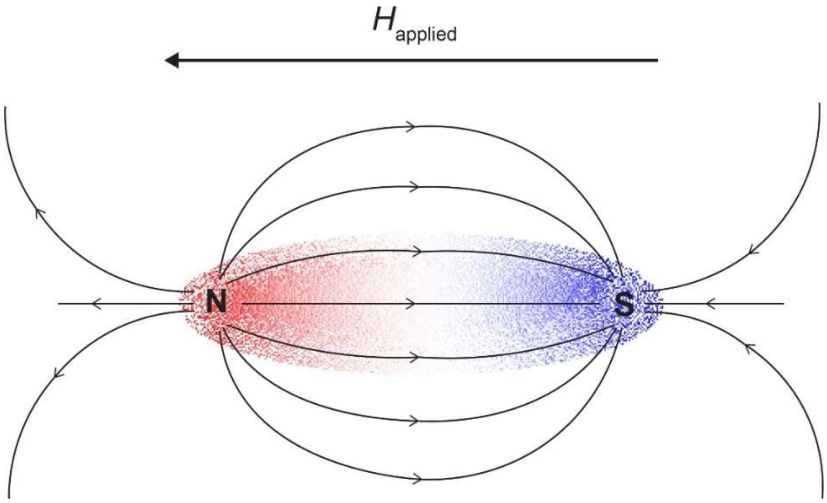

Figure 1.12: Radiation of H lines around a spheroid [45].

For a better understanding of shape anisotropy, the demagnetizing field should be introduced qualitatively via magnetic poles. Figure 1.12 shows the spheroid which was magnetized from right to left by an external magnetic field. In this way, two different poles are generated – the north pole at the left side and the south pole at the right side of the spheroid. A result of two different poles is a pattern of H lines that radiate from the north to the south pole of the spheroid. The important fact is that the field inside of the sample points toward the south pole, which is the opposite direction of the external magnetic field and is called demagnetizing field H_d. This field is created by magnetization of the sample and its size is directly proportional to the size of magnetization. The demagnetizing field (H_d) is defined as (Eq. (1.11)):

$$H_d = N_d M \tag{1.11}$$

where N_d is a demagnetizing coefficient (factor) governed by the shape of the specimen. In the case of prolate spheroid or elongated sample, N_d is large along the short axis and small along the long axis. When the anisotropy becomes even more pronounced, the aspect ratio increases – the distance between poles goes toward infinity and N_d factor toward zero [45].

1.2.3 Curie temperature

The alignment of the magnetic moments is strongly associated with the temperature. The temperature where the spontaneous magnetization of material drops to zero is the so-called Curie temperature (T_c). It can be understood as the transition temperature between the ferromagnetic and paramagnetic phase. In specific heat, the magnetic ordering is a continuous thermodynamic phase transition with a λ-shaped anomaly connected with the disordering of the atomic dipole moments. Among ferromagnetic materials, cobalt has the highest T_c of 1115 °C followed by iron and nickel with Tc of 771 °C and 355 °C [47]. The T_c temperatures of ferrimagnetic and ferromagnetic materials are collected in Table 1.1 [46].

Table 1.1: Curie temperatures of ferrimagnetic and ferromagnetic materials [46].

Material	T_c [K]
Fe	1043
Co	1388

Ni	627
Gd	293
Dy	88
EuO	69
Fe_3O_4	853
CrO_2	387

1.3 Processing of Nd-Fe-B Magnets

The magnetic properties and the microstructure of a magnetic material produced by a specific processing route depend not only on the initial material composition but also on the heat treatment regime and processing parameters. Thus, Nd-Fe-B magnets can be produced through different processing routes, which are usually separated based on their microstructure. The microstructure can be either microcrystalline or nanocrystalline which divides the production into two completely different processing routes shown in Figure 1.13 [52], [53].

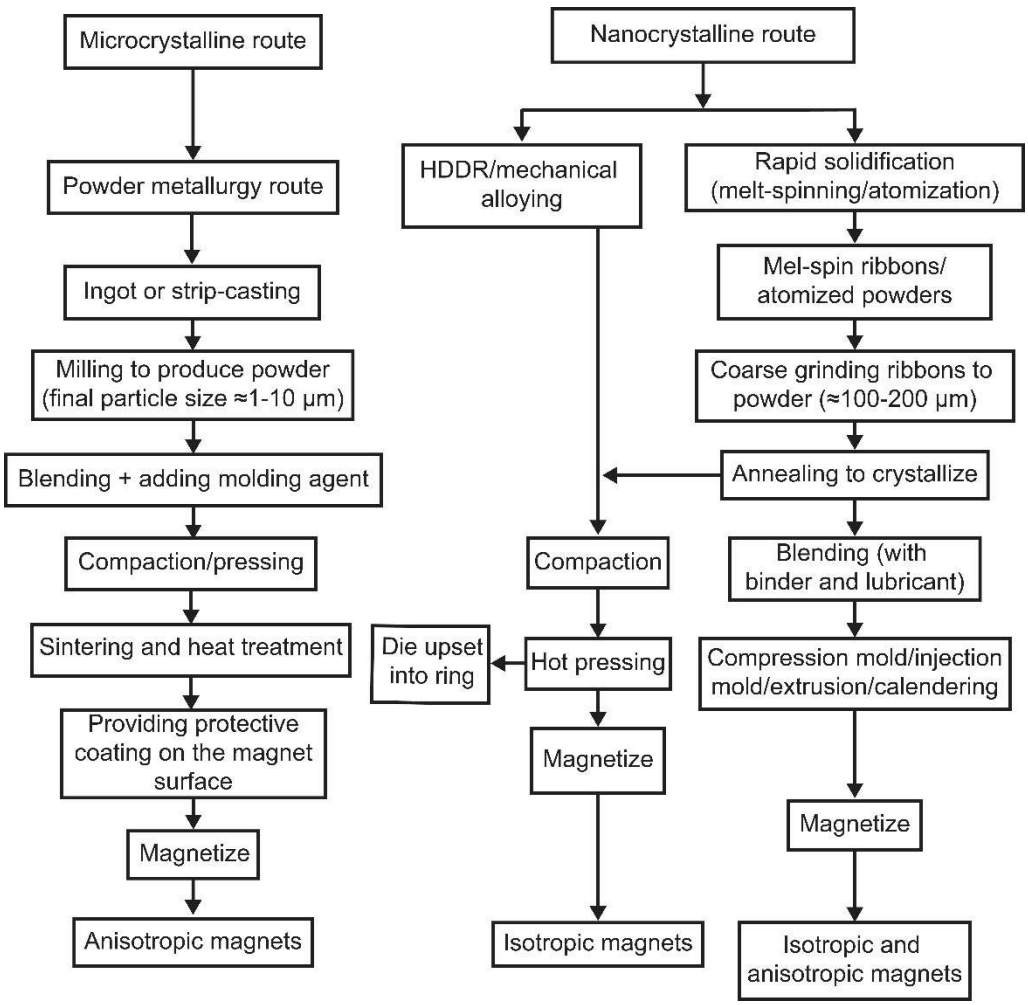

Figure 1.13: Schematic figure of processing routes for Nd-Fe-B magnets [52].

The microcrystalline route is based on the powder-metallurgy technique, where the sintering provides fully dense anisotropic magnets with a $(BH)_{max}$ around 400 kJ/m^3. On the other hand, the nanocrystalline route includes rapid-solidification techniques (melt spinning, atomization), HDDR process (hydrogenation-disproportionation-desorption-recombination) and mechanical alloying technique. This route results in anisotropic magnets with $(BH)_{max}$ ~ 160—440 kJ/m^3 and isotropic magnets with $(BH)_{max}$ ~ 80—120 kJ/m^3 [52], [53].

1.3.1 Powder metallurgy route

The powder-metallurgy process for the production of Nd-Fe-B magnets was discovered by Sagawa in 1984 [32] and since then, this process serves as a technique for processing anisotropic sintered magnets [54]. The process begins with an ingot being cast with a relatively large amount of rare earth in initial composition (Nd, Dy ~ 15 at.%) which limits the α-Fe precipitation and promotes the subsequent liquid-phase grain-boundary sintering operation [53]. The strip casting technology development through the years enables higher cooling rates, finer scale and homogeneous microstructure, which leads to lower consumption of rare earth in the initial composition (Nd + Dy ~ 14 at.%) with no need for post-cast annealing. The so-prepared ingot is then coarse ground and (jet) milled in a protective atmosphere into a fine powder with particle size around 5 µm. The resulting powder can be aligned in a magnetic field (~ 800–1600 kA/m (1–2 T)) and subsequently pressed into a green compact [53].

The sintering of a green compact is performed at elevated temperatures (1000–1100 °C) from 2 to 4 hours in a protective atmosphere (argon) or in a vacuum. During the thermal treatment, the grain boundary phase melts at ~ 630 °C and therefore, this process can be also called the liquid phase sintering process [32], [55]. In the cooling process after the heat treatment, the Fe-rich precipitates occur within the Nd-rich phase, mostly at the surface of neighbouring $Nd_2Fe_{14}B$ grains. The temperature of the sintering process determines the morphology, the number and the size of the initial precipitates. At low sintering temperatures, a thin continuous layer around the $Nd_2Fe_{14}B$ grains prevents the demagnetization and consequently improves the coercivity. On the contrary, at the high temperatures, the precipitates formed on the surface of $Nd_2Fe_{14}B$ grains decrease the coercivity. The sintering is followed by the post-sintering process at approximately 600 °C to relieve internal stress and refine the grain-boundary texture. The final magnetic properties strongly depend on the initial chemical composition, sintering and post-sintering processing temperature [53], [56]. The typical microstructure of a sintered magnet processed by the powder metallurgy route is shown in Figure 1.14.

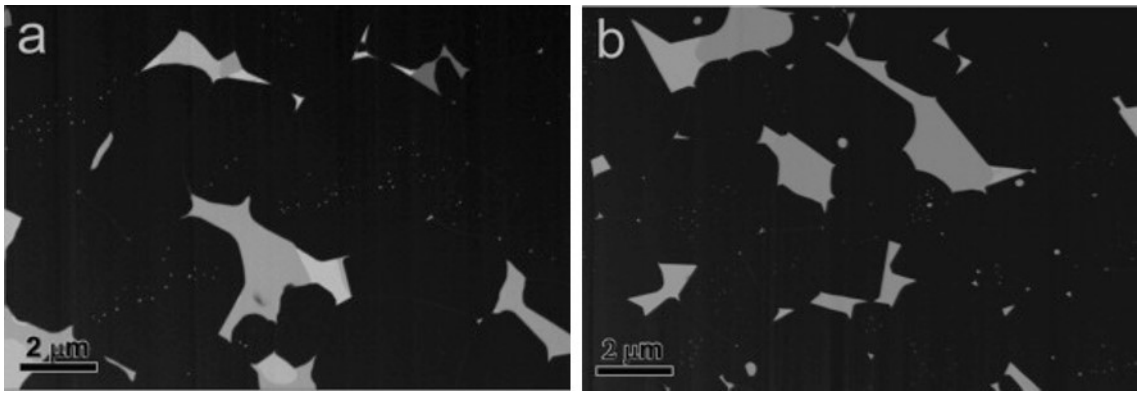

Figure 1.14: Microstructure of Nd-Fe-B sintered magnet with the grain size of 4.5 µm (a) and grain size of 3 µm (b) [57].

1.3.2 Hydrogenation-disproportionation-desorption-recombination process (HDDR)

The HDDR process stands for hydrogenation-disproportionation-desorption-recombination and is a well-established processing route for obtaining the refined grain structure of rare-earth transition-metal alloys (e.g., Nd-Fe-B alloys). The process was invented by Takeshita et al. [58] in 1989 and later on interpreted by McGuiness et al. [59], [60]. In this type of processing the magnetically anisotropic powder can be produced, however; the process is limited by the thermal stability of the powder. The process is mainly based on hydrogen-induced phase transformation, which results in highly coercive $Nd_2Fe_{14}B$ powders. This powder is the basis for the production of bonded magnets or fully-dense hot-pressed magnets [54]. The main advantage of the HDDR process is the production of anisotropic Nd-Fe-B powders by adjusting the process parameters or by aligning the c-axis of $Nd_2Fe_{14}B$ along one direction [54].

In the Nd-Fe-B system the HDDR reaction (shown in Figure 1.15) occurs in two stages and is expressed as (Eq. (1.12)) [54]:

$$Nd_2Fe_{14}B + (2 \pm x)H_2 \leftrightarrow 2NdH_{2+x} + 12Fe + Fe_2B \pm \Delta H \qquad (1.12)$$

1) *Disproportionation*: The $Nd_2Fe_{14}B$ phase disproportionate or decompose during the heat treatment at 800 °C and 1 bar of hydrogen pressure into a finely divided mixture of α-Fe, NdH_2 and Fe_2B.
2) *Desorption and Recombination*: The subsequent heat treatment under the vacuum causes the desorption of hydrogen from NdH_2. The disproportionated Fe_2B, α-Fe and Fe_2B are then recombined into the $Nd_2Fe_{14}B$ phase. The new recombined phase possesses a much finer grain structure compared to the initial $Nd_2Fe_{14}B$ phase [54].

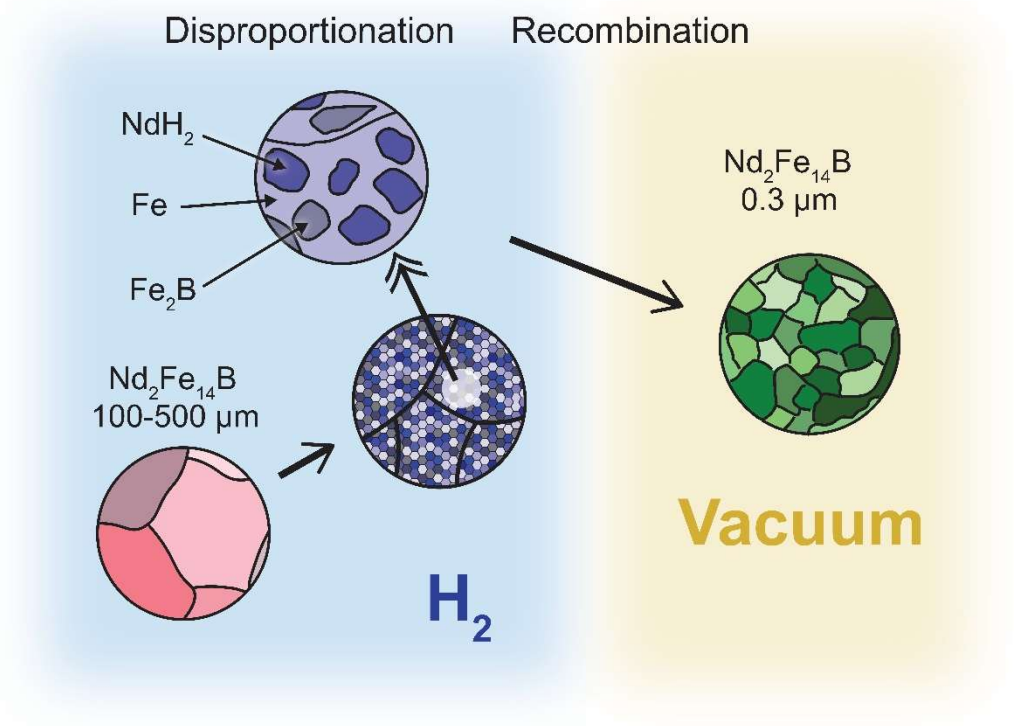

Figure 1.15: Schematic figure of HDDR processing of $Nd_2Fe_{14}B$ powder [54].

The HDDR process reduces the grain size of the $Nd_2F_{14}B$ powder from 100 μm to approximately 0.3 μm, which is close to the single domain size of the $Nd_2Fe_{14}B$ phase. The additional heat-treatment of HDDR powder leads to iron-free uniformly fine-grained microstructure with excellent magnetic properties [61], [62]. With small additions of Zr, Co or Ga, magnetic anisotropy is induced by altering kinetics which results in anisotropic powder with well-textured grains [63], [64]. The additives of Co and Ga impact the recombination time and temperature meanwhile the Zr addition improves the coercivity and reduces the grain size [65]–[67]. Alternatively, the anisotropic HDDR powder can be processed without kinetic-altering addition by controlling the hydrogen pressure under certain condition during the HDDR process [68], [69]. Honkura et al. processed the anisotropic HDDR powder by so-called ''dynamic-hydrogenation disproportionation desorption recombination'' (d-HDDR) process, where the anisotropy rate was determined based on the rate of the reaction between $Nd_2Fe_{14}B$ phase and hydrogen [68].

1.3.3 Rapid-solidification technique

The rapid-solidification process is an important area in solidification processing and becomes an important technique in industrial use. Since the 1970s, especially after the discovery of the first amorphous alloy produced by this technique, the field of rapidly solidified metals and alloys has grown quickly. Rapid solidification is a rapid extraction of thermal energy during the transition from a liquid state (high temperature), to the solid-state material (room temperature). This process affects phase equilibrium and can be considered as nonequilibrium cooling because the cooling rates are very high ~10^3 –10^9 K/s. Consequently, the alloys processed by the rapid-solidification technique exhibit better properties due to the small grain size and improved microstructure [54], [70], [71].

This process can be used to make an amorphous material instead of a crystalline material because it controls the kinetics of crystallization. It also permits large deviations from phase equilibrium, which can enhance compositional flexibility, extends the solid solubility, and the formation of non-equilibrium phase. Over the past four decades, rapid solidification resulted in a broad spectrum of solidification techniques that brought many commercially available products [70].

1.3.4 Melt-spinning (continuous) process

The melt-spinning technique (Figure 1.16) is the most used rapid-solidification process and the most appropriate technique to produce large quantities of ribbons. The simplest version of this technique was invented back in 1872, when the first ribbons were produced. The improved versions such as chill-block (similar to modern single-roller melt spinner) and free-flight melt spinner (jet of the molten alloy is solidified by the surrounding gas) were discovered in 1908 and 1961. A similar version to the modern single-roller melt spinner was invented at the California Institute of Technology in 1958 by Pond et al., who firstly directed a molten stream on the inner surface of a rotating rim. This modern single-roller melt spinner was assembled by a solid copper quench wheel combined with a quartz containment crucible. The alloy in the crucible was melted by induction heating and forced out of the crucible using pressurized gas. The speed of the quench was carefully controlled since the grain size is strongly related to the wheel speed [19], [54].

The main advantages of the melt-spinning process in comparison with other solidification techniques in terms of the microstructure and phase equilibria are:

- Processing of nonequilibrium crystalline phases;
- Improved chemical homogeneity with an increase of the cooling rate;
- The formation of non-equilibrium glassy phases;

- The grain size reduction with increasing of the cooling rate and achievement of nanoscale microstructure;
- Homogeneity and solubility area of equilibrium phases are extended with increasing of the cooling rate [54].

From the perspective of $Nd_2Fe_{14}B$ magnets, the melt-spun Nd-Fe-B ribbons were discovered by Croat and Herbst in General motors [30]. The development of melt-spun ribbons ran parallel to the development of sintered Nd-Fe-B magnets discovered by Sagawa at Sumitomo [32]. In this process, shown in Figure 1.16, a thin stream of molten Nd-Fe-B alloy (melted by induction heating) is ejected through the small bore at the bottom of the quartz crucible on the surface of a rapidly rotating Cu wheel. When the molten alloy impacts the cooling surface of the rotating Cu wheel, it spreads and solidifies at high velocity (~10^5–10^6 K/s) into the thin ribbons, which leave the wheel tangentially to a chamber from where the melt-spun ribbons are collected [54]. $Nd_2Fe_{14}B$ ribbons, processed at optimal quench rates, are composed of crystalline polygonal grains ranging from few tens of nanometers in the wheel side to 1 μm in the free side [54], [71], [72]. The high cooling rates prevent the grain growth and formation of α-Fe, which deteriorate the magnetic properties [19].

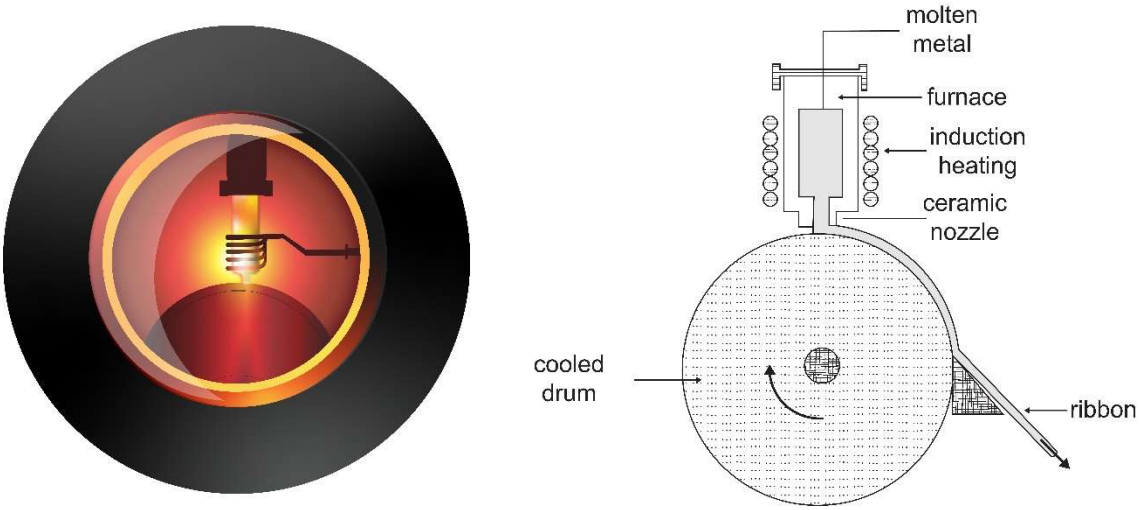

Figure 1.16: Schematic representation of the melt spinning technique [73].

Croat et al. proved that melt-spun ribbons are magnetically and crystallographically isotropic and therefore their demagnetization curve is not square-shaped like in the case of an anisotropic material. In contrast, this type of material exhibits a monotonic change of magnetization versus the applied field. They processed series of $Nd_{0.15}(Fe_{1-y}B_y)_{0.85}$ alloys at different wheel velocities and measured their coercivities shown in
Figure 1.17. They found that the maximum coercivity is reached at a velocity between 15 and 20 m/s, meanwhile, over-quenched (finer grains or amorphous) or under-quenched ribbons (larger grains) showed a much lower value of coercivity. Another important factor is the boron content, which also has a significant impact on the coercivity of melt-spun ribbons. The alloys with boron content between 0.5 and 0.9 show the highest coercivities between 1.7 and 2 T. The enhancement of coercivity with increasing boron content in melt-spun ribbons is the result of an increase in the volume content of a major $Nd_2Fe_{14}B$ intermetallic and a minor Nd-rich intergranular phases in the microstructure at the expense of the equilibrium of α-Fe and Nd_2Fe_{17} phases [19].

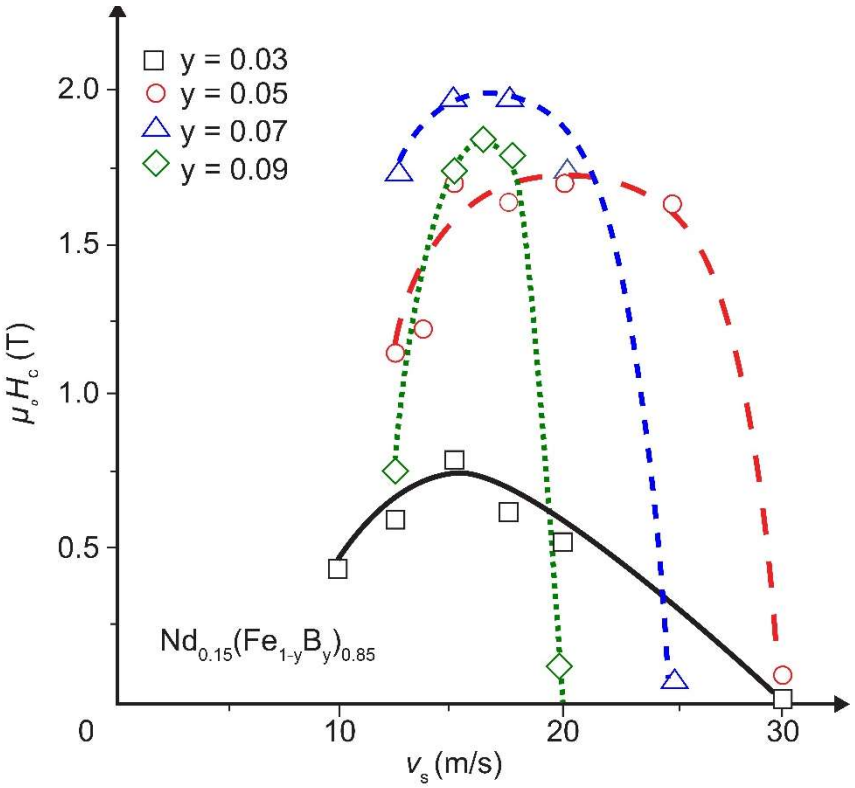

Figure 1.17: The coercivity of $Nd_{0.15}(Fe_{1-y}B_y)_{0.85}$ alloys versus wheel speed [19], [30].

1.3.5 Gas-atomization

An alternative method to HDDR and melt-spinning process is the gas-atomization technique. This is the oldest technique of the rapid-solidification processes [74] that enables the processing of nanocrystalline Nd-Fe-B powder with an average size of 20 um. Although the melt-spinning process is industrially the most important route, gas atomization is an appropriate technique for forming a microstructure at the cooling rates 1 to 2 orders of magnitude lower regarding the cooling rates in the melt spinning technique (10^6 K/s). The gas atomization technique shows great commercial potential due to its ability for high-volume, low-cost production. The gas atomized Nd-Fe-B powder is especially used for bonded magnets, due to the high tap density and powder flow characteristics [75].

It is a versatile method for powder production, schematically shown in Figure 1.18. A high-pressure inert gas (argon or helium) is used to break up the molten stream of alloy into fine droplets, which eventually solidify into fine particles with cooling rates from 10^4 to 10^5 K/s. The primary objective of this process is producing a fine dispersion of droplets that have good thermal contact with the inert gas and at the same time to destabilize a thin liquid film. The process occurs due to the transfer of kinetic energy from atomizing fluid to the melt. When the gas-stream velocity exceeds surface tension, which keeps the liquid unified, the stream of molten alloy disintegrates. The formation of waves in the shape of the rod is caused by the interaction between gas jets and alloy stream. The waves propagate which leads to perforations and results in the break-up of the stream into the fine droplets. Each experiment of this technique begins with bulk material and finishes with a collection of fine particles [54], [71]. The most important objectives of the atomization process are:

- To reduce the particle size;
- To minimize the average particle size;

- To produce complex melt systems for powder applications.

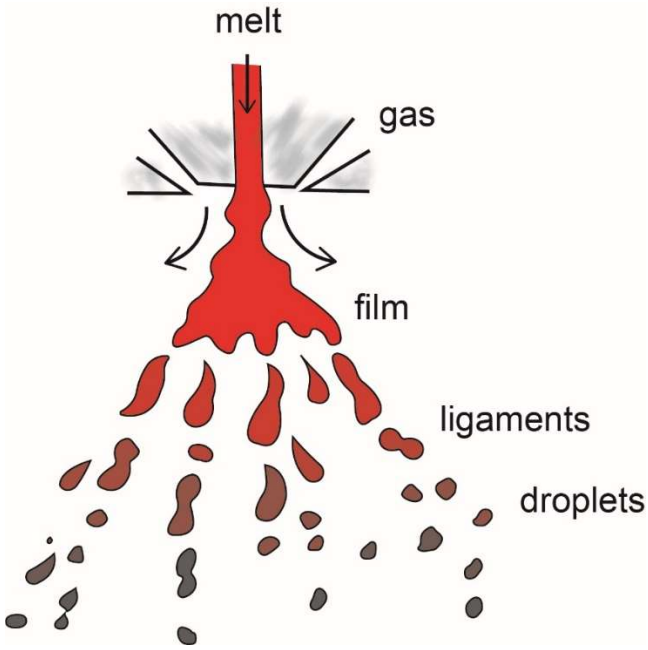

Figure 1.18: Schematic presentation of the atomization technique [76].

The microstructural development of Nd-Fe-B gas-atomized powder primarily depends on the cooling rate. The particle size is consistent with the solidification rate [77]. Based on the particle size and cooling rate, characteristically different microstructures were found:

1) A partition less structure with no visible microsegregation is formed within the finest particles (< 10 µm). Depends on the rate of heat extraction, this structure can be formed in a glassy or crystalline state. An amorphous fraction was also found in this microstructure.
2) In the particle size between 10 and 15 µm, a two-phase cellular microstructure (Figure 1.19a) is formed with $Nd_2Fe_{14}B$ as the primary phase and the rare-earth-rich eutectic as the grain-boundary phase. An equiaxed grain microstructure is a result of a spherical growth morphology that is developed under the critical amount of undercooling.
3) In particles with a size between 15 and 90 µm, a dendritic microstructure (Figure 1.19b) with nucleation sites at the surface and interior of the particles is found. The dendritic growth begins from the heterogeneous nucleation sites and continues with the growth of dendritic arms at the tips which results in a starburst morphology.

The largest particles above 90 µm also have a dendritic microstructure with different morphology. Instead of starburst morphology is in this case fern morphology (Figure 1.19c), which is a consequence of the formation of secondary dendrite arms due to slow growth rate and low undercooling [75].

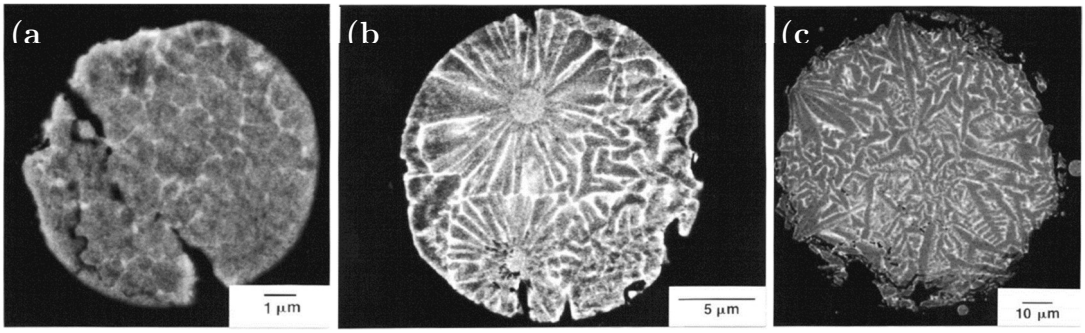

Figure 1.19: A BSE (backscattered electron) image of gas atomized $Nd_2Fe_{14}B$ powder with: a) cellular morphology, b) starburst dendritic morphology, and c) fern dendritic morphology [75].

The main problem of this technique is a production of a spectrum of particle sizes with a non-uniform microstructure (Figure 1.20), which affects the intrinsic and extrinsic magnetic properties. Lewis et al. also found that larger particles contain pure α-Fe, a soft-magnetic material, which causes the degradation of coercivity and makes the main $Nd_2Fe_{14}B$ phase nonstoichiometric. This implies a strong connection between the grain size and intrinsic coercivity which is the largest in the smallest nanocrystalline spheres [75], [77], [78].

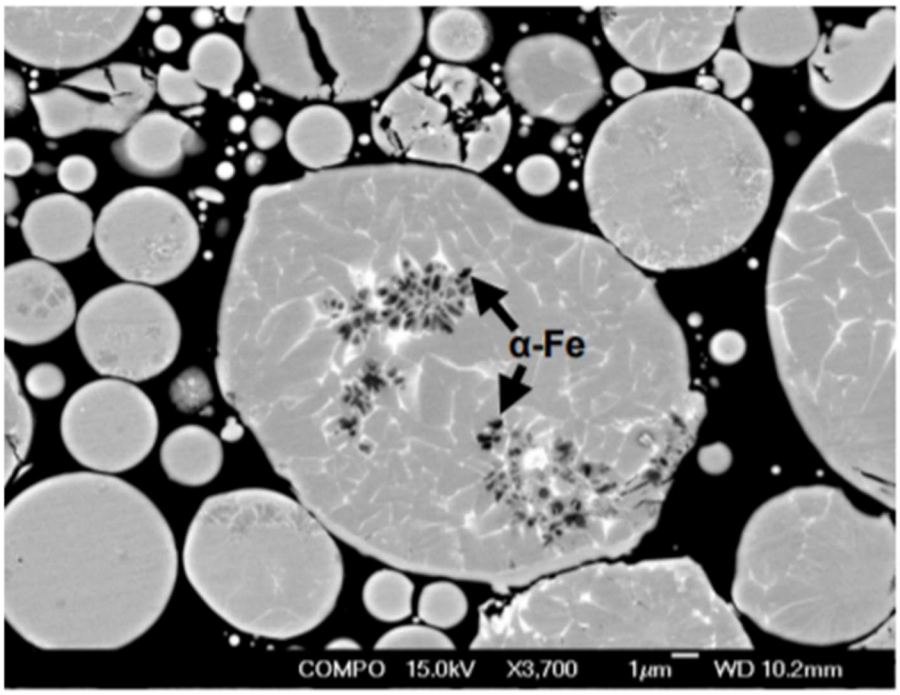

Figure 1.20: The microstructure of Nd-Fe-B gas atomized powder [79].

1.3.6 Mechanical alloying

Two important processes are involved in mechanical alloying: a high-energy ball milling and subsequent annealing treatment. In this process, the diffusion-reaction causes the mixing of different elements and forms an ultrafine layered structure of composite particles. The formation of the desired alloy depends on the alloy thermodynamics, mechanical processing of the initial material and the energy required for the ball-milling process. The main advantage of mechanical alloying is the formation of metastable phases during the

processing because it is a nonequilibrium technique and it can overcome many limitations of conventional milling processes [54].

In the case of the Nd-Fe-B system, during the ball milling, a layered structure of Nd and Fe is formed. The B particles are undeformed and embedded along the interfaces. The ball milling is followed by the heat treatment at 600 to 700 °C for a maximum of 30 minutes. During this process, a hard magnetic $Nd_2Fe_{14}B$ phase with a crystallite size of 10–50 nm is formed from ultrafine and homogeneously distributed reactant particles [54], [80].

A modified version of mechanical alloying named "intensive milled technique" was reported by Gutfleisch et al. [80], where they used it as a starting material for ball milling an alloy powder instead of elemental powder. The powder after using "intensive milled technique" showed higher coercivity than powder processed by mechanical alloying (mechanically alloyed nanocomposite powders of $Nd_2Fe_{14}B/\alpha$-Fe with additional elements).

1.4 Bulk Magnets from Melt-Spun Nd-Fe-B Ribbons

In the following chapter, the processing routes for bulk Nd-Fe-B magnets from melt-spun Nd-Fe-B ribbons will be presented. Two typical processing techniques will be described below.

1.4.1 Polymer bonded magnets

Bonded magnets are magnets that consist of at least two components – a magnetic powder and a non-magnetic binder. They can be used in a wide range of applications. The large growth of the personal computer industry and related technology and automotive industry has significantly increased the demand for polymer-bonded magnets. The manufacturing of bonded magnets is near net shape production which is the major advantage over the powder metallurgical process because the processing requires zero or minimal finishing operations [81]. However, due to increased demand, the magnetic powder producers need to constantly improve their products and manufacturing method to provide the best properties of the final polymer-bonded magnet [82], [83]. There are several manufacturing methods for processing the magnetic powder for bonded magnets:

- crushing of bulk magnet or alloy ingot;
- a direct chemical reaction to a powder product;
- melt-spinning processing;
- HDDR processing;
- gas atomization processing;
- mechanical alloying.

The powder can be hard ferrite, Nd-Fe-B, $SmCo_5$, Sm_2Co_{17}, SmFeN, Alnico or a mixture of two or more different magnetic powders. The powders have specific magnetic properties obtained by the chosen chemical composition and optimized process path for use in polymer-bonded magnets. The type of magnetic powder is identified based on the desired application of the final product [81]. On the other hand, two types of binders fix the magnetic material – flexible and rigid. Typical binders for flexible magnets are vinyl and nitrile rubber, meanwhile, the binders for rigid magnets are nylon, polyphenylene sulfide, polyester, Teflon and thermoset epoxies [81]. There are several different processing routes for the production which are described below.

In the injection-moulding process, a highly filled thermoplastics molten compound is injected into the mould cavities, where it is cooled and solidified. For this type of processing of bonded magnets, the ferrites and Nd-Fe-B are the most commonly used magnetic powders. To achieve high-volume output and productivity, multi-cavity tooling is used for

processing the bonded magnets. The injection-moulding process also enables the production of complex-shaped and multi-component to assemble magnets. On the other hand, the powder loading is limited to 60-65 vol.% and the tooling is expensive. Due to the high investment and the lack of standards, the applications are limited to mass parts [81], [82].

The extrusion process enables comparable maximum loading (65 vol.%) to that of the injection-moulding process, meanwhile, the initial material is similar to that used in calendaring processing. Here, the main screw in combination with the heated barrel works against the compound to push it with high pressure through a heated die. The product, i.e., a strip of material, can be cut into pieces, coiled in a spool or collected in a cut sheet [81], [82].

In the calendaring process a series of rolls reducing the thickness of sheets which are passed through several times to about 1–10 mm. The low loading of only 55 vol.% results in flexibility of the final product, which is a suitable property for applications like advertising, toys and clamping devices. The maximum temperatures of the calendaring processing depends on the type of the binder and are typically between 80 and 130 °C [82]. The bonded magnet manufacturing route of all three above-described processes is shown in Figure 1.21.

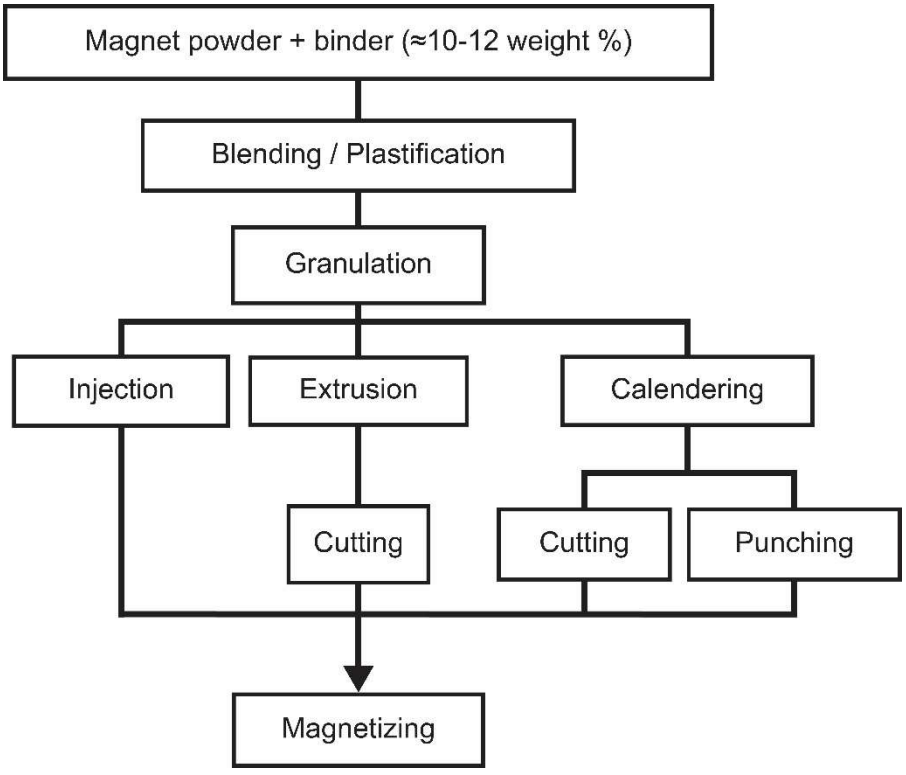

Figure 1.21: Production processing routes for injection moulding, extrusion and calendaring [82].

The fourth processing route for bonded magnets is compression moulding with moderate tooling costs, a short economic cycle process and a maximum loading of 85 vol.%, which results in higher flux densities of the final product regarding the other three techniques described above. The process starts with the refinement step and liquid encapsulating processing of Nd-Fe-B powder to coat each particle with a thin film of thermoset epoxy, hardener and other additives. In the next step, the so-prepared powder is fed into the press cavity and pressed into a compacted magnet and subsequently heat-treated at about 150 to 180 °C. The production of near-net-shape compression-bonded Nd-Fe-B magnets

together with a high maximum energy product make these magnets useful for numerous applications in brushless DC motors, spindle motors and other motor applications [81], [82]. The compression moulding processing route is shown in Figure 1.22.

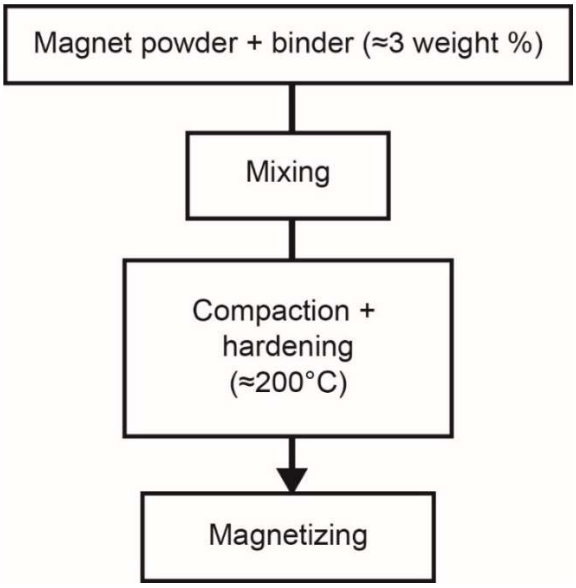

Figure 1.22: Production processing route of compression-moulding process [82].

In the case of Nd-Fe-B magnets, the melt-spun ribbons are mainly used for processing bonded magnets. The produced ribbons are ground to a particle size of less than 400 µm and subsequently post-annealed to develop the desired microstructure and magnetic properties. The magnetic powder is then mixed with polymer (thermal-set or thermal-plastic) and the mixture is compressed or injection moulded with an appropriate tool to produce a near-net shape polymer-bonded magnet with a microstructure shown in Figure 1.23. The several different polymers (polyamides or polyphenylene sulfide) with a loading factor from 50 to 75 % can be employed by the injection-moulding technique. A polymer-bonded magnet produced by injection-moulding possesses a remanent magnetization between 0.5 and 0.6 T and a maximum energy product between 40 and 55 kJ/m^3. This method enables the production in a variety of different shapes for a high spectrum of

applications. Another technique is compression-moulding, which in combination with an epoxy polymer results in the highest volumetric fraction of magnetic powder with the remanent magnetization between 0.62 and 0.72 T and maximum energy product between 48 and 85 kJ/m^3. The better magnetic properties of polymer-bonded magnet processed by compression moulding technique are the consequence of higher volume fraction of magnetic powder; however, despite inferior properties, the injection-moulding technique is still very attractive [83], [84].

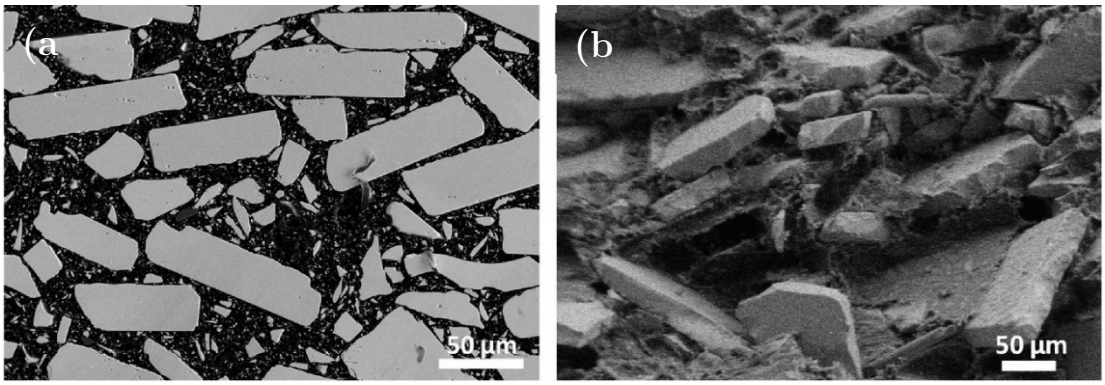

Figure 1.23: Microstructure of Nd-Fe-B polymer-bonded magnet of (a) cross-section and (b) fractured surface [85].

Recently, the extrusion and calendaring method also take a place in the processing of Nd-Fe-B polymer-bonded magnets. These two methods enable the production of mechanically flexible Nd-Fe-B polymer magnets with a desirable shape for a specific type of application. The magnets processed by calendaring have a lower remanent magnetization and maximum energy product than magnets processed by compression, injection moulding or extrusion due to the low-loading factors. That is why the moulding method should be carefully chosen for a specific type of application based on coercivity, remanent magnetization, maximum energy product and temperature characteristics of the final polymer-bonded magnet [83].

1.4.2 Hot-pressing technique vs Spark plasma sintering

The hot-pressing (HP) technique (Figure 1.24) is a common method for processing dense magnets from magnetic powder. The temperature and pressure are simultaneously applied to a powder compact, which is an advantage compared to conventional sintering methods because it allows processing at lower temperatures and shorter times to inhibit the grain growth during consolidation and maintain the excellent magnetic properties. The powder container is usually heated by radiation through external heating elements like a copper coil and by the convection of inert gases, which means that the heat is transferred to the sample by conduction from the surface of the powder container to the sample. All the processing parameters – temperature, pressure, heating rate, atmosphere and holding time affect the microstructure and properties of the final bulk sample [86], [87].

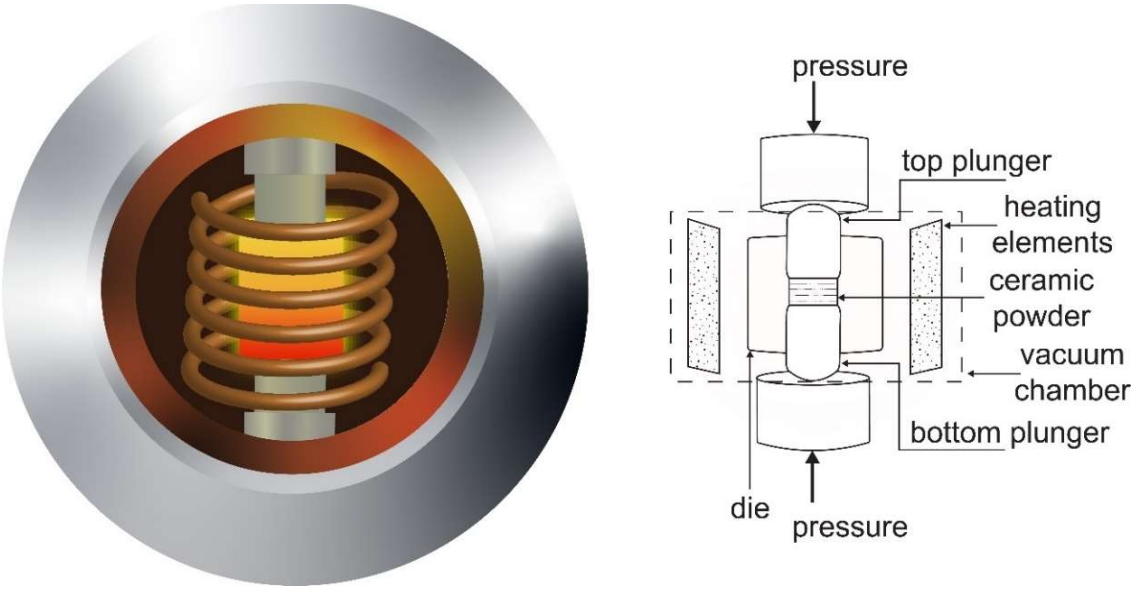

Figure 1.24: Schematic presentation of a hot-pressing (HP) process [86].

On the other hand, the spark-plasma-sintering method (SPS), also known as field-activated sintering method or pulsed electric sintering method, is an advanced sintering technique utilizing uniaxial force and pulsed (on-off) direct electrical current that enables high-speed consolidation of the powder and processing of high-temperature materials with poor deformability into configurations which are unfeasible with other sintering methods. The direct way of heating provides high heating and cooling rates and improves the densification over grain-growth-promoting diffusion mechanisms. Besides, it enables the maintenance of the intrinsic properties of the nano-powders in their fully dense bulk samples [87].

This type of sintering was first mentioned and patented back in 1913. The patent concerned the current- and pressure-assisted sintering system in a vacuum. First SPS model was developed in 1930, however, this device was not appropriate for commercial use. In the 1960s the Kiyoshi Inoue invented spark plasma sintering, where the heating was applied by pulsed current; however, he failed to commercialize the device successfully. At the end of 1970s, the Inoue's method was used for processing near-net-shape products, large components, functionally graded materials and non-equilibrium composites. In 1980, the technique was developed even further, especially in Japan, where they started to use it frequently in the laboratory. In the early 1990s, this technology became commercially available and Japanese companies first started producing SPS devices. Several years later, US companies started with the production of the upgraded version of SPS devices based on pulsed direct electric current. Today there are on the market several FAST/SPS devices which provide excellent conditions for sintering [88].

The SPS technique is suitable for processing a broad range of powders like pure metals, alloys, ceramics to produce bulk specimens. The initial powder is usually placed in a graphite mould and during the sintering, the pressure and electric current are applied to improve the densification process of the powder into the bulk sample. The method is very similar to conventional HP; however, the main difference is in the heating of the sample. In this case, instead of using an external source for heating, the sample is heated by radiation or induction. The pulsed electric current is applied in the millisecond range via the conductive (usual graphite) mould and directly through the sample (Figure 1.25). The powders are heated from both inside and outside due to the generated electric field, which is a result of the applied pulsed direct current [88], [89].

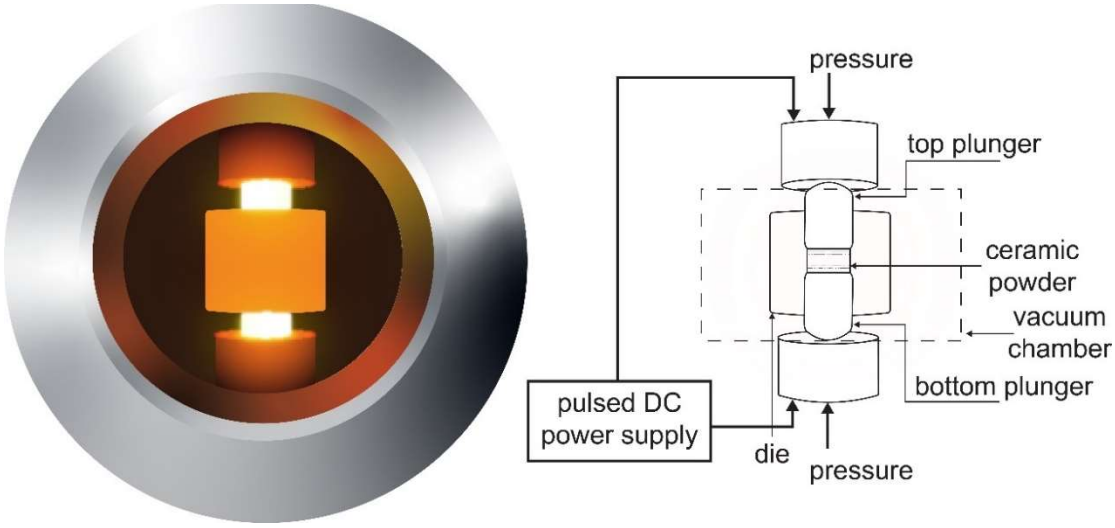

Figure 1.25: Schematic presentation SPS process [86].

As mentioned above, the SPS method is similar to HP from the perspective of the appliance of mechanical pressure on the sample during densification; however, with heating rates incomparably higher (up to 1000 °C/min) compared to HP (≈5–10°C/min). Besides, simultaneous sintering and pressing enable fast densification at low sintering temperatures (200–300°C lower compared to other conventional sintering techniques) and short holding times (0–10min) which makes SPS the most popular fast-sintering method for the processing of nanostructured materials, amorphous materials, ceramic composites and highly refractory metals [90], [91]. When heating is established, the heating power is not only distributed over the volume of the powder sample homogenously, it is also dispersed at contact points of the powder particles where the energy is required for the sintering process. The result of heating power distribution is a favourable sintering processing with inhibited grain growth and suppressed powder decomposition [87].

On the other hand, adequate electrical conductivity of the initial powders is required for SPS processing. Besides, the main deficiency is the inhomogeneous temperature distribution through the whole sample, which is reflected in larger temperature gradients. The consequence of the temperature gradients is inhomogeneous sintering behaviour which affects the properties of the final product. To minimize the temperature gradients inside the sample during the SPS processing, the following parameters of the initial powder which determine the temperature distribution should be considered [87]:

- The electrical conductivity;
- The mould thicknesses;
- The presence of the graphite paper:
    - Preventing direct contact between the sample and graphite parts;
    - Providing the electrical contacts between all the parts [87].

1.4.2.1 The mechanism of the SPS process

The electric discharge phenomenon is the basis of the SPS. A low-voltage spark pulse current with high energy momentarily generates a spark-plasma at high localized temperatures. The temperatures between the particles ranging up to ten thousand degrees Celsius and result in optimal electrocatalytic and thermal diffusion. The lower sintering temperatures and shorter holding times compared to conventional sintering techniques are explained by the following mechanisms [87].

1.4.2.1.1 Plasma generation

In 1965 Inoue et al. [92] firstly named this method as spark plasma sintering and plasma active sintering due to the pulses that generate the sparks and plasma discharges between the contacts of the particles. They set up a theory that spark discharges caused by ionization at the particle contact develop impulsive pressures, which enables easier diffusion of the atoms at contacts. Later, Groza et al. [93] claimed that the formation of oxygen-free grain boundaries between the grains is a consequence of a pulsed current, which has a cleaning effect on the particle surfaces. However, there is still no experimental evidence of plasma generation or its effect in SPS. Meanwhile, the occurrence of plasma discharge has been confirmed by electric discharges occurred on microscopic level [87].

1.4.2.1.2 Joule heating

Another possible mechanism is Joule heating - a typical heat-generation mechanism in the case of using metals as the initial material. It occurs due to the resistance of electric current, which achieves its the maximum value at the particle contacts. At the beginning of the process, there are many contacts between the particle conducting surfaces; however, with the densification progress, these contacts start to vanish due to the pore closure. The result of the disappearance of the contacts is decreasing and at the end, when the material attains full-density, vanishing of the electrical resistance. In this electrical path, the resistances from graphite-mould punch system and the graphite foil-powder contacts is also included [87], [94].

1.4.2.1.3 Pulsed current

In the SPS device, the high-amperage pulsed DC is utilized to consolidate the powder during the SPS processing. This pulsed DC is a periodically repeatable current with varying value and a constant direction and could be described as a signal that consists of one or more rectangular pulses. The ON-OFF DC-pulse method generates the following phenomena [95]:

- spark plasma;
- Joule heating;
- spark impact pressure;
- electrical field diffusion effect.

All of these phenomena have special effects and, in the end, a practical advantage which is shown in Figure 1.26.

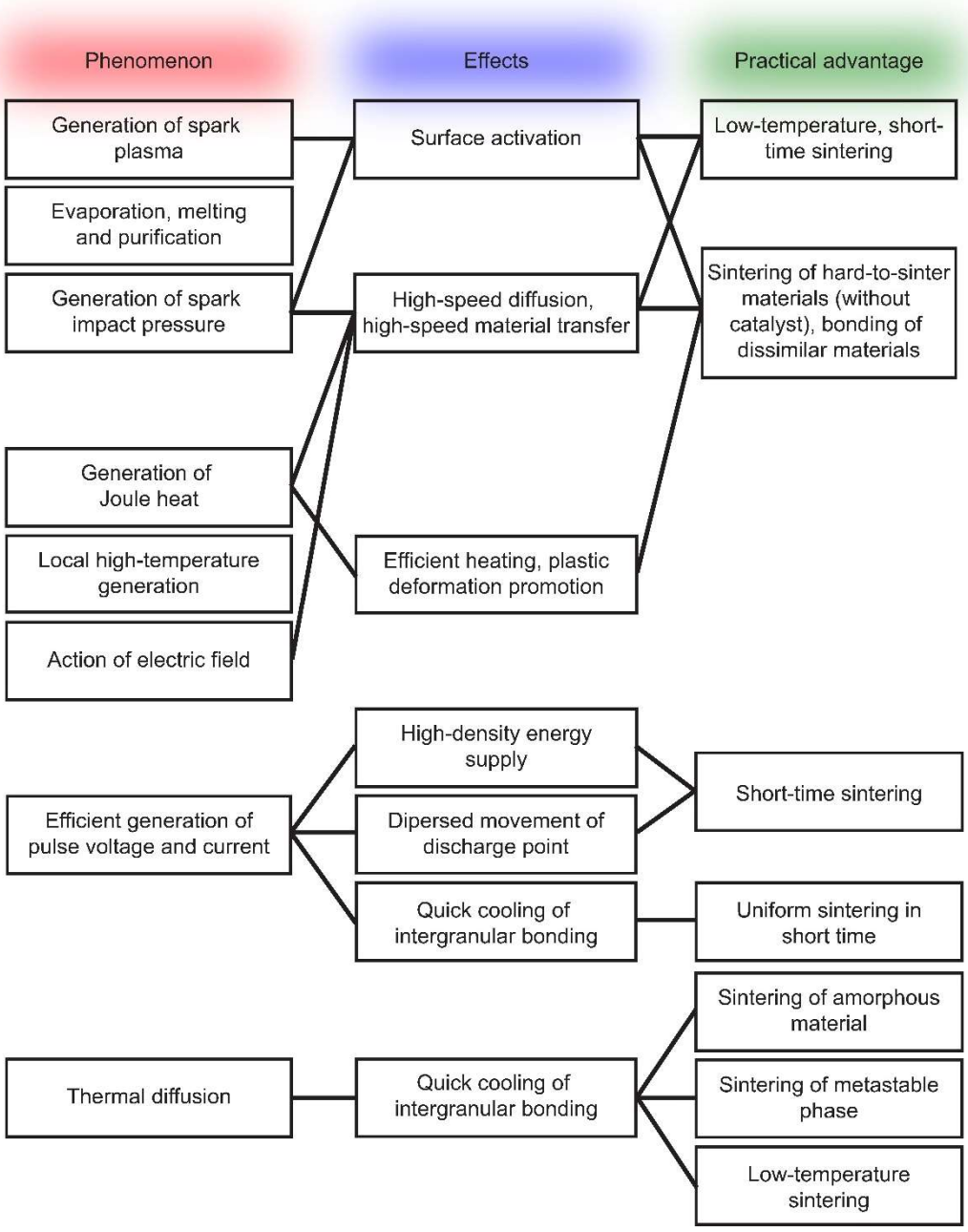

Figure 1.26: Generated phenomena by pulsed SPS ON-OFF DC, their effects and practical advantage [87].

As mentioned in the previous section, in the SPS process a bulk sintered compact is made at a lower sintering temperature with a shorter holding time in comparison with conventional sintering methods. It is easier to purify and activate the surfaces of the initial powder particle and promote material transfer at the macro- and micro-level [87]. Figure 1.27 (a) shows the flow of pulse current through the powder particles inside the mould. A special pulse generator (Figure 1.27 (b)) applies ON-OFF DC-pulse voltage and current to powder particles and effectively generates the electrical discharges between the particles, which enables sintering in the initial stages [95].

The spark plasma and spark impact pressure generate high-temperature sputtering, which eliminates the impurities from the surface of the powder particles. The high-speed diffusion is a result of the rapid migration of ions which is caused by an electrical field.

The time of the pause and applied DC pulse last for a few to tens of millions of milliseconds. A sintering process is conducted in either vacuum, low pressure or inert gas atmosphere at a low applied voltage (few volts) and high applied current (few thousand amperes) [95].

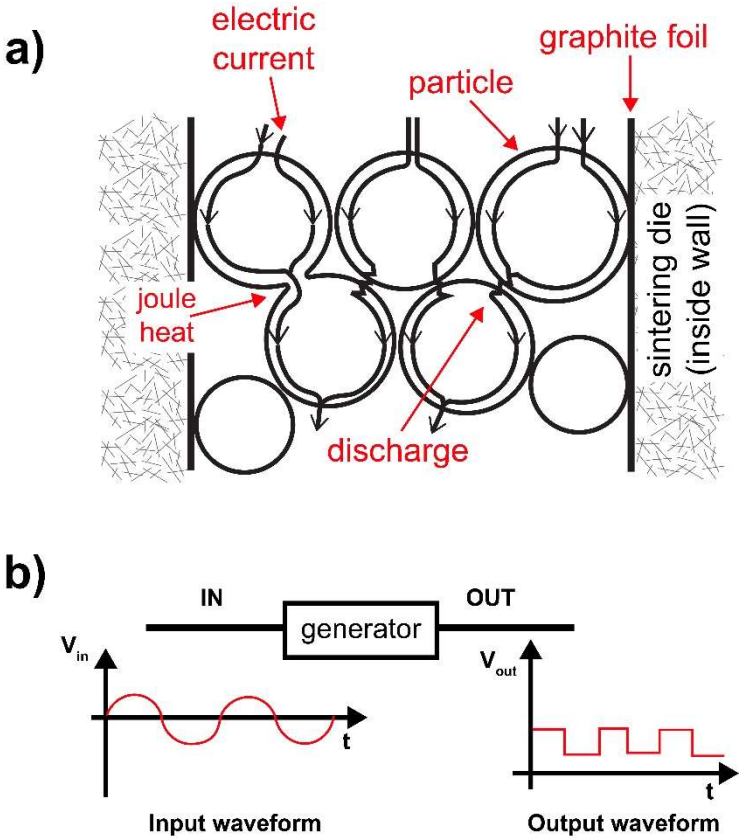

Figure 1.27: The flow of pulsed current through the particles [87], and pulsed DC generator [95].

1.4.2.2 Hot-pressed and hot-deformation process

In 1985, R.W. Lee [96] developed a new method where the fully dense well-aligned Nd-Fe-B magnets were processed in two steps from melt-spun powder. In the first step, a hot-pressing (HP) or spark-plasma-sintering technique is used to produce a fully dense, hot-pressed magnet at ~ 700 °C and 50 MPa. In this step, the coercivity reaches a typical value of ~ 1500 kA/m (1.9 T) and the remanent magnetization of about half of magnetization saturation, i.e., ~ 0.8 T [97]. The $(BH)_{max}$ is, in this case, above 110 kJ/m^3 [98]. The microstructure of the HP magnet is quite isotropic and uniform throughout the entire magnet. It consists of randomly orientated polygonal $Nd_2Fe_{14}B$ grains with sharp boundaries and sizes between 80 to 100 nm [99]. The typical microstructure of the HP magnet is shown in Figure 1.28 (a), (b).

The HP is followed by hot-deformation (HD) at approximately 750—800 °C, with a strain rate of 0.001 s^{-1}. During the HD process, the equiaxed grains are changed to anisotropic platelet-like shape structures. Due to the anisotropic grain growth and the grain-boundary sliding, the *c*-axes of the grains are aligned parallel to the pressing direction. The best magnetic properties have been obtained in the HD process at 800 °C with the 73 % height reduction of the final magnet. The remanent flux density has been improved to the typical values of 1.3—1.5 T, while the coercivity is decreased to

~ 1000 kA/m (1.25 T). However, the $(BH)_{max}$ is usually increased to above 400 kJ/m^3, which is proof that the HD process greatly improves the magnetic properties.

During the HD process, the oxidation of the metallic Nd-rich phase is extremely suppressed. The main reason for this is the size of the ribbons (~ 150 um), which is around 100 times larger than jet-milled powders for sintered magnets [100]. During this process, a strongly oriented (001) texture with plate-like shape grains is developed due to the grain boundary sliding and the anisotropic grain growth of the tetragonal $Nd_2Fe_{14}B$ phase [99], [101]–[103]. The typical microstructure with ultrafine, near-single-domain size [96] of HD magnet is shown in Figure 1.28 (c), (d). However, two distinguishable zones with different grain shapes and sizes are formed [104]. In the vicinity of the ribbon interface are coarse grains areas, while, in the inner part of the ribbons, fine-textured platelet-like grains can be found [97]. The excellent magnetic properties, especially high $(BH)_{max}$, is a consequence of the strongly textured microstructure [105].

The coercivity is strongly related to the grain size and the chemical composition of the HD magnets [106]. In this case, the coercivity is fairly low for the single-domain-size grains. It is comparable to a sintered magnet with a grain size of ~ 5 μm [107]. The reason for low coercivity is the lack of a non-ferromagnetic phase around the hard ferromagnetic phase. To improve the coercivity, the grain boundaries must be structurally and chemically modified. The problem was solved with the addition of Dy, but the main problem of heavy rare earths is a limitation of their natural sources and the rapidly increasing price. Therefore, the research has focused on the development of heavy-rare-earth-free/lean magnets with a high coercivity. For instance, the addition of Nd to the hot-deformed magnet can enhance the coercivity, which is also sensitive to the concentration of Nd in the initial material. That is why the materials with a higher concentration of Nd can achieve better coercivity. In contrast, the drawback of adding non-ferromagnetic Nd led to decreased remanent flux density. Hence, the optimal concentration of Nd needs to be provided for the best magnetic properties [107].

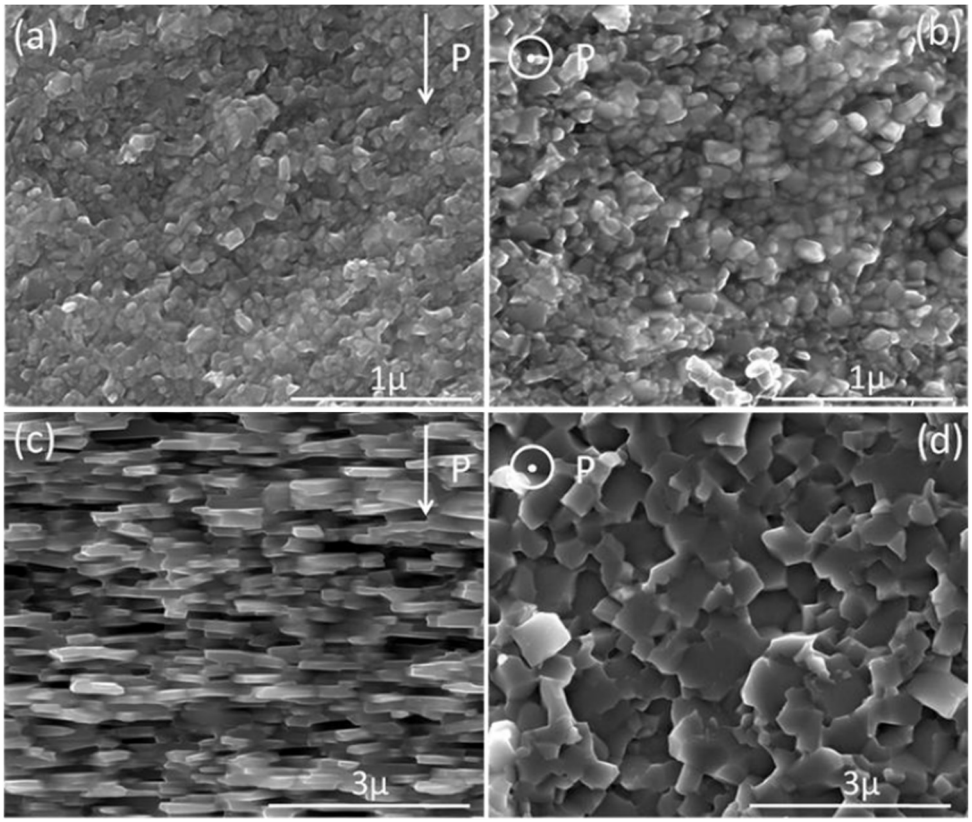

Figure 1.28: Microstructure of fractured surface of (a) and (b) hot-pressed (HP) and (c) and (d) hot-deformed (HD) Nd-Fe-B magnets obtained parallel and perpendicular to the pressing direction [108].

1.5 Coercivity-Enhancement Techniques

Nd-Fe-B magnets exhibit excellent magnetic properties with a maximum energy product as high as 474 kJ/m^3, which is close to the theoretical value of 512 kJ/m^3 [30], [37], [38], [84], [109], [110]. The superior properties are the reason for using this type of magnet in various demanding applications such as wind turbines, traction motors, electric and hybrid vehicles [111]–[113]. However, in such types of applications, the magnets need to retain the coercivity of at least 0.8 T at elevated temperatures above 150 °C to withstand the demagnetizing field [114]. Unfortunately, the current low coercivity of sintered Nd-Fe-B magnets (≈ 1.2 T) at room temperature is not enough for high-temperature applications and reduces below to 0.8 T at 150 °C due to the thermal demagnetization effect [39], [114]. The solution, to enhance the coercivity at room temperature, is to modify the microstructure either by grain-boundary engineering [103], [107], [115]–[124], heavy-rare-earth (HRE) element replacement for Nd [109], [125]–[131], by the grain-boundary diffusion process (GBDP) or grain-size refinement [57], [100], [132]–[135].

1.5.1 Grain size

Since the natural sources of Tb and Dy are limited, the processing focus should be on the HRE-free magnets or at least on magnets with a small content of HRE elements [127], [136], [137]. An effective approach to improve sintered Nd-Fe-B magnets' coercivity without using the HRE element is grain-size refinement. Several authors reported that the grain size refinement of the $Nd_2Fe_{14}B$ grains while maintaining the thin continuous Nd-rich

intergranular phase significantly enhances the coercivity of sintered magnets [133], [134], [138].

The coercivity is an extrinsic magnetic property influenced by many parameters, such as grain size, misaligned grains, magnetically coupled grains and the local magnetizing field. Nd-Fe-B magnets have a typical nucleation-type coercivity mechanism empirically determined by the effective nucleation field and the sum of the effective demagnetization field. Based on that, Kronmüller et al. proposed the following expression for coercivity (Eq. (1.13)) [139], [140]:

$$H_c = \left(\frac{2K_1}{M_S}\right)\alpha_K\alpha_\psi - N_{eff}M_s \tag{1.13}$$

where K_1 denotes the first anisotropy constant, M_s is the saturation magnetization, α_K is the nucleation effect of inhomogeneity of crystalline energy, α_ψ is the nucleation effect of misalignment grains and N_{eff} is an averaged local effective demagnetization factor. The first term of equation describes the influence of grain misalignment and defects on the anisotropy field and the second term the reduction of coercivity due to the demagnetization field [140]. The micromagnetic simulations implies that the coercivity enhancement by the grain size reduction is closely connected to the lower demagnetization factor, which means that the effective demagnetization field, $N_{eef}M_s$, decreases with grain size reduction and results in higher value of coercivity [39].

Üstüner et al. measured the grain size of sintered Nd-Fe-B magnets according to ASTM E112 standard and showed the grain size dependence on coercivity [100]. A chart of coercivity versus grain size of sintered Nd-Fe-B magnets is shown in Figure 1.29.

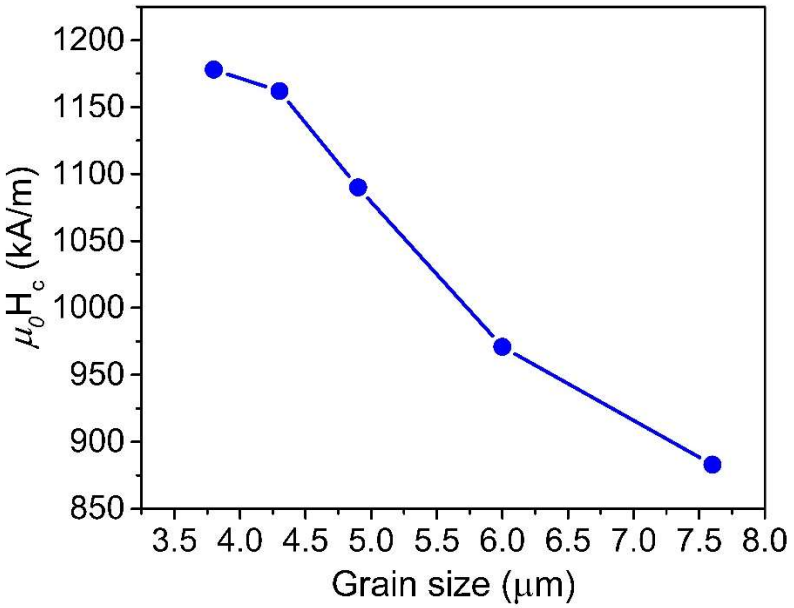

Figure 1.29: Coercivity of Nd-Fe-B sintered magnets with different grain sizes [100].

As mentioned above, in this type of permanent magnet the coercivity is controlled by nucleation of reverse domains at the surface of each individual grain [141], [142]. Due to the local demagnetizing fields and defects of the grain's surface, the nucleation field is decreased, which results in the deterioration of coercivity [141], [142]. By reducing the grain size, the probability of imperfections is lower and consequently a higher value of coercivity is achieved [100].

However, below the grain size of 3 µm, conventionally sintered magnets' coercivity values begin to deteriorate [57], [134]. To overcome this problem, Sagawa et al. presented an effective method for improving the coercivity by grain-size refinement below 3 µm [143]. They showed that with the submicron-sized jet-milled powders sintered by a press-less process (PLP), a coercivity up to 2 T could be achieved in 1-µm grain size sintered magnets [143], [144]. Further refinement of the grain size in sintered magnets showed deterioration of the coercivity due to the jet-milled powder's oxidation [136].

R.W. Lee first reported that an HD method enables the preparation of ultrafine microstructure with grain size close to the single domain size (~ 250 nm) [96]. The anisotropic HD magnet is processed from melt-spun Nd-Fe-B ribbons by HP and subsequent HD process as already mentioned in the Section 1.4.2.2. Tang et al. reported about the remanent magnetization of 1.45 T of HD magnet processed from melt-spun Nd-Fe-B ribbons with a small addition of Nb (0.29 wt. %), which is comparable to values of sintered magnets [145], [146]. On the other hand, Liu et al. showed that one magnitude order lower grain size of HD magnets enhances the temperature dependence of coercivity and makes them useful for high-temperature applications [132].

1.5.2 Heavy rare earth alloying

Another way to improve the coercivity is HRE-alloying, which means that up to 10 wt.% of HRE is added in the initial Nd-Fe-B alloy. Yan et al. [147] reported the three-stage alloying of DyH_3 and Nd-Fe-B powder mixture. During all three stages (Figure 1.30), they observed a Dy distribution in the grain boundaries. In the 1st stage of thermal treatment at 650 °C, the hydrogen was desorbed from the milled Nd-Fe-B powder and DyH_3. The result is the formation of reactive Dy, which reacts with Nd-rich material and with the matrix $Nd_2Fe_{14}B$ phase. It is expected that Dy would firstly react with a molten Nd-rich intergranular phase and after that diffusing and substituting for Nd in the matrix phase. In the 2nd stage, as the temperature increases, Dy starts to substitute for Nd at the edge of $Nd_2Fe_{14}B$ grains and starting to form the $(Nd_xDy_{1-x})_2Fe_{14}B$ phase. In the last stage, sintering temperature and dwell-time increase further, as the composition steadily becomes more and more homogenous and Dy-lean zones shrink due to Dy diffusion into the matrix phase [147].

Even though the reports show an enhancement of coercivity, this type of processing has two major drawbacks:

- it is expensive due to the high market price of HRE [148],
- a relatively large addition of HRE decreases the remanent magnetization because of the antiferromagnetic coupling between the added HRE and Fe [147], [149].

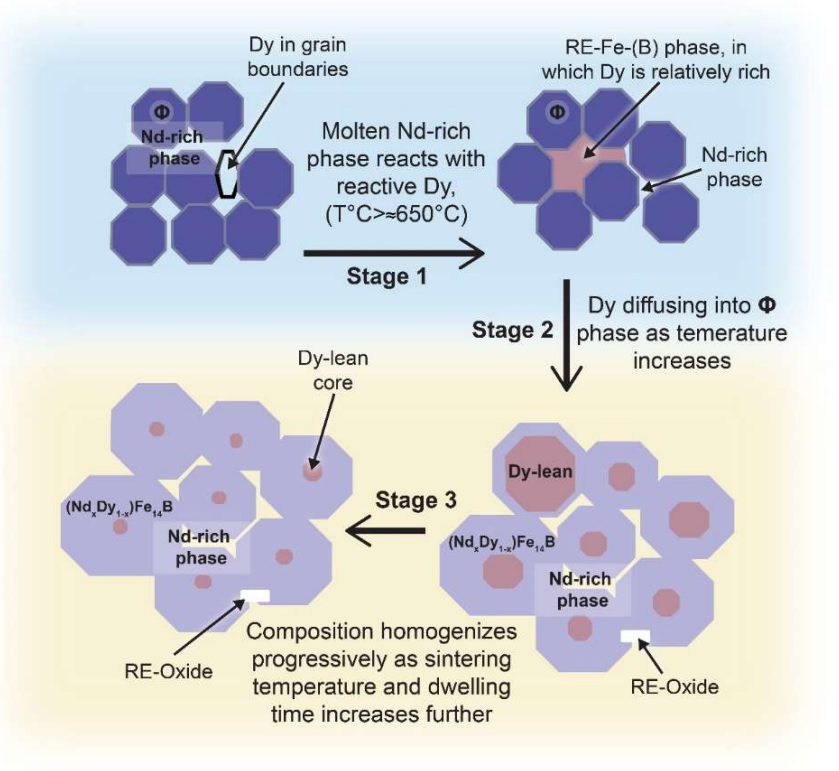

Figure 1.30: Schematic diagram of the diffusion between HRE particle and $Nd_2Fe_{14}B$ grain during sintering [147].

1.5.3 Grain-boundary engineering and GBDP

To reduce the HRE consumption for the purpose of improving the coercivity, Hirosawa et al. found a solution to enhance the coercivity of sintered Nd-Fe-B magnets by a heavy-rare-earth grain-boundary diffusion process where the Nd in the $Nd_2Fe_{14}B$ phase is partially substituted with heavy rare earth Dy/Tb, which increases the magnetocrystalline anisotropy of the $(Nd,Dy/Tb)_2Fe_{14}B$ phase (Figure 1.31) [36]. Žagar et al. [150] recently did a detailed investigation of the core-shell formation mechanisms. They studied two generally accepted formation models for HRE-GBDP in Nd-Fe-B sintered magnets. In the first model also called chemically induced liquid film migration, the HRE diffuses along the GB into the magnet as a part of the liquid GB phase above the eutectic point of the Nd-Fe-B system (~ 685 °C) [151]. The diffusion process is accompanied by the partial melting of the Nd-Fe-B matrix phase. Beginning with the cooling below the ternary eutectic temperature, the $(Nd,HRE)_2Fe_{14}B$ shells will start to precipitate out of the liquid phase and solidify on the surface of Nd-Fe-B matrix grains [125], [129], [151]–[154]. The result is the formation of core shells with a similar chemical composition. The second model is based on the solid-state diffusion of HRE along the GB. Löewe et al. [155] and Kim et al. [152] found that the diffusion process, in this case, is carried out below the ternary eutectic temperature. This theory is supported by the fact that toward the centre of the magnet, the Tb concentration in the GB phase significantly decreases. Moreover, the substitution of HRE for Nd in already formed $(Nd,HRE)_2Fe_{14}B$ shells becomes even harder, as they are less susceptible to the substitutional diffusion of Tb. The result is lower HRE concentration in GB and thinner shells as we go toward the centre of the sample [150].

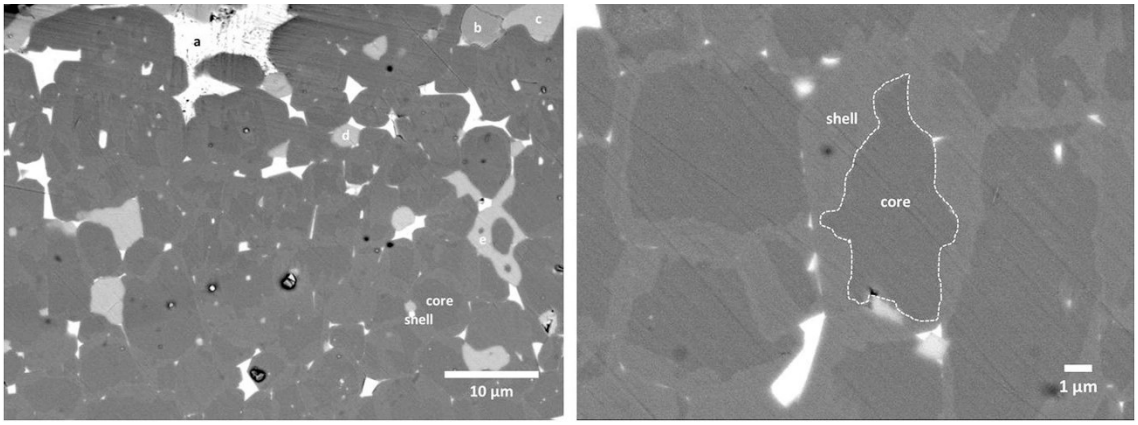

Figure 1.31: FEG-SEM image of core-shell-type microstructure of TbF_3 GBDP sintered Nd-Fe-B magnet [126].

In the end, the core of the Nd-Fe-B matrix grain preserves the original HRE-free chemical composition, meanwhile, the surface layer of the grain is enriched with HRE. The increasing magnetocrystalline anisotropy of the shell enhances the value of coercivity (Figure 1.32) and protects it against demagnetization. Moreover, the chemical composition of the core is still intact and possesses a high spontaneous magnetization of the $Nd_2Fe_{14}B$ matrix phase, which results in higher remanent magnetization and maximum energy product compared to HRE alloyed Nd-Fe-B magnet [127], [156], [157].

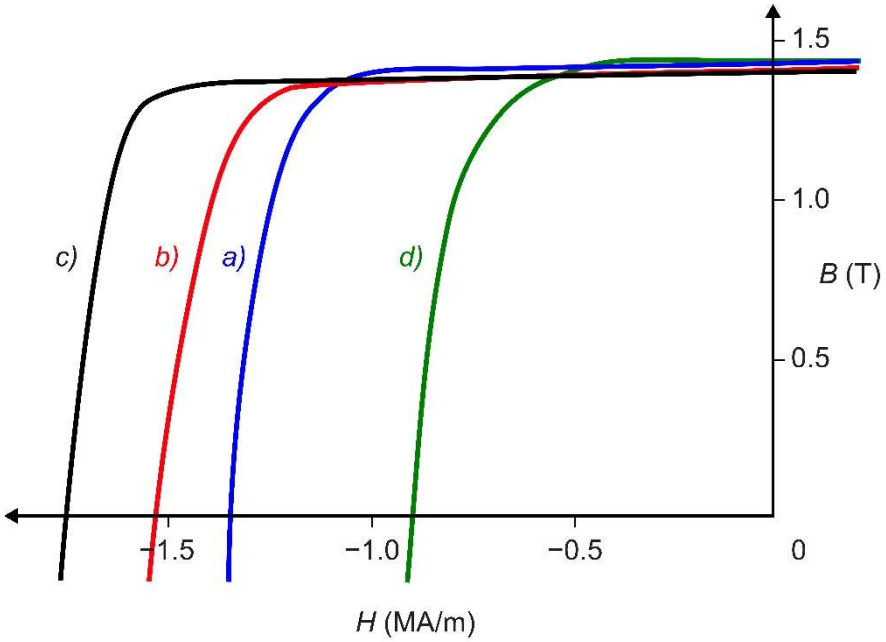

Figure 1.32: Demagnetization curves of Nd-Fe-B sintered magnets after annealing with a) Dy_2O_3, b) DyF_3, c) TbF_3 and d) without coating [128].

Besides the strong dependence of coercivity on the grain size of hot-deformed magnets, it is also known that the chemical composition of grain boundaries has a significant effect on this property [99], [106], [124]. Liu et al. presented a significant impact of Nd content in initial ribbons on the HD magnet's final coercivity [107]. The high Nd content increases the coercivity from 0.9 T to 1.79 T due to the formation of a thick Nd-rich grain-boundary phase and a decrease of the ferromagnetic nature in the intergranular phase, which

improves the magnetic isolation of the $Nd_2Fe_{14}B$ grains and enhances the pinning force against domain wall motion [107]. Another option to modify a HD magnet's grain-boundary composition from ferromagnetic to non-ferromagnetic nature is by low-temperature grain-boundary diffusion process using low-temperature eutectic alloys without heavy rare earths. The result of infiltration is the formation of the Nd-rich intergranular phase and consequently decoupling of $Nd_2Fe_{14}B$ grains, which is the main reason for the enhancement of coercivity of hot-deformed magnet [103]. Various eutectic alloys such as Nd_xR_y (M=Nd, R = Al, Cu, Mn, Zn, Ga) have already been investigated as diffusion sources for the infiltration process and the largest reported coercivity was limited to 2.5 T (Figure 1.33) [103], [158], [159]. However, an increase of the coercivity consequently decreases the remanent magnetization due to exchange coupling of Fe atoms with HRE atoms.

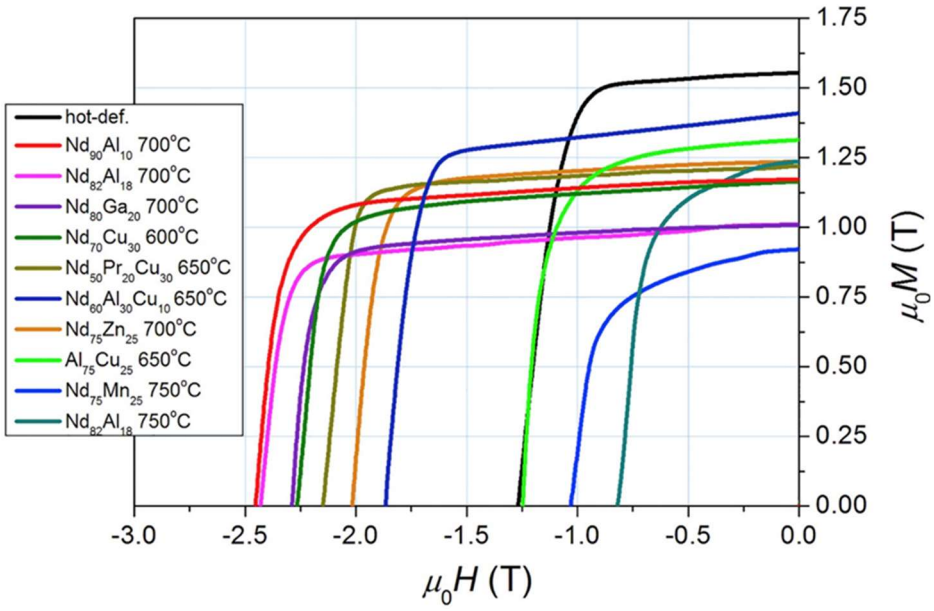

Figure 1.33: Demagnetization curves of hot-deformed (HD) magnet and grain boundary diffusion processed hot-deformed (HD) magnet with different low-temperature eutectic alloys [103].

To prevent a decrease of remanent magnetization and to further increase the coercivity, the HRE should be introduced as a diffusion source. As mentioned above, Hirosawa et al. used an HRE-GBDP method to enhance the coercivity of conventionally sintered magnets [36]. However, the temperatures used for the HRE-GBDP process of sintered magnets exceed 900 °C; therefore, they are not appropriate for HD magnets due to the excessive grain growth at high temperatures. That is why the grain-boundary diffusion process (GBDP) of the HD magnet should be introduced at lower temperatures. Sepehri-Amin et al. found a solution combining the elemental Dy with the Nd-Cu alloy resulting in $Nd_{60}Dy_{20}Cu_{20}$ alloy as diffusion source [160]. Later on, the same group used Tb instead of Dy in a composition $Nd_{60}Tb_{20}Cu_{20}$ [114]. Despite the significant increase of coercivity from 0.87 T to 2.57 T, they preserved the high remanent magnetization of 1.38 T for the hot-deformed magnet shown in Figure 1.34 [114].

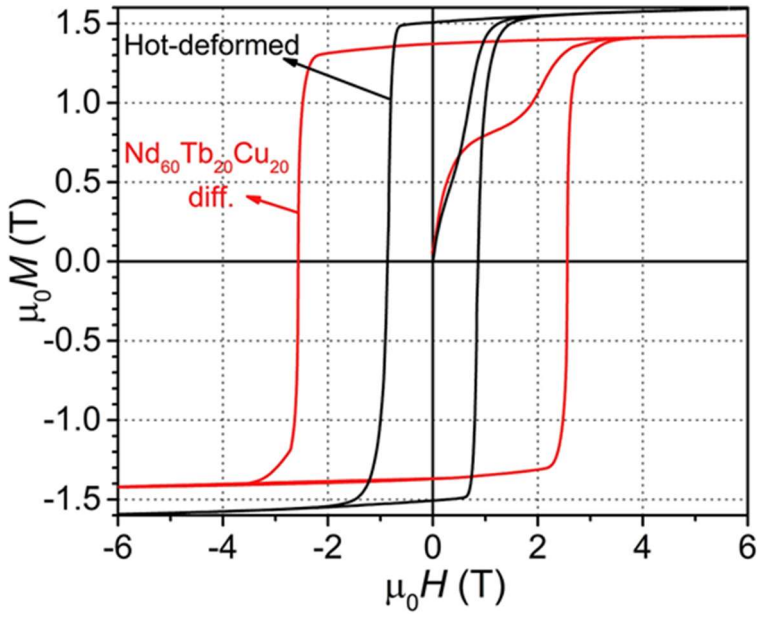

Figure 1.34: Hysteresis loops of the as hot-deformed(HD) and $Nd_{60}Tb_{20}Cu_{20}$ diffusion-processed hot-deformed (HD) Nd-Fe-B magnet [114].

However, the above-mentioned processed HD magnets were too thin for industrial applications. For such usage, the permanent magnet should have a thickness above 5 mm [161]. Recently, Tang et al. introduced a novel method, the so-called two-step eutectic grain-boundary diffusion process, where they treated a 5.6-mm thick hot-deformed magnet, and obtained a uniform microstructure from the surface to the centre of the processed HD magnet [161].

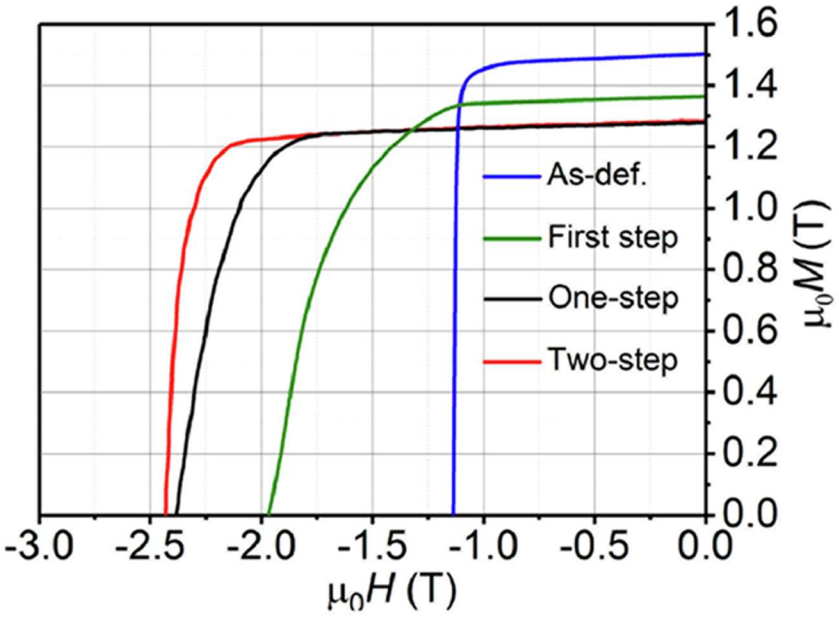

Figure 1.35: Demagnetization curves of the as hot-deformed, first step, one-step, and two-step diffusion processed hot-deformed (HD) Nd-Fe-B magnet [161].

A GBDP was performed in two different ways to show its efficiency. They showed that the one-step $Tb_{20}Dy_{10}Nd_{40}Cu_{30}$ diffusion-processed bulk hot-deformed magnet results in a large

coercivity enhancement from 0.91 T to 2.38 T and poor squareness of the demagnetization curve (Figure 1.35), which is a consequence of an inhomogeneous microstructure. On the other hand, they showed a solution with a two-step GBD process. In the first step, they used the $Tb_{20}Dy_{10}Nd_{40}Cu_{30}$ eutectic alloy, and in the second step, the $Nd_{80}Cu_{20}$ eutectic alloy as a diffusion source for the infiltration process [161]. Due to the uniform microstructure, they improved the demagnetization curve's squareness, enhanced the processed magnet's coercivity from 0.91 T to 2.43 T, and preserved the high remanent magnetization of 1.3 T (Figure 1.35) [161].

Chapter 2

Aims and Hypothesis

The main concept of my research arises from the fact that the demand for permanent magnets is growing exponentially as humanity tends to use green technology. Moreover, as we strive to preserve and maintain a sustainable environment, permanent magnets play a crucial role in many applications like electric vehicles and electric generators.

One branch of permanent magnets are Nd-Fe-B magnets, which possess the highest maximum energy product among the permanent magnets; however, there is still plenty of room for improvement of their magnetic properties. With this in mind, the primary goal of this thesis is to contribute to the enhancement of the magnetic properties of melt-spun Nd-Fe-B powders and Nd-Fe-B bulk magnets. To improve their coercivity, the usage of heavy rare-earths (HREs), such as Dy and Tb, are currently unavoidable in the fabrication of high-coercivity magnets. However, due to the limited natural abundance and high costs of HRE elements, an alternative route for the processing of HRE free/lean high-coercivity Nd-Fe-B magnets has emerged. One option is the grain-boundary diffusion process (GBDP) of Nd-Fe-B magnet or melt-spun powder with the addition of a heavy-rare-earth-free diffusion source [114]. In this case, the engineering of the grain boundary phase (GB) by low-temperature GBDP using low-temperature eutectic alloys such as $Nd_{70}Cu_{30}$ cause the formation of non-ferromagnetic GB phase which results in enhanced coercivity of the final Nd-Fe-B magnet and melt-spun powder [162]–[164]. Accordingly, the aim is the coercivity improvement for commercial low-cost melt-spun Nd-Fe-B for the purpose of processing the polymer-bonded magnets. Due to the low content of Nd-rich phase in the grain boundary, a $Nd_{70}Cu_{30}$ low-temperature eutectic alloy is introduced via GBDP to significantly improve the coercivity.

To enhance the coercivity even further, the HREs can be introduced only at the surface of the Nd-Fe-B grains, resulting in a local increase of magnetocrystalline anisotropy field at the nucleation sites [39], [114]. This HRE-GBDP method is commonly used for Nd-Fe-B sintered magnets [128], [130]. However, in the present work, a Nd-Fe-B hot-deformed (HD) magnet processed from the ultra-fine-grained melt-spun powder was employed, which is not suitable for conventional HRE-GBDP. Too high diffusion process temperatures (900 °C) cause substantial grain growth and consequently deteriorate the magnetic properties [136]. To prevent grain growth, a different approach should be considered. Instead of using conventional HRE-GBDP, the Dy or Tb should be included in low-temperature eutectic alloys [114]. Considering this, low-temperature $Nd_{62}Dy_{20}Al_{18}$, $Nd_{60}Tb_{20}Cu_{20}$ and $Nd_{60}Dy_{20}Cu_{20}$ eutectic alloys are used, which enable the formation of a HRE-shell at lower diffusion process temperatures without causing grain growth [114], [136], [160]. For industrial applications, the permanent magnet should have a thickness above 5 mm [161]. Recently, a novel method has been introduced, i.e., the so-called two-step eutectic GBDP, where a thick HD magnet is treated in a way to obtain a uniform microstructure of HD

magnet [161]. Besides a significantly enhanced coercivity, preserved high remanent magnetization, the squareness of the demagnetization curve is also improved, due to the uniform microstructure [161]. The aim of this work was a further optimization of the two-step grain-boundary diffusion process with a minimal amount of HRE elements in the final bulk hot-deformed Nd-Fe-B magnet.

Another, advanced option to ensure high-coercivity Nd-Fe-B magnets is so-called microstructural engineering. It is well known that the coercivity of Nd-Fe-B magnets is strongly connected to the grain size and the chemical composition of GBs [99], [106], [107], [124], [132]. An approach to enhance the coercivity of Nd-Fe-B magnets without the addition of heavy-rare-earth elements is to refine the grain size of the Nd-Fe-B matrix phase while enabling a continuous grain-boundary phase [37], [100], [132]–[134], [146], [165]. First attempts to decrease the grain size were performed in the processing of sintered Nd-Fe-B magnets. The grain size was reduced to 0.5 μm, however, the ultrafine starting powder is challenging for further use, due to its explosive nature [57], [132], [135]. As an alternative, a melt-spun Nd-Fe-B powder with an ultrafine grain size of ~ 250 nm suitable for processing of HD magnets was developed [19], [30]. Due to the ~ 150 μm particle size, which is significantly larger compared to jet-milled powders (1-10 μm) for sintered magnets, the Nd-rich phase is not subjected to oxidation during the HD process [107], [132]. The coercivity of HD magnets not only depends on the grain size but also on the chemical composition of the GB phase which ensures the magnetic isolation of the Nd-Fe-B matrix phase [99], [106], [116], [166]. To provide a small grain size and continuous grain GB phase in a HD Nd-Fe-B magnet, a closely monitored microstructure evolution should be considered as well as optimization of the processing parameters, which is also the goal of this work.

Chapter 3

Materials and Methods

3.1 Low-Temperature Eutectic Alloy ($Nd_{70}Cu_{30}$) Diffusion Processing of Commercial Melt-Spun Nd-Fe-B Powder for Polymer-Bonded Magnet

3.1.1 3.1.1 Preparation of $Nd_{70}Cu_{30}$ powder

A selected rare-earth element Nd (99.1 % purity) and selected metal Cu (99.9 % purity) were weighed in a desired atomic ratio (70:30). The elements were mixed and put in arc melter (Figure 3.1 (a)). Both elements were melted in an argon atmosphere to obtain a completely homogenized $Nd_{70}Cu_{30}$ alloy. The as-prepared alloy was placed into the crucible and then into a melt-spinning device (Figure 3.1 (b)) for processing the $Nd_{70}Cu_{30}$ ribbons. When the 10^{-5} mbar vacuum was established in the chamber, the argon was released to achieve the 0.7 bar in the chamber and 0.2 bar overpressure in the pre-chamber. After reaching the desired atmosphere, the alloy in the crucible, was induction heated above the melting point of the alloy ($\sim$ 520 °C [167]). When the alloy was completely melted, the overpressure was released from the pre-chamber into the crucible, which caused the dissolved alloy to flow through the nozzle in the form of a thin jet onto the rotating water-cooled copper wheel. The water-cooled copper wheel rotated at a speed of 2400 revolutions per minute. This resulted in ultra-fast cooling ($< 10^6$ K/s) of the molten alloy, which in contact with the copper wheel instantly changed from a liquid to a solid-state, forming long and thin ribbons. The ribbons were subsequently ground in a laboratory grinder in an argon atmosphere to produce the $Nd_{70}Cu_{30}$ powder with a particle size between 0.1 and 0.3 mm.

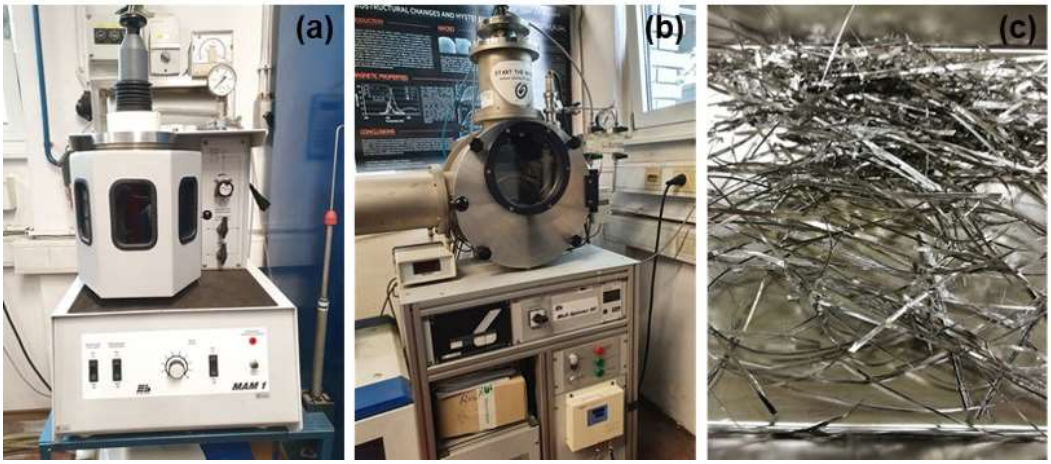

Figure 3.1: (a) Arc Melter MAM-1 – Edmund Bühler, (b) Melt Spinner SC – Edmund Büchler, and (c) melt-spun Nd-Cu ribbons.

3.1.2 Diffusion processing of commercial melt-spun Nd-Fe-B powder

Figure 3.3 shows the schematic procedure of diffusion processed melt-spun Nd-Fe-B ribbons. The pre-prepared $Nd_{70}Cu_{30}$ powder (3–7.5 wt.%) was added to the commercial melt-spun Nd-Fe-B ribbons with composition $Nd_{26.4}Fe_{67.6}Co_{5.0}B_{1.0}$ (wt.%) and 1.5–2.5 vol.% of intergranular phase. After the addition of the $Nd_{70}Cu_{30}$ alloy, the sample was mixed under the argon atmosphere in a homogenizer to obtain a homogenized mixture. This was followed by compression of the homogenized mixture in a press to obtain a 10-mm green tablet.

Figure 3.2: Carbolite furnace with vacuum system.

The as-prepared tablets were placed in a quartz tube attached to a vacuum system (10^{-4} - 10^{-5} mbar) and heat-treated in a carbolite furnace (Figure 3.2). The samples were then heat-treated at different temperature regimes (600 – 700 °C) and for different dwelling times (15 min – 120 min). During the heat treatment, the alloy diffused into Nd-Fe-B

ribbons, which resulted in a final sample composed of agglomerates. To change the agglomerates back to individual particles, the heat-treated tablets were homogenized in an argon atmosphere. As-prepared diffusion processed melt-spun Nd-Fe-B ribbons were subsequently used for the production of a polymer-bonded magnet.

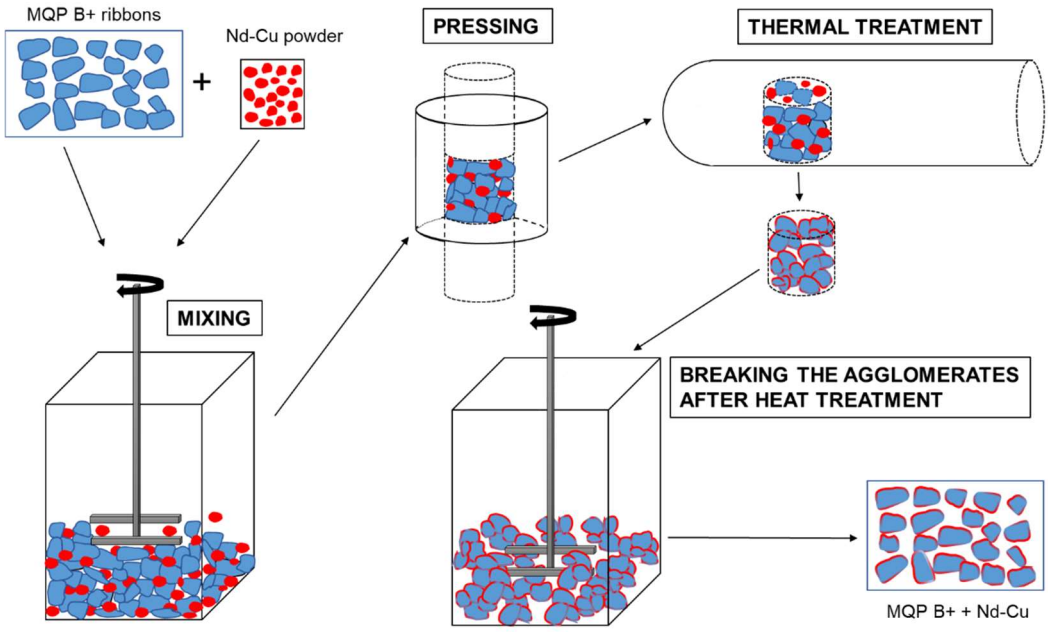

Figure 3.3: Schematic presentation of the processing of the improved commercial melt-spun Nd-Fe-B ribbons with the addition of Nd-Cu [168].

3.1.3 Processing of polymer-bonded magnet from diffusion-processed melt-spun Nd-Fe-B powder

The Nd-Fe-B polymer-bonded magnets were processed in a laboratory and in an industrial plant. To prepare the polymer-bonded magnet, a polymer binder is mixed with melt-spun Nd-Fe-B powder. In this work, a 12 wt.% of polyphenyl sulfide (PPS) binder was added to the melt-spun Nd-Fe-B ribbons.

Figure 3.4 shows a schematic process for processing of the polymer-bonded magnet in the laboratory. The procedure started with homogenizing the melt-spun Nd-Fe-B magnetic ribbons and polymer in the homogenizer. This was followed by compression of the homogenized mixture in a press, to obtain a 10-mm green tablet. The as-prepared tablets were placed in a quartz tube attached to a vacuum system. Before the heat treatment, a vacuum between 10^{-4} mbar and 10^{-5} mbar was established. The tablets were then heat-treated at 300 °C for 40 min. After the heat treatment was completed, the polymer-bonded magnet was cooled together with the oven to room temperature.

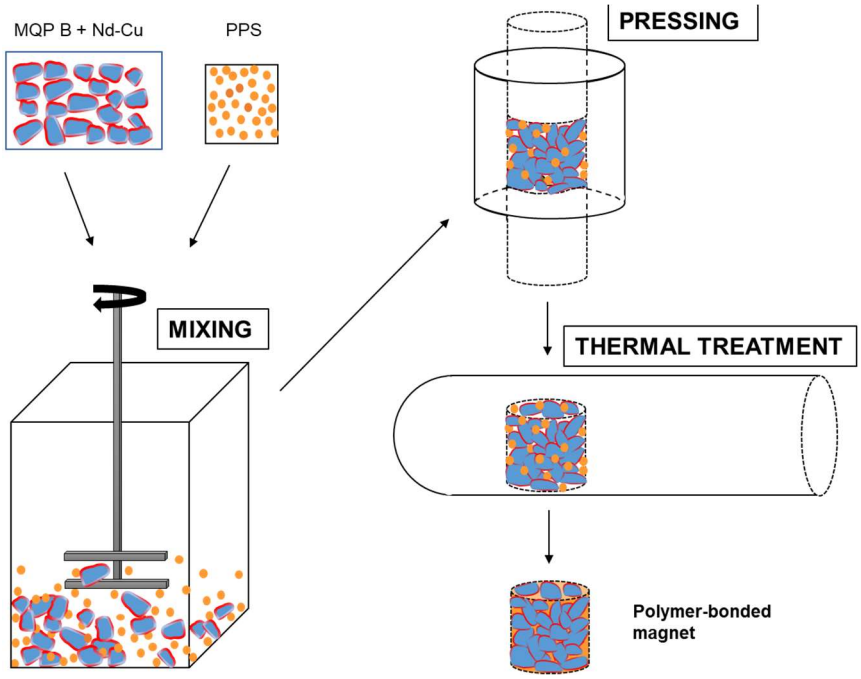

Figure 3.4: Schematic presentation of manufacturing a polymer-bonded magnet by laboratory procedure [168].

The industrial processing of the polymer-bonded magnet is shown in Figure 3.5. It started with homogenizing the mixture of melt-spun Nd-Fe-B ribbons and polymer in an extruder (Leistritz ZSE 27 HP 36D) at ≈ 300 °C to obtain 5-mm pellets with the desired composition. In the next step, the pellets were dosed into the injection-moulding device (Krauss-Maffei KM 30) at ≈ 300 °C to obtain polymer-bonded magnets with a cylindrical shape and a 10-mm diameter.

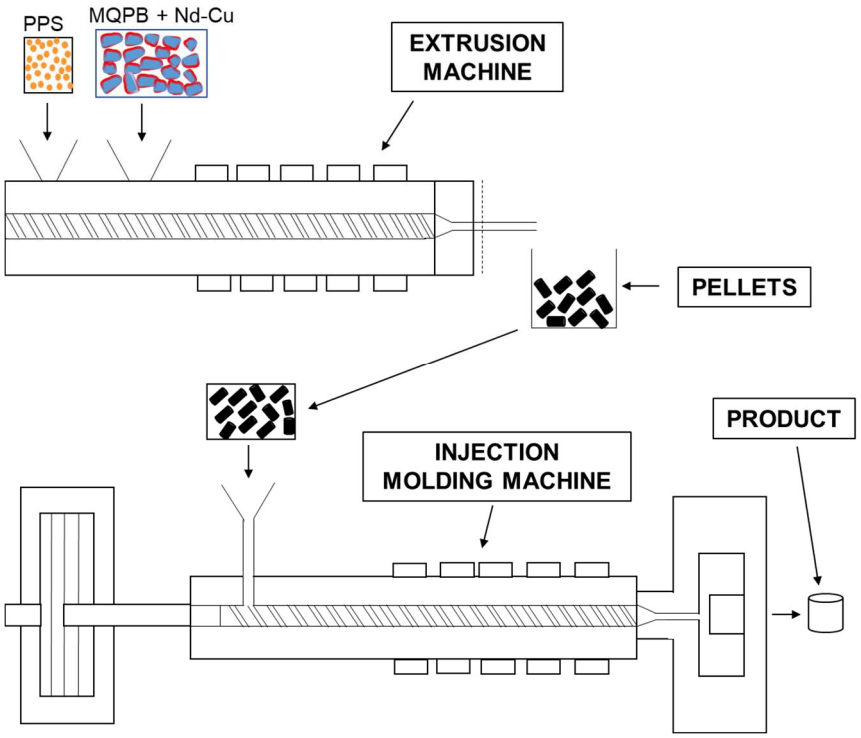

Figure 3.5: Schematic presentation of the manufacturing process of polymer-bonded magnets according to the industrial process (Kolektor KHF) [168].

3.2 Hot-Pressing and Hot-Deformation Process

The processing of hot-pressed (HP) and hot-deformed (HD) magnets from commercial melt-spun Nd-Fe-B ribbons was performed with a spark plasma sintering (SPS) furnace (Fuji Electronic Industrial Dr Sinter SPS Syntex 3000) shown in Figure 3.6.

Figure 3.6: Pressure-assisted pulsed current sintering (SPS) system Fuji Electronic Industrial.

Commercial Nd-Fe-B melt-spun ribbons (Figure 3.7 (a)) with the nominal composition $Nd_{30.1}Pr_{0.4}Fe_{62.0}Co_{6.1}Ga_{0.5}B_{0.9}$ (wt.%) were used for the HD process. The powder was first HP into a fully dense magnet using a spark plasma sintering (SPS) furnace.

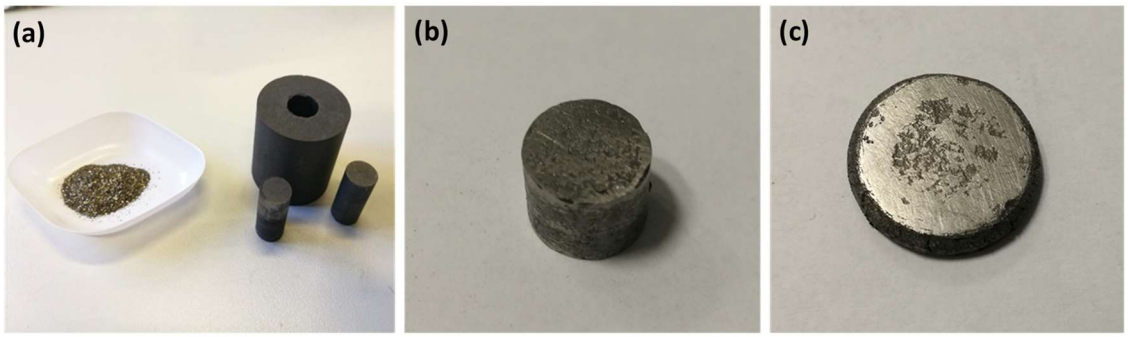

Figure 3.7: Procedure for preparation of Nd-Fe-B HD magnet from (a) Nd-Fe-B melt-spun ribbons, to (b) HP magnet and final product (c) HD magnet.

The SPS experiment was performed in a 10-mm graphite mould. To provide good electrical contact and prevent damaging the graphite tools, a thin graphite foil (≈200 μm) was placed between the sample, mould and punches. The magnet was compacted at an SPS temperature 675 °C under a uniaxially applied pressure of 50 MPa in a vacuum (≈ 5×10^{-2} mbar). The temperature and pressure regimes are shown in Figure 3.8. The SPS temperature was controlled by a K-type thermocouple inserted into the graphite mould at the level of the sample. The thickness of the graphite wall splitting the thermocouple from the sample was minimal (≈1 mm). A 12:2 on-off direct current (DC) pulse sequence was applied to heat the sample. After the sintering process was finished, the pressure was immediately released and the mould with the sample was cooled to RT by cooling water circulating through the system.

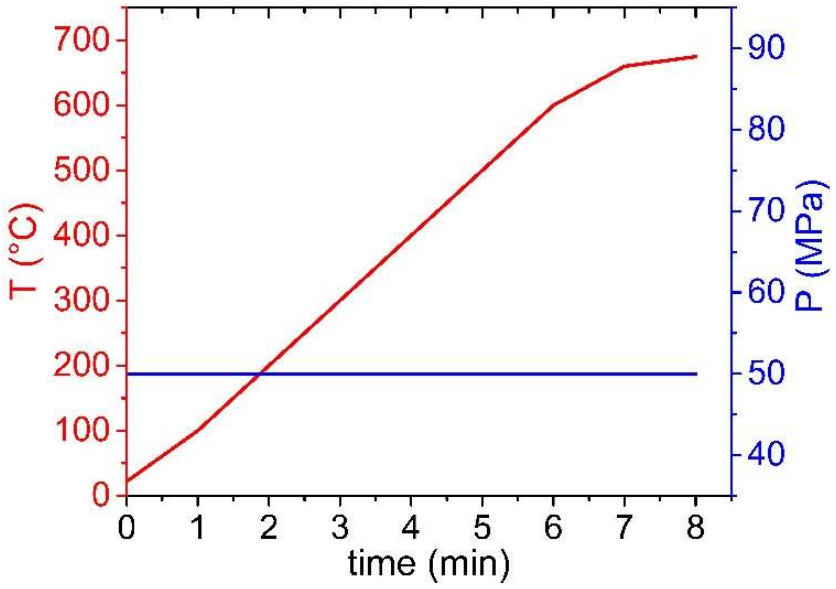

Figure 3.8: Temperature and pressure regimes of HP magnet with nominal target temperature of 675 °C and maximum pressure of 50 MPa.

The HP magnets (Figure 3.7 (b)) were polished to remove the graphite foil and subsequently HD (Figure 3.7 (c)) in a 20-mm graphite mould. A thin graphite foil was also placed between the sample, mould and punches. The marked temperatures in Figure 3.9 and Figure 3.10 are the nominal temperatures and serve as an SPS processing parameter. The SPS settings and measurement were equal to the HP process described above.

In this work, several different approaches of processing HD Nd-Fe-B magnets have been proposed:

In the first approach, the alternative method, the SPS technique, has been used to perform a hot-deformation process at the temperature and pressure similar to that used in the conventional hot-pressing technique. The heating rate from RT to 600 °C was 75 °Cmin^{-1}, followed by a lower heating rate of 60 °Cmin^{-1} and 20 °Cmin^{-1} in the next to 2 minutes to 680 °C. In the last minute, the temperature was maintained at the target temperature of 680 °C, and the maximum pressure of 90 MPa was applied during this holding time. The temperature and pressure regimes are shown in Figure 3.9.

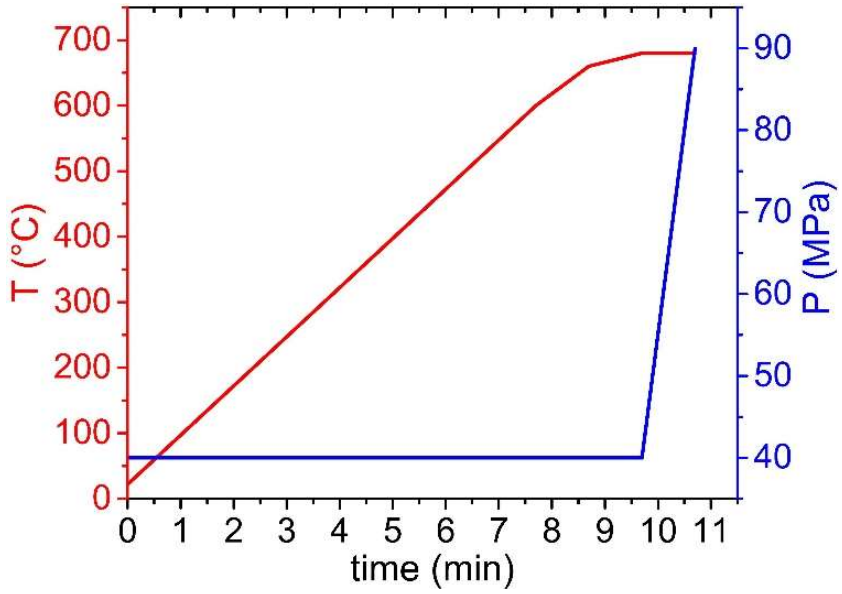

Figure 3.9: Temperature and pressure regimes of HD magnet with nominal target temperature of 680 °C and maximum pressure of 90 MPa.

In the second case, the SPS technique was used to produce a low-energy-processing HD magnet, with the aim of reducing the energy consumption during the processing. The heating rate from RT to nominal temperature of 300 °C was 100 °Cmin^{-1}, followed by a lower heating rate of 30 °Cmin^{-1} and 20 °Cmin^{-1} in the next to 2 minutes to 350 °C. In the last minute, the temperature was maintained at the target temperature of 350 °C. The higher pressure was initially applied at a nominal temperature of 250 °C, and within 3.5 minutes, it constantly increased to a maximum pressure of 90 MPa. After the target temperature was reached, the sintering process was immediately stopped, and pressure released. The temperature and pressure regimes are shown in Figure 3.10.

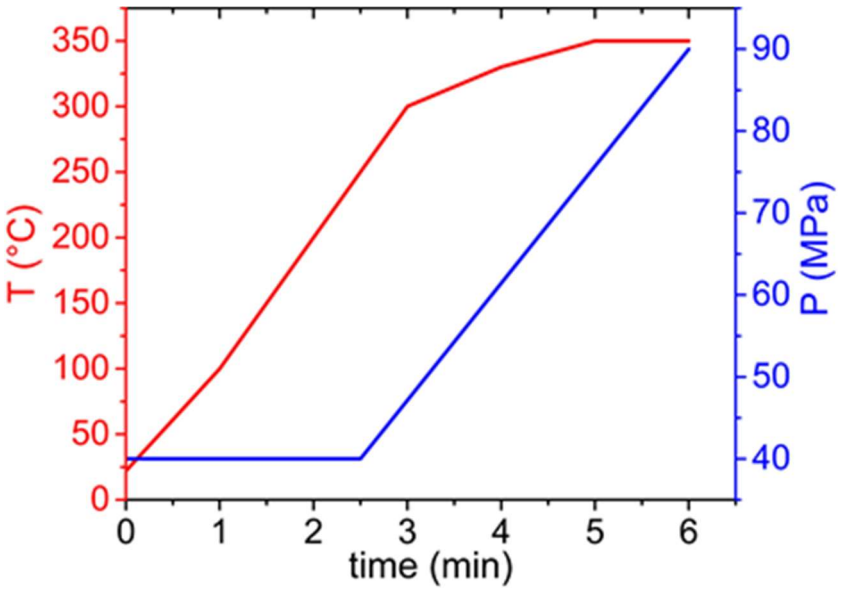

Figure 3.10: Temperature and pressure regimes of HD magnet with nominal target temperature of 350 °C and maximum pressure of 90 MPa.

The last approach to perform a deformation process was to produce the anisotropic bulk magnet by low-pressure SPS. The HP magnet was hot-deformed under a constant low-pressure of 40 MPa with a heating rate of 100 °C/min, and the target temperature was set to 680 °C. The temperature and pressure regime are shown in Figure 3.11. In this case, the HD magnets with different deformation ratios were prepared to understand the dependence of the remanent magnetization on the deformation ratio. The hot-deformation process was stopped at different stages, based on the height reduction, at 1 mm, 2 mm, 3 mm, etc.

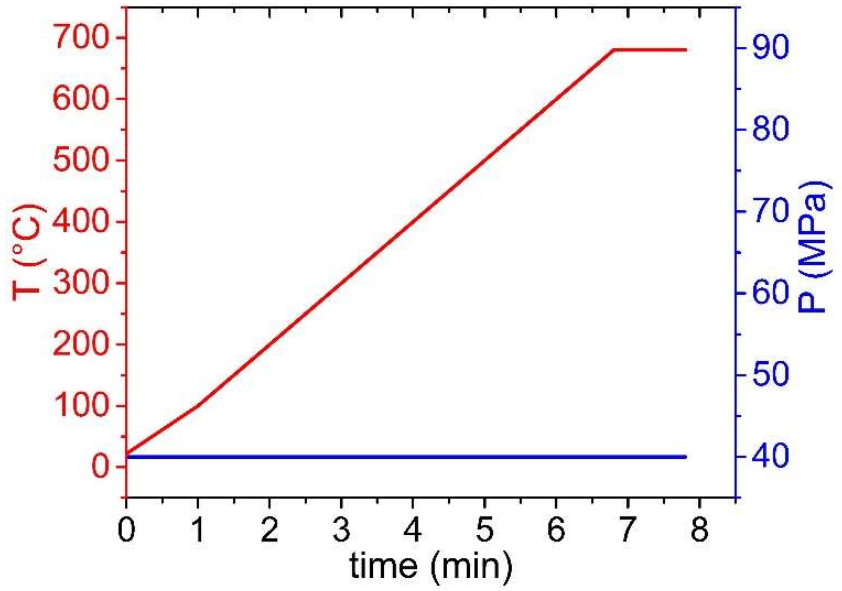

Figure 3.11: Temperature and pressure regimes of HD magnet with nominal target temperature of 350 °C and maximum pressure of 40 MPa.

The deformation ratio (%) of the HD magnet was calculated based on the following definition (Eq. (3.1)):

$$DR = \frac{h_{HP} - h_{HD}}{h_{HP}} * 100\% \tag{3.1}$$

where DR represents the deformation ratio (%) and h_{HP}, h_{HD} are the heights of the HP, HD magnet (mm). After each HD process, the HD magnet was polished to remove the graphite foil.

3.3 Sample Preparation for Microstructure Characterization and Magnetic Measurements

The edges of the HD magnets were firstly cut to provide a well-shaped sample. The samples were cut into square blocks to provide a regular shape for an accurate measurement of the magnetic properties. The cutting operations were performed on a precision sectioning saw with a BUEHLER IsoMet Low Speed Saw diamond blade.

Figure 3.12: Precision sectioning saw with a diamond blade – BUEHLER IsoMet Low Speed Saw.

For a further SEM microstructural characterization, the cut samples were placed into the resin for easier grinding and polishing. The grinding and polishing were performed on a metallographic specimen preparation device – Struers LaboPol (Figure 3.13). The grade of the polishing paper started with 800 and continued with 1000, 1200, 2400 and 4000. After each grade change, the sample was cleaned in an ultrasonic bath to provide clean surfaces before further polishing with a higher grade of polishing paper. The final polishing was performed with a one-, half- and quarter-micrometre carbon-based slurry.

Figure 3.13: Metallographic specimen preparation device - Struers LaboPol.

After polishing, the surface was chemically etched with 3 M Cyphos solution for 10 s and then intensively washed with ethanol. The as-prepared sample was cleaned and dried with hot air, before sticking it on the aluminium holder for the SEM characterization. For better conductivity, an adhesive carbon conductive tape was put between the holder and the sample. If necessary, the sample was coated with the carbon layer to prevent charging.

For TEM bulk sample investigations, the sample was prepared via conventional preparation technique: cut into square blocks of 1.8 x 1.8 mm, perpendicular and parallel to the pressing direction. The blocks were fitted into 3-mm brass cylinders using epoxy glue to improve strength. The TEM specimen was ground to a thickness of 100 μm and dimpled down to 15 μm at the disc centre (Dimple grinder, Gatan Inc., Warrendale PA, USA) (Figure 3.14 (a)). To reach the electron transparent region, the TEM specimens were finally ion-milled (PIPS, Precision Ion Polishing System, Gatan Inc., USA) (Figure 3.14 (b)) using 3-kV Ar^+ ions at an incidence angle of 8° until perforation.

Figure 3.14: (a) Dimple grinder – model 656 and (b) Precision Ion Polishing System (PIPS) – Gatan.

3.4 Characterization

3.4.1 Magnetic properties measurements

The magnetic properties of the (diffusion processed) melt-spun Nd-Fe-B powder, polymer-bonded, HP and HD magnets were measured using a Steingroever EP2 permeameter (Figure 3.15 (b)) and a Lakeshore 7304 vibrating-sample magnetometer (VSM) (Figure 3.15 (a)). Before measuring the magnetic properties, all the samples were fully magnetized in 5-T magnetic pulser.

During the magnetic measurements many influences should be considered, that is why the estimation of the uncertainty of the magnetic measurements is a complex task. However, according to the provider of magnetic-measurement devices, in both above-mentioned devices, the uncertainty of magnetic measurements is less than 2 % if there is no saturation effect of the pole-piece.

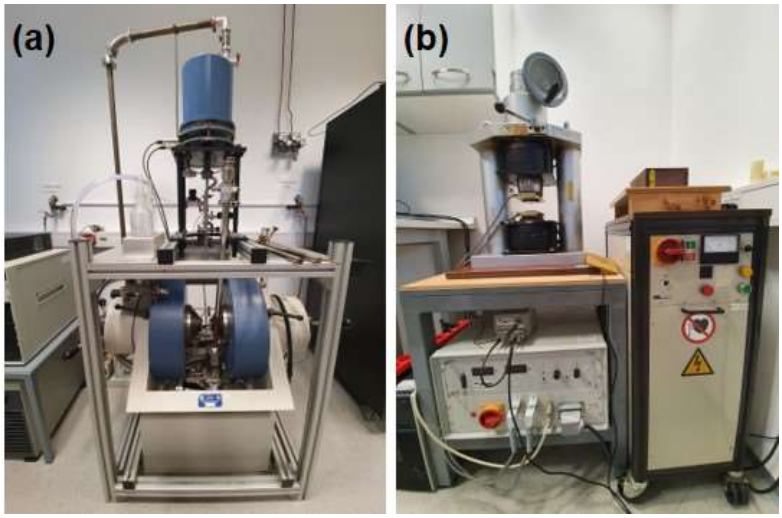

Figure 3.15: (a) Vibrating-sample magnetometer – Lakeshore 7304 and (b) Permeameter – Steingroever EP2.

3.4.2 XRD

The X-ray powder diffraction data of the processed samples were collected with a Malvern Panalytical Empyrean X-ray diffractometer (XRD) (Figure 3.16) using monochromated X-rays, produced by a Cu-target tube (0.15406 nm). The scan range in Bragg angles was from 10° to 90° (2θ) and the final XRD data were analysed with HighScore Plus XRD Analysis Software.

Figure 3.16: X-ray diffractometer - Malvern Panalytical Empyrean.

3.4.3 SEM and TEM analysis

The microstructural characterization and compositional analyses were performed using a field-emission gun scanning electron microscope FEG-SEM JEOL JSM-7600F (Figure 3.17 (a)), field-emission gun scanning electron microscope (FEG-SEM) Thermo Fisher, Verios G4 HP (Figure 3.17 (b)) and a focused-ion-beam scanning electron microscope (FIB-SEM) FEI HeliosNanolab 650. The phases present in the samples were revealed by backscattered electron imaging (BSE), while the local chemical composition was analysed by energy-dispersive X-ray spectroscopy (EDS).

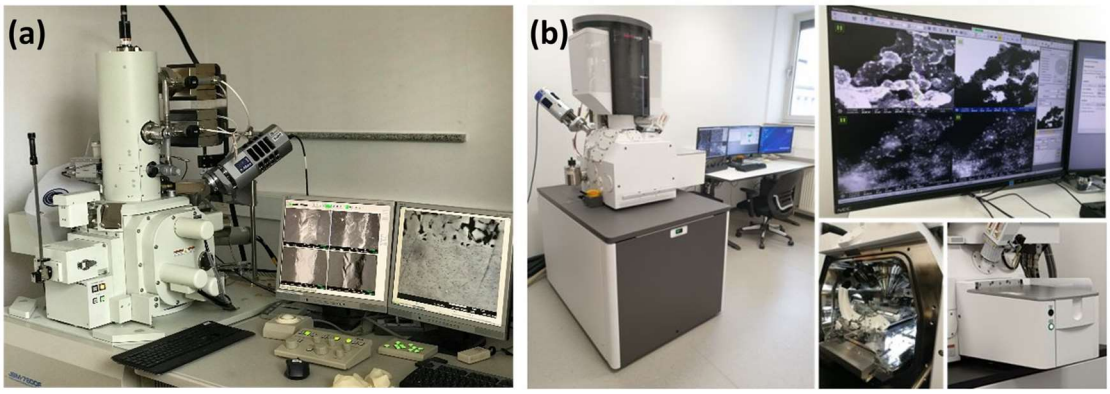

Figure 3.17: Scanning electron microscopes: (a) field-emission-gun scanning electron microscope FEG-SEM JEOL JSM-7600F and (b) field-emission-gun scanning electron microscope (FEG-SEM) Thermo Fisher, Verios G4 HP.

The scanning electron microscope (SEM) scans a focused beam of high-energy electrons at the surface of the sample to generate a variety of signals (image). The obtained signals reveal information about the texture (morphology), chemical composition and crystal structure [169], [170].

Detailed microstructural investigations of the samples were performed by transmission electron microscopy (TEM) using a 200-kV microscope (TEM; JEM-2100, Jeol, Japan, Figure 3.18).

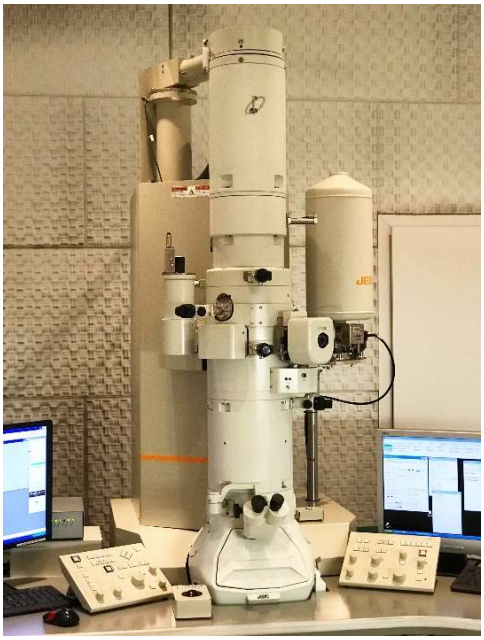

Figure 3.18: Transmission electron microscope (TEM) – Jeol JEM-2100.

Chapter 4

Results and Discussion

The Results and Discussion part of the thesis is divided into four different topics that comprise two first-author papers, a first author patent application, a last-author paper and additional experimental results. The first section of the Results and Discussion includes the first-author paper entitled “Magnetic properties and microstructure evolution of hot-deformed Nd-Fe-B magnets produced by low-pressure spark-plasma sintering”. The second topic summarizes the results of an economically efficient method for processing HD Nd-Fe-B magnets based on SPS. In the third part, a second first-author paper entitled “Significant coercivity enhancement of hot-deformed Nd-Fe-B bulk magnets by two-step diffusion process using a minimal amount of Dy” is presented. This paper was performed in collaboration with National Institute for Materials (NIMS, Japan) and Daido Company (Japan). The last section of this chapter includes the first-author patent application entitled “A process for improving the magnetic properties of commercial Nd-Fe-B magnetic ribbons with a small proportion of intergranular phase and a process for producing polymer-bonded magnets from these melt-spun ribbons”, which was developed in collaboration with Kolektor KFH d.o.o and Kolektor Group d.o.o. Besides the patent application, the last-author paper performed by Soderžnik et al. is also included in the last part of the Results and Discussion.

4.1 Paper "Magnetic Properties and Microstructure Evolution of Hot-Deformed Nd-Fe-B Magnets Produced by Low-Pressure Spark-Plasma Sintering"

The following section presents a paper entitled "Magnetic properties and microstructure evolution of hot-deformed Nd-Fe-B magnets produced by low-pressure spark-plasma sintering", authored by M. Korent, M. Komelj, S. Šturm, K. Žužek Rožman, K. Žagar Soderžnik and M. Soderžnik, which was published in Journal of Magnetism and Magnetic Materials, vol. 515, in 2020, p. 167279, (https://doi.org/10.1016/j.jmmm.2020.167279).

In this work, the HD Nd-Fe-B magnets from commercial MQUF Nd-Fe-B ribbons were produced. The SPS technique was used as it enables the implementation of a deformation process at the relatively low temperature of 680 °C and a low pressure of 40 MPa compared to conventional processes [171], [172]. At this temperature and pressure, a high deformation ratio of 75 % is reached, which results in good remanent magnetization of 1.29 T, a coercivity of 1077 kA/m and a maximum energy product of 313 kJ/m^3. Even though a HD magnet is processed at low pressure and short processing time, the accomplished magnetic properties are comparable with HD magnets obtained by applying high pressure and temperature [171], [173].

The initial stages of the HD process were investigated by means of microstructural observations and magnetic measurements. HD magnets with different deformation ratios (23 %, 34 %, and 46 %) were produced and their remanence dependence on the deformation ratios was investigated. In the initial stages of the HD process, the cone-like shape of the magnet is observed for the first time. In such a cone-like HD magnet, with 23 % deformation ratio, a detailed microstructure characterization was performed. The investigation at different regions of a cone-like HD magnet showed various degree of alignment of both the ribbons and the grains were detected.

The experimental data were interpreted in the frame of the Stoner-Wohlfarth model, which reproduces the hysteresis response to an external magnetic field. The model reproduced the experimental data reasonably well and revealed good magnetic properties while applying low pressure, if a phenomenological decrease in the anisotropy constant is taken into account.

The subject of this manuscript will draw the attention of a wide scientific community since high-coercivity heavy-rare-earth-free Nd-Fe-B hot-deformed magnets are timely and extensively studied in the field of functional materials and materials synthesis. In addition, high coercivity permanent magnets are key materials in the production of electric components on the macro and nanoscales.

Journal of Magnetism and Magnetic Materials 515 (2020) 167279

Contents lists available at ScienceDirect

Journal of Magnetism and Magnetic Materials

journal homepage: www.elsevier.com/locate/jmmm

Research articles

Magnetic properties and microstructure evolution of hot-deformed Nd-Fe-B magnets produced by low-pressure spark-plasma sintering

Matic Korent[a,b], Matej Komelj[a], Sašo Šturm[a,b], Kristina Žužek Rožman[a,b], Spomenka Kobe[a,b], Kristina Žagar Soderžnik[a], Marko Soderžnik[a,c,*]

[a] Jožef Stefan Institute, Department for Nanostructured Materials, Ljubljana, Slovenia
[b] Jožef Stefan International Postgraduate School, Ljubljana, Slovenia
[c] Laboratory for Tribology and Interface Nanotechnology (TINT), Faculty for Mechanical Engineering, University of Ljubljana, Slovenia

ARTICLE INFO

Keywords:
Low-pressure hot-deformation process
Spark-plasma sintering
Microstructure evolution
Stoner–Wohlfarth model

ABSTRACT

We have produced hot-deformed Nd-Fe-B magnets from commercial (MQU-F) Nd-Fe-B ribbons. The spark-plasma-sintering technique was used to deform the samples under low pressures of 40 MPa. The initial stages of the hot-deformation process were investigated in terms of microstructures and magnetic properties. Hot-deformed magnets with different deformation ratios were produced and the dependence of the remanence on the deformation ratio was determined. In the initial stages of the hot-deformation process, a cone-like shape of the magnet was observed for the first time. The experimental data can be qualitatively interpreted by applying the basic Stoner–Wohlfarth model.

1. Introduction

Nd-Fe-B permanent magnets, discovered in 1983 [1,2], are used in demanding applications such as wind turbines and hybrid electric vehicles [3,4]. Sintered Nd-Fe-B magnets are the most common form used in such applications; however, their typical intrinsic coercivity ($\mu_0 H_{cJ}$) of 955 kA/m and high remanent magnetization ($\mu_0 M_r$) of 1.4 T are often insufficient [5,6]. Besides, their performance drops significantly with increasing temperature, as illustrated by a temperature coefficient of coercivity $\beta \approx -0.6\%\ ^\circ C^{-1}$, which consequently restricts their use at the elevated temperatures (150–200 °C) typical of electric motors [7,8].

To overcome these limitations, another type of Nd-Fe-B permanent magnet can be used. Hot-deformed (HD) Nd-Fe-B magnets have a lower temperature coefficient $\beta \approx -0.45\%\ ^\circ C^{-1}$ than sintered magnets, due to the smaller local demagnetization factor of the finer grains, which makes these magnets more applicable at high temperatures [7–9]. In addition, a high maximum energy product, $(BH)_{max}$, of more than 400 kJ/m^3 [10–12] makes them ideal in the most demanding conditions [11,13].

Since the HD process involves elevated temperatures, grain-boundary migration and the sliding of planes lead to plastic deformation of the magnet [14]. The final microstructure, as a consequence of this plastic deformation, results in a crystallographic alignment of the $Nd_2Fe_{14}B$ grains along the pressing direction [15]. This means that the morphologically isotropic $Nd_2Fe_{14}B$ grains in the melt-spun ribbons are transformed into textured, closely packed, plate-like grains with the crystallographic *c*-axis parallel to the pressing direction [16,17]. This textured microstructure of $Nd_2Fe_{14}B$ grains is crucial for achieving a remanent magnetization that is close to the maximum theoretical values [18]. Recently, Tang et al. reported an extremely high degree of grain alignment, which resulted in a remanent magnetization of 1.45 T [19]. This value is slightly lower than the maximum theoretical value for the saturation magnetization of the $Nd_2Fe_{14}B$ phase (1.60 T) [20]. The main reason for the deviation from the maximum theoretical value of the remanent magnetization are the zones with coarse, misaligned grains [19].

From the perspective of the coercivity, a homogeneous distribution of the intergranular Nd-rich phases plays an important role in reducing the exchange coupling between the grains [21]. During magnetization reversal, such a distribution works as a barrier to domain-wall motion and, consequently, contributes to a coercivity enhancement [16,17]. However, a detailed microstructural characterisation revealed that the Nd-rich intergranular phases contains up to 50 at.% of Fe and Co in the form of pure metals [21]. Due to the presence of ferromagnetic elements, the intergranular phase is ferromagnetic [7]. Consequently, the $Nd_2Fe_{14}B$ grains are exchange coupled, and so the coercivity does not exceed 1430 kA/m [7,22]. The results of recent observations using Lorenz microscopy by U.M.R Seelam et al. [23] suggested that the

* Corresponding author.
E-mail address: marko.soderznik@tint.fs.uni-lj.si (M. Soderžnik).

https://doi.org/10.1016/j.jmmm.2020.167279
Received 17 March 2020; Received in revised form 23 July 2020; Accepted 29 July 2020
Available online 02 August 2020
0304-8853/

domain walls are strongly pinned to the intergranular Nd-rich phase, and they run continuously from grain to grain [17].

Typically, high pressures are used to achieve a high deformation ratio and, consequently, a well-oriented texture, resulting in a high remanent magnetization. The deformation ratio (%) is defined as $DR = \frac{h_{HP} - h_{HD}}{h_{HP}} * 100\%$, where DR stands for the deformation ratio (%), h_{HP} for the height of the HP magnet (mm) and h_{HD} for the height of the HD magnet (mm). On the other hand, due to the high pressure during the deformation process, the Nd-rich intergranular liquid phase is partially squeezed out, which leads to a thinning of the grain-boundary phase around the $Nd_2Fe_{14}B$ grains. Any deficit of the intergranular phase has a detrimental effect on the coercivity due to the strong exchange coupling of the ferromagnetic grains [21,24].

To avoid squeezing out the Nd-rich phase, low pressures should be used in the HD process. The spark-plasma-sintering (SPS) technique enables the production of HD magnets at low pressures (< 40 MPa) [25]. Furthermore, the main advantage of SPS, as we have applied it for this study, is that the grain growth is inhibited by the low sintering temperatures and the short holding times [17,26,27].

The low-pressure SPS in our study was inspired by Sagawa's pressless sintering (PLP) [28]. The SPS technique was used to produce fully dense HD Nd-Fe-B magnets at low pressures. For this work, the very first stages of the microstructure evolution of the HD magnets were monitored. Anisotropic magnets with different deformation ratios were produced, while the results of the microstructural analyses and magnetic characterisation, particularly the influence of the grain reorientation, were complemented by a simple Stoner–Wohlfarth (SW) model.

2. Experiment and model

Commercial Nd-Fe-B melt-spun ribbons (MQU-F) with the nominal composition $Nd_{30.1}Pr_{0.4}Fe_{62.0}Co_{5.1}Ga_{0.5}B_{0.9}$ (wt. %) were used. The ribbons were compacted in a vacuum into a hot-pressed (HP), fully dense magnet at 675 °C and 50 MPa using a SPS furnace (Fuji Electronic Industrial Dr. Sinter SPS Syntex 3000). A 10-mm mould was used for the preparation of the HP magnet. After HP, the dimensions were measured and the density was determined using a bulk-density measurement system (Densitec, Exelia AG, Switzerland). The HP magnets were then hot-deformed in a 20-mm mould under a constant pressure of 40 MPa with a heating rate of 100 °C/min, and the temperature was set to 680 °C. To understand the HD process and its microstructural evolution, HD magnets with different deformation ratios were prepared. The HD process was stopped at different stages, based on the height reduction, at 1 mm, 2 mm, 3 mm, etc. The magnetic properties of the partially HD magnets were measured with a permeameter (Steingroever EP2) at room temperature. For the microstructure analyses, samples were cut perpendicular to the c-axis and metallographically polished. The microstructure was investigated at the micro and nano levels using a FIB Helios Nanolab™ 650.

To be able to interpret the experimental results, we applied the simplest SW model, which reproduces the hysteresis response to an external magnetic field. The approach is not meant as a complete theoretical description of a complex interplay between microstructure and measurable magnetic properties, while rather as an intuitive interpretation of the observed phenomenon. The model is based on the magnetic contribution to the energy consisting of two phenomenological terms. The first term, which describes the coupling between the magnetic moment m and the external magnetic field H, is a minimum if the two vectors are parallel to each other. The second term is the contribution of the magnetic anisotropy, implying the angle ϑ between the direction of the magnetic moment and the easy axis should be as small as possible. The anisotropy constant K is assumed to describe both the intrinsic effects, for example, the magnetocrystalline anisotropy, and the influence of extrinsic factors, for example, the role of grain boundaries. For simplicity we considered a magnet consisting of a set of non-interacting domains characterized by different easy-axis directions. Furthermore, we assumed that all the domains exhibit the same magnitude m of the magnetic moment. The direction of the magnetic moment m for each domain is found by minimizing the expression:

$$E_{mag}^{i} = (m.\ H)\cos(\varphi_i) + Ksin^2(\varphi_i - \vartheta_i) \quad (1)$$

where H is the magnitude of the external field, while φ_i and ϑ_i are the angles between the magnetic moment and the directions of the external field and the easy axis, respectively. The measured quantity is usually a projection of the magnetization in the direction of the external field, which can be modelled as the sum over all the domains:

$$M = m \sum_i \cos(\varphi_i) \quad (2)$$

It is clear that the effect of the microstructure can be modelled by varying the anisotropy constant K and the distribution of the angles ϑ_i. We apply the former completely phenomenological to simulate the non-desired effect of the pressure on the grain boundaries, in agreement with both main interpretations [29,30] of Brown's paradox, by regarding the microstructural defects as the source of a strong deviation between the intrinsic anisotropy field and the measured coercivity. On the other hand, the distribution of the angles ϑ_i realistically mimics the alignment of the grains in the microstructure: a narrow (broad) distribution implies more anisotropic (isotropic) grain orientations, which is the central object of our investigation.

3. Results

3.1. Initial stages of the HD process

The fully dense, cylindrical HP magnet in Fig. 1(a) serves as a reference, and such a HP magnet was the subject of the HD process. Fig. 1(b-f) presents plastically deformed magnets with different deformation ratios, starting with 23% (2 mm), 34% (3 mm), 46% (4 mm), 57% (5 mm) and ending with the highest degree of deformation, i.e., 75% (6.6 mm). During the initial stages of the HD process, with height reductions of 2, 3, and 4 mm, the magnets took on the shape of a cone, and then in the final stages (5 and 6.6 mm height reduction) the magnets recover the shape of a cylinder.

3.2. Microstructure evolution

Fig. 1 shows the progress of the HD process with SPS and its effect on the shape and the microstructure. Before the deformation process, a HP magnet with an isotropic microstructure and the shape of a cylinder with a 10-mm diameter was produced (see Fig. 1a). In the first stages of the HD process, the magnet took on the shape of a cone, which must be a consequence of the SPS pressing system, as it will be discussed later. During the final stage of the process, the HD magnet had the shape of a cylinder with a diameter of approximately 20 mm and a fully anisotropic microstructure, which is presented on the micro and nano levels in Fig. 2.

The magnet with the shape of a cone and a height reduction of 2 mm indicated in Fig. 1. (b) was divided into three zones (upper, middle, and bottom of the magnet). The microstructures of all three zones were investigated using backscattered (BS) electrons in the FIB–SEM. Fig. 2(a), (c), and (e) present microstructures at the micro level, which means that the ribbons can be seen in the upper, middle and bottom zones of the HD magnet. It is clear that in the upper zone, see Fig. 2(a), the ribbons are randomly orientated, in the middle zone, see Fig. 2(c), the ribbons exhibit a partial orientation, while in the lower zone, see Fig. 2(e), the majority of the ribbons are oriented perpendicular to the pressing direction. Fig. 2(b), (d), (f) show microstructures on the nanoscale, i.e., the grains inside the ribbons in the upper, middle and

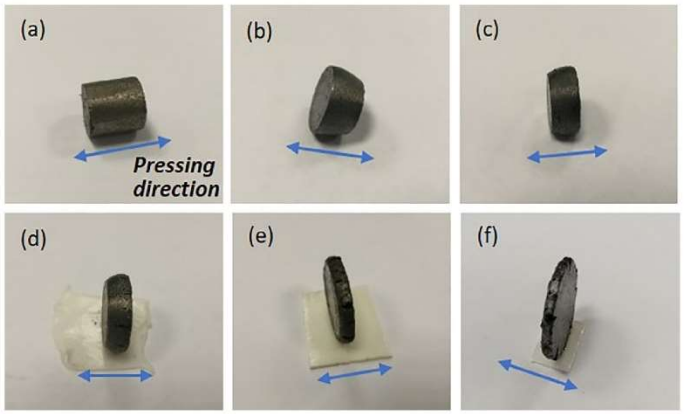

Fig. 1. (a) Hot-pressed Nd-Fe-B magnet, partially HD Nd-Fe-B magnet with height reductions of (b) 2 mm, (c) 3 mm, (d) 4 mm, (e) 5 mm, and the fully HD magnet with a height reduction of (f) 6.6 mm.

lower zones of the HD magnet. The effect of the ribbon alignment is also very similar to the grain alignment. In the upper zone, see Fig. 2(b), randomly distributed ribbons with plate-like grains were observed. In the middle zone, see Fig. 2(d), the grains within the ribbons showed partial orientation. Compared to the upper zone, a better orientation is observed in the middle zone. However, plenty of grains remain randomly orientated. In the bottom zone, see Fig. 2(f), the grains within the ribbons show a pronounced orientation that is perpendicular to the pressing direction.

3.3. Magnetic properties

Fig. 3 shows the demagnetization curves of the HP and HD magnets with different deformation ratios. The magnetic properties are collected in Table 1. The HP magnet has the lowest remanent magnetization of 0.83 T and the highest coercivity of 1556 kA/m. The medium remanent magnetization is the reason for the moderate maximum energy product of 117 kJ/m^3. With hot deformation, the texturing becomes more pronounced, which leads to an increment in the remanent magnetization. A relatively small height reduction of 2 mm already led to a 31%

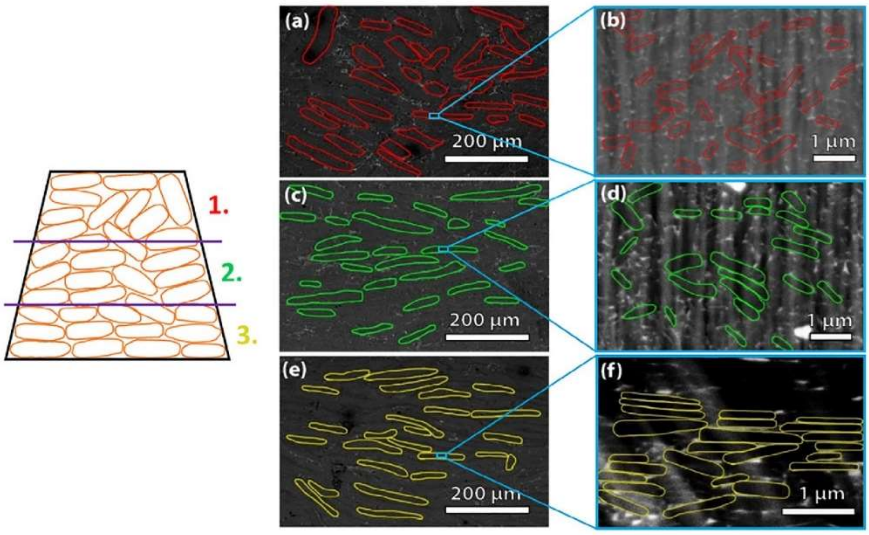

Fig. 2. Backscattered-SEM images of HD magnet with a height reduction of 2 mm of (a) ribbons in upper part of the magnet, (b) grains inside ribbons in upper part of the magnet, (c) ribbons in middle part of the magnet, (d) grains inside ribbons in middle part of the magnet, (e) ribbons in bottom part of the magnet, (f) grains inside ribbons in bottom part of the magnet.

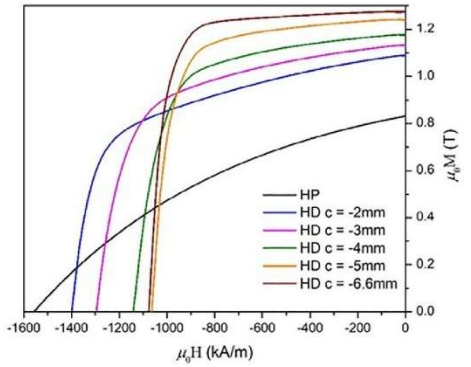

Fig. 3. Demagnetization curves of HP magnet and HD magnets with different height reductions (2, 3, 4, 5 and 6.6 mm).

Table 1
Magnetic properties (coercivity, remanent magnetization, maximum energy product) of HP magnet and HD magnets with different height reductions.

	HP magnet	HD magnets				
Height reduction (mm)	/	−2	−3	−4	−5	−6.6
Deformation ratio (%)	/	23	34	46	57	75
$\mu_0 H_{cJ}$ (kA/m)	1556	1400	1296	1142	1071	1077
$\mu_0 M_r$ (T)	0.83	1.09	1.13	1.18	1.24	1.29
$(BH)_{max}$ (kJ/m^3)	117	209	231	255	290	313

increase in the remanent magnetization and a 10% decrease in the coercivity compared to the HP magnet. By increasing the deformation ratio, the remanent magnetization is gradually increased to 1.29 T. On the other hand, the coercivity decreases with an increasing remanent magnetization from 1556 kA/m to 1077 kA/m.

3.4. Stoner–Wohlfarth model

The degree of grain alignment was modelled by introducing a Gaussian distribution of the angle ϑ_i for particular isolated, single-domain grains in the SW model, for different values of the variance σ parameter. The calculated total magnetization, see Eq. (2), divided by the number of grains and the coercivity approached convergence when applying at least 1000 single-domain grains. The equilibrium angle was found by minimizing Eq. (2) for each of the domains. The narrower c-axis distribution of the grains (higher σ), simultaneously with the phenomenologically decreased anisotropy constant, K, yields a higher remanent magnetization and a lower coercivity.

We suppose that with the pressure, simultaneously with a better alignment of the grains, we also introduce defects in the microstructure. These defects act as pinning sites, which consequently decrease the coercivity loss due to the external demagnetization fields. This phenomenon was modelled by slightly decreasing the anisotropy constant K, which resulted in a qualitative agreement between the modelled, see Fig. 4 (second quadrant), and experimental, see Fig. 3, results.

4. Discussion

We have shown that a HD magnet can be produced at relatively low temperature (680 °C) and low pressure (40 MPa) compared to conventional processes, for example, Y. I. Lee et al. [31] produced a Nd-Fe-B HD magnet at 810 °C and 100 MPa, and Y. H. Hou et al. [32] used 750 °C and 350 MPa. The HD magnets were prepared from commercial

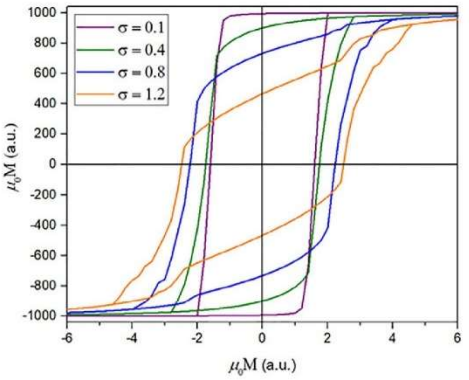

Fig. 4. Simulated hysteresis loops of HD magnets with different deformation ratios based on a Gaussian distribution (σ denotes the standard deviation of the Gaussian distribution of the grain-orientation angles ϑ_i).

MQU-F ribbons by applying minimal pressure during the SPS. The results of our experiments demonstrate that high pressures, which are typically used in HD [33,34], are not required for the production of HD magnets. We applied a pressure of 40 MPa during the deformation process and a temperature of 680 °C, which was enough to achieve a high deformation ratio of 75%. The SPS method enables short processing times, which means that the grain growth is limited [25]. Using low-pressure SPS we produced a HD magnet with a coercivity of 1077 kA/m, a remanent magnetization of 1.29 T and a maximum energy product of 313 kJ/m^3. These magnetic properties are comparable with current HD magnets obtained by applying a high pressure and a high temperature [31,35]. As mentioned before, the high pressure is most likely the reason for squeezing out the Nd-rich intergranular phase, which leads to a stronger intergranular exchange coupling and a lower coercivity [8,36]. To prevent squeezing out the Nd–rich intergranular phase, using a moderate temperature was proposed by J. Liu et al. [8]. However, we combined both, moderate temperature and low pressure, to make a more uniform, non-ferromagnetic intergranular phase around the $Nd_2Fe_{14}B$ grains.

Partially HD samples with a height reduction (deformation ratio) of 2 (23%), 3 (34%), and 4 mm (46%) took on a cone-like shape, which is the result of the conditions during the compression mode in the SPS machine, where the magnet is pressed only by the bottom cylinder piston, while the top cylinder piston is fixed. Such a cone-like magnet, shown schematically in Fig. 5., with a deformation ratio of 23% was characterized in terms of microstructure. The FIB BS electron figures show the gradual texturing from the top towards the bottom of the sample. In the upper zone, randomly distributed ribbons consist of grains with no orientation of the c-axis along the pressing direction. In the middle zone the grains within the ribbons are partially orientated. Despite there being better texturing than in the upper zone, there are still a lot of randomly oriented grains, which lowers the degree of texture and decreases the remanent magnetization [17]. In the bottom zone of the magnet, the orientation of the ribbons and the grains within the ribbons becomes strongly pronounced, which leads to a high degree of deformation [37].

It was demonstrated that the simplest SW model, defined by the energy contribution $E_{mag}^{\perp} = mHcos(\varphi_i) + Ksin^2(\varphi_i - \vartheta_i)$ [38] of a particular single-domain grain could qualitatively reproduce the measured hysteresis loops if the pressure-induced formation of grain-surface defects is phenomenologically assumed. The FIB BS electron images showed that at low pressure, a rather large amount of the intergranular

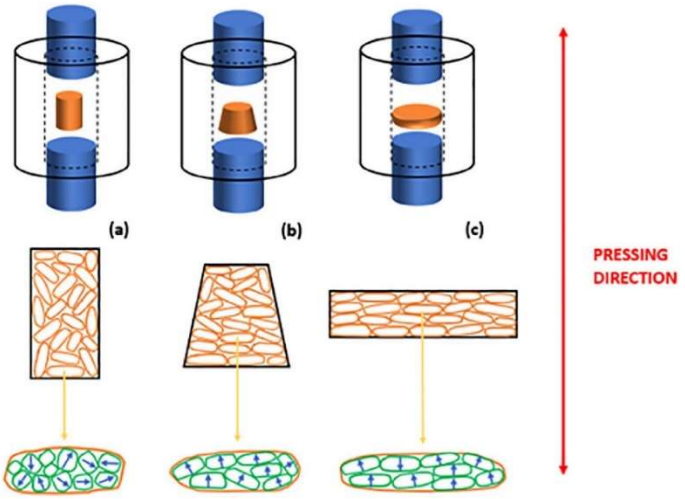

Fig. 5. Schematic figures of (a) HP, (b) partially HD and (c) fully HD magnet at the micro and nano levels.

phase was detected in all three zones. However, much larger grains were found in the well-aligned regions. This means that the higher demagnetizing field in the larger grains is the critical microstructural factor with respect to the lower coercivity [36,39]. In the Refs. [36,39], the authors found that large misaligned grains act as initiator of the magnetization reversal process and therefore affect the coercivity. In the SW model a negative impact of the increasing applied pressure was phenomenologically taken into account by reducing the anisotropy constant K in order to obtain a decrease of the coercivity, simultaneously with an increase in the remanent magnetization, as seen from the measurements.

We showed an alternative way of producing a competitive-quality HD magnet using low-pressure SPS, in analogy with PLP. Using a low pressure during the process means that massive, heavy presses can be eliminated from the production line [40]. This also implies that low pressure is an essential factor that must be considered during the HD. However, to further improve this process and understand its impact on the magnetic properties, additional research is needed, since the influence of electric currents on the deformation during SPS was not considered here.

5. Conclusions

We suggested a HD process for commercial Nd-Fe-B ribbons under low pressure at 40 MPa using the SPS technique. A magnet with a deformation ratio of 75% was produced at 680 °C and showed a remanent magnetization of 1.29 T and a coercivity of 1077 kA/m. The magnetic properties are comparable with existing HD methods, where a high pressure and a high temperature are needed. In addition, we produced HD magnets with different deformation ratios (23, 34, 46, 57, and 75%) and tracked the behaviour of the microstructure in the initial stages of the process. The microstructural investigation showed three different zones in a cone-like HD magnet. It revealed different degrees of texturing in each zone. The magnetic properties of HD magnets with different height reductions showed a decrease of coercivity and an increase of the remanent magnetization with an elevated deformation ratio. The interplay between the positive effect of the HD process due to the grain alignment and the spurious negative impact due to the grain-boundary deterioration was interpreted in the frame of a simple SW model. It reproduces the experimental data reasonably well if a phenomenological decrease in the anisotropy constant is taken into account.

CRediT authorship contribution statement

Matic Korent: Conceptualization, Writing - original draft. **Matej Komelj:** Writing - review & editing. **Sašo Šturm:** Funding acquisition. **Kristina Žužek Rožman:** . **Spomenka Kobe:** . **Kristina Žagar Soderžnik:** . **Marko Soderžnik:** Conceptualization, Writing - review & editing, Supervision.

Declaration of Competing Interest

The authors declare that they have no known competing financial interests or personal relationships that could have appeared to influence the work reported in this paper.

Acknowledgements

This work was supported by projects ID PR-08336, P2-0084, L2-9213 of the Slovenian Research Agency. CENN Nanocenter Slovenia is also acknowledged for using FIB FEI HeliosNanoLab 650.

References

[1] M. Sagawa, K. Hiraga, H. Yamamoto, Y. Matsuura, Permanent magnet materials based on the rare earth-iron-boron tetragonal compounds (invited), IEEE Trans. Magn. 20 (5) (1984) 1584–1589, https://doi.org/10.1109/TMAG.1984.1063214.
[2] A.S. Kim, F.E. Camp, High performance NdFeB magnets (invited), J. Appl. Phys. 79 (8) (1996) 5035, https://doi.org/10.1063/1.361566.
[3] M. Soderžnik, M. Korent, K. Žagar Soderžnik, M. Katter, K. Üstüner, S. Kobe, High-coercivity Nd-Fe-B magnets obtained with the electrophoretic deposition of submicron TbF3 followed by the grain-boundary diffusion process, Acta Mater. 115 (2016) 278–284, https://doi.org/10.1016/j.actamat.2016.06.003.
[4] H. Sepehri-Amin, T. Ohkubo, K. Hono, The mechanism of coercivity enhancement by the grain boundary diffusion process of Nd-Fe-B sintered magnets, Acta Mater. 61 (6) (2013) 1982–1990, https://doi.org/10.1016/j.actamat.2012.12.018.
[5] X. Tang, H. Sepehri-Amin, T. Ohkubo, K. Hioki, A. Hattori, K. Hono, Coercivities of hot-deformed magnets processed from amorphous and nanocrystalline precursors,

Acta Mater. 123 (2017) 1–10, https://doi.org/10.1016/j.actamat.2016.10.026.
[6] H. Sepehri-Amin, Y. Une, T. Ohkubo, K. Hono, M. Sagawa, Microstructure of fine-grained Nd-Fe-B sintered magnets with high coercivity, Scr. Mater. 65 (5) (2011) 396–399, https://doi.org/10.1016/j.scriptamat.2011.05.006.
[7] H. Sepehri-Amin, et al., Microstructure and temperature dependent of coercivity of hot-deformed Nd-Fe-B magnets diffusion processed with Pr-Cu alloy, Acta Mater. 99 (2015) 297–306, https://doi.org/10.1016/j.actamat.2015.08.013.
[8] J. Liu, et al., Grain size dependence of coercivity of hot-deformed Nd-Fe-B anisotropic magnets, Acta Mater. 82 (2015) 336–343, https://doi.org/10.1016/j.actamat.2014.09.021.
[9] H. Sepehri-Amin, T. Ohkubo, M. Gruber, T. Schrefl, K. Hono, Micromagnetic simulations on the grain size dependence of coercivity in anisotropic Nd-Fe-B sintered magnets, Scr. Mater. 89 (2014) 29–32, https://doi.org/10.1016/j.scriptamat.2014.06.020.
[10] Y. Hou, D.J. Sellmyer, Magnetic Nanomaterials: Fundamentals Synthesis and Applications, Wiley-VCH Verlag GmbH, 2017.
[11] T. Zhang, et al., Hot-deformed Nd-Fe-B magnets fabricated by dynamic loading with a high maximum energy product, Intermetallics 73 (2016) 67–71, https://doi.org/10.1016/j.intermet.2016.04.001.
[12] T. Saito, M. Fujita, T. Kuji, K. Fukuoka, Y. Syono, The development of high performance Nd-Fe-Co-Ga-B die upset magnets, J. Appl. Phys. 83 (11) (1998) 6390–6392, https://doi.org/10.1063/1.367522.
[13] S. Sawatzki, et al., Anisotropic local hardening in hot-deformed Nd-Fe-B permanent magnets, Acta Mater. 147 (2018) 176–183, https://doi.org/10.1016/j.actamat.2017.12.059.
[14] R.K. Mishra, E.G. Brewer, R.W. Lee, Grain growth and alignment in hot deformed Nd-Fe-B magnets, J. Appl. Phys. 63 (8) (1988) 3528–3530, https://doi.org/10.1063/1.340731.
[15] Z. Hu, H. Qu, J. Zhao, C. Luo, J. Li, Y. Liu, Enhanced mechanical properties in die-upset Nd-Fe-B magnets via die-upsetting process, J. Rare Earths 30 (11) (2012) 1112–1115, https://doi.org/10.1016/S1002-0721(12)60189-6.
[16] J. Liu, H. Sepehri-Amin, T. Ohkubo, K. Hioki, A. Hattori, K. Hono, Microstructure evolution of hot-deformed Nd-Fe-B anisotropic magnets, J. Appl. Phys. 115 (17) (2014) 15–18, https://doi.org/10.1063/1.4867960.
[17] Y.H. Hou, Y.L. Huang, Z.W. Liu, D.C. Zeng, S.C. Ma, Z.C. Zhong, Hot deformed anisotropic nanocrystalline NdFeB based magnets prepared from spark plasma sintered melt spun powders, Mater. Sci. Eng. B Solid-State Mater. Adv. Technol. 178 (15) (2013) 990–997, https://doi.org/10.1016/j.mseb.2013.06.009.
[18] Z. Wang, et al., Magnetic properties improvement of die-upset Nd-Fe-B magnets by Dy-Cu press injection and subsequent heat treatment, Sci. Rep. 6 (November) (2016) 1–12, https://doi.org/10.1038/srep38335.
[19] X. Tang, H. Sepehri-Amin, T. Ohkubo, K. Hono, Suppression of non-oriented grains in Nd-Fe-B hot-deformed magnets by Nb doping, Scr. Mater. 147 (2018) 108–113, https://doi.org/10.1016/j.scriptamat.2017.12.032.
[20] S. Hirosawa, Y. Matsuura, H. Yamamoto, S. Fujimura, M. Sagawa, H. Yamauchi, Magnetization and magnetic anisotropy of R2Fe14B measured on single crystals, J. Appl. Phys. 59 (3) (1986) 873–879, https://doi.org/10.1063/1.336611.
[21] J. Liu, et al., Effect of Nd content on the microstructure and coercivity of hot-deformed Nd-Fe-B permanent magnets, Acta Mater. 61 (14) (2013) 5387–5399, https://doi.org/10.1016/j.actamat.2013.05.027.
[22] J. Li, et al., Coercivity and its thermal stability of Nd–Fe–B hot-deformed magnets enhanced by the eutectic grain boundary diffusion process, Acta Mater. 161 (2018) 171–181, https://doi.org/10.1016/j.actamat.2018.09.018.
[23] U.M.R. Seelam, et al., Coercivity of the Nd-Fe-B hot-deformed magnets diffusion-processed with low melting temperature glass forming alloys, J. Magn. Magn. Mater. 412 (2016) 234–242, https://doi.org/10.1016/j.jmmm.2016.04.005.
[24] X.D. Xu, et al., Comparison of coercivity and squareness in hot-deformed and sintered magnets produced from a Nd-Fe-B-Cu-Ga alloy, Scr. Mater. 160 (2019) 9–14, https://doi.org/10.1016/j.scriptamat.2018.09.028.
[25] G. Jingkun, L. Jang, H. Kou, Modern Inorganic Synthetic Chemistry, 1st ed., Elsevier, 2011, pp. 429–454.
[26] X. Song, et al., Technique for preparing ultrafine nanocrystalline bulk material of pure rare-earth metals, Adv. Mater. 18 (9) (2006) 1210–1215, https://doi.org/10.1002/adma.200502619.
[27] X.Q. Li, L. Li, K. Hu, Z.C. Chen, S.G. Qu, C. Yang, Microstructure and magnetic properties of anisotropic Nd-Fe-B magnets prepared by spark plasma sintering and hot deformation, Trans. Nonferrous Met. Soc. China (English Ed.) 24 (10) (2014) 3142–3151, https://doi.org/10.1016/S1003-6326(14)63453-1.
[28] M. Sagawa, Toward ultimate Nd-Fe-B permanent magnets, Rare-earth Permanent Magnets and Their Applications, 2012, p. 3.
[29] H. Kronmüller, Theory of nucleation fields in inhomogeneous ferromagnets, Phys. Status Solidi 144 (1) (1987) 385–396, https://doi.org/10.1002/pssb.2221440134.
[30] D. Givord, P. Tenaud, T. Viadieu, Coercivity mechanisms in ferrite and rare earth transition metal sintered magnets (SmCo5, Nd-Fe-B), IEEE Trans. Magn. 24 (2) (1988) 1921–1923, https://doi.org/10.1109/20.11646.
[31] Y.I. Lee, G.Y. Huang, C.W. Shih, W.C. Chang, H.W. Chang, J.S. You, Coercivity enhancement in hot deformed Nd2Fe14B-type magnets by doping low-melting RCu alloys (R = Nd, Dy, Nd + Dy), J. Magn. Magn. Mater. 439 (2017) 1–5, https://doi.org/10.1016/j.jmmm.2017.05.009.
[32] Y.H. Hou, et al., Effects of Nd-rich phase on the improved properties and recoil loops for hot deformed Nd-Fe-B magnets, Acta Mater. 115 (2016) 385–391, https://doi.org/10.1016/j.actamat.2016.06.015.
[33] F. Hou, et al., Evolution of microstructures and magnetic properties in bulk Nd-Fe-Cu-B nanocomposites prepared by high pressure thermal deformation, J. Magn. Magn. Mater. 499 (November 2019) (2020) 166271, https://doi.org/10.1016/j.jmmm.2019.166271.
[34] T. Saito, Y. Sajima, D. Nishio-Hamane, Enhancement of magnetic properties by Zn addition in Nd-Fe-B hot-deformed magnets produced by spark plasma sintering method, J. Alloys Compd. 687 (2016) 662–666, https://doi.org/10.1016/j.jallcom.2016.06.151.
[35] Q. Liu, et al., Coercivity optimization of hot-deformed Nd-Fe-B magnets by addition of B19.23Fe80.77 particles, J. Magn. Magn. Mater. 498 (June 2019) (2020) 166254, https://doi.org/10.1016/j.jmmm.2019.166254.
[36] M. Soderžnik, et al., Magnetization reversal process of anisotropic hot-deformed magnets observed by magneto-optical Kerr effect microscopy, J. Alloys Compd. 771 (2019) 51–59, https://doi.org/10.1016/j.jallcom.2018.08.231.
[37] M. Zhu, W. Li, Texture formation mechanism and constitutive equation for anisotropic thermorheological rare-earth permanent magnets, AIP Adv. 7 (5) (2017), https://doi.org/10.1063/1.4978700.
[38] M.F. de Campos, F.A.S. da Silva, J.A. de Castro, Relation between initial magnetization curve and grain size of nanocrystalline NdFeb magnets, Mater. Sci. Forum 802 (December) (2014) 558–562, https://doi.org/10.4028/www.scientific.net/MSF.802.558.
[39] M. Soderžnik, B. Ambrožič, K. Žagar Soderžnik, M. Korent, Limits of grain boundary engineering in nanocrystalline Nd-Fe-B melt-spun ribbons, Mater. Lett. 264 (2020) 20–22, https://doi.org/10.1016/j.matlet.2020.127338.
[40] W.F. Li, T. Ohkubo, K. Hono, M. Sagawa, The origin of coercivity decrease in fine grained Nd-Fe-B sintered magnets, J. Magn. Magn. Mater. 321 (8) (2009) 1100–1105, https://doi.org/10.1016/j.jmmm.2008.10.032.

4.2 Paper "Toward Low-Energy Spark-Plasma Sintering of Hot-Deformed Nd-Fe-B Magnets"

In this section, a newly developed, economically efficient method for processing rare-earth magnets based on SPS is presented throughout the paper entitled "Toward Low-Energy Spark-Plasma Sintering of Hot-Deformed Nd-Fe-B magnets" authored by M. Korent, M. Soderžnik, U. Ročnik, S. Drev, K. Žužek Rožman, S. Šturm, S. Kobe, and K. Žagar Soderžnik. The article was published in the International Journal of Materials Science and Applications, vol. 10, 2021, p. 98-107, (doi: 10.11648/j.ijmsa.20211005.12).

The spark-plasma-sintering (SPS) method was used to process a hot-deformed (HD) Nd-Fe-B magnet with significantly lower energy consumption compared to the conventional SPS process. Commercial MQU-F Nd-Fe-B ribbons with nominal composition $Nd_{30.1}Pr_{0.4}Fe_{62.0}Co_{6.1}Ga_{0.5}B_{0.9}$ (wt.%) were used for the fabrication of a magnet with an anisotropic microstructure. The ribbons were firstly compacted into a fully dense magnet in a 10-mm graphite mould at 675 °C under an applied pressure of 50 MPa. The HP magnets were then subsequently hot-deformed in a 20-mm graphite mould at two different temperatures and maximum applied pressure of 90 MPa.

The low-energy processing (LEP) hot-deformed magnet was processed at a nominal SPS temperature of 350 °C, meanwhile the high-energy-consumption (HEP) hot-deformed magnet at a nominal SPS temperature 680 °C. During the deformation process of low-energy processing hot-deformed magnet, 0.37 MJ of energy was consumed, which is more than three times less than for the high-energy processing hot-deformation process (1.2 MJ). Both HD magnets were then post-annealed at 650 °C for 120 min in a vacuum to further improve the magnetic properties.

After the post-annealing process, the low-energy processing hot-deformed magnet showed a remanent magnetization of 1.27 T and coercivity of 1327 kA/m (1.67 T). On the other hand, the high-energy processing hot-deformed magnet showed a similar coercivity of 1337 kA/m (1.67 T) and only 0.04 T higher remanent magnetization (1.31 T).

A small deficiency in magnetic properties of low-energy processing hot-deformed magnet was revealed by the microstructural characterization and statistical analyses, which showed a better texture orientation for the high-energy processing hot-deformed magnet and indicated the reason for the lower remanent magnetization and reduced squareness in the case of the low-energy processing. The results also show that although the low-energy-processing hot-deformed magnet was processed with a three-times-lower energy consumption, the maximum energy product is only 8 % lower than the maximum energy product of the high-energy processing hot-deformed magnet.

In this work, we have shown that the hot-deformed magnet can be produced with significantly lower energy consumption if one applies a proper method for its fabrication. However, further studies are needed to further resolve and even more improve the magnetic properties of hot-deformed magnets.

International Journal of Materials Science and Applications
2021; 10(5): 98-107
http://www.sciencepublishinggroup.com/j/ijmsa
doi: 10.11648/j.ijmsa.20211005.12
ISSN: 2327-2635 (Print); ISSN: 2327-2643 (Online)

Toward Low-Energy Spark-Plasma Sintering of Hot-Deformed Nd-Fe-B Magnets

Matic Korent[1, 2, *], Marko Soderznik[1, 3], Urska Rocnik[1], Sandra Drev[4], Kristina Zuzek Rozman[1, 2], Saso Sturm[1, 2], Spomenka Kobe[1, 2], Kristina Zagar Soderznik[1]

[1]Department for Nanostructured Materials, Jozef Stefan Institute, Ljubljana, Slovenia

[2]Jozef Stefan International Postgraduate School, IPS, Ljubljana, Slovenia

[3]Laboratory for Tribology and Interface Nanotechnology (TINT), Faculty for Mechanical Engineering, University of Ljubljana, Ljubljana, Slovenia

[4]Center for Electron Microscopy and Microanalysis, Jozef Stefan Institute, Ljubljana, Slovenia

Email address:
matic.korent@ijs.si (M. Korent), marko.soderznik@gmail.com (M. Soderznik), urska.rocnik@gmail.com (U. Rocnik), sandra.drev@ijs.si (S. Drev), tina.zuzek@ijs.si (K. Z. Rozman), saso.sturm@ijs.si (S. Sturm), spomenka.kobe@ijs.si (S. Kobe), kristina.zagar@ijs.si (K. Z. Soderznik)

[*]Corresponding author

To cite this article:
Matic Korent, Marko Soderznik, Urska Rocnik, Sandra Drev, Kristina Zuzek Rozman, Saso Sturm, Spomenka Kobe, Kristina Zagar Soderznik. Toward Low-Energy Spark-Plasma Sintering of Hot-Deformed Nd-Fe-B Magnets. *International Journal of Materials Science and Applications*. Vol. 10, No. 5, 2021, pp. 98-107. doi: 10.11648/j.ijmsa.20211005.12

Received: August 24, 2021; **Accepted**: September 13, 2021; **Published**: September 29, 2021

Abstract: High-coercivity Nd-Fe-B permanent magnets are key materials for producing electrical components on the macro- and nanoscale. We present a newly developed, economically efficient method for processing Nd-Fe-B magnets based on spark-plasma sintering (SPS) that makes it possible to retain the technologically essential properties of the magnet, but by consuming about 30% less energy compared to the conventional SPS process. A magnet with an anisotropic microstructure was fabricated from MQU-F commercial ribbons with a low energy consumption (0.37 MJ) during the deformation process and compared to a conventionally prepared hot-deformed magnet that consumed three-times more energy (1.2 MJ). Both magnets were post-annealed at 650°C for 120 min in a vacuum. After the post-annealing process, the low-energy processing (LEP) hot-deformed magnet exhibited a coercivity of 1327 kAm^{-1}, and a remanent magnetization of 1.27 T. In comparison, the high-energy processing (HEP) hot-deformed magnet had a coercivity of 1337 kAm^{-1} and a remanent magnetization of 1.31 T. A complete microstructural characterization and detailed statistical analyses revealed a better texture orientation for the HEP hot-deformed magnet processed with the larger energy consumption. This texture is the main reason for the difference in the remanent magnetization between the two hot-deformed magnets. The results show that although the LEP hot-deformed magnet was processed with three-times less energy than in a typical hot-deformation process, the maximum energy product is only 8% lower than that of a HEP hot-deformed magnet.

Keywords: Hot-Deformed Nd-Fe-B Magnets, Low-Energy Processing Hot-Deformation Process, Spark-Plasma Sintering, Statistical Analyses, Electron Microscopy

1. Introduction

Discovered in 1984 [1, 2], Nd-Fe-B magnets are those with the highest maximum energy product $(BH)_{max}$, more than 400 kJm^{-3}, which is close to the theoretical limit of 512 kJm^{-3} [3-7]. Thus, they are in a very high demand for major applications in electric and hybrid vehicles, traction motors, and wind turbines [8, 9]. $Nd_2Fe_{14}B$ has a tetragonal crystal structure with a $P4_2/mnm$ space group [10]. To achieve a large remanent magnetization ($\mu_0 M_r$) and consequently a large value of $(BH)_{max}$ for a magnet with such a composition, a high degree of (001) texture must be introduced [11, 12]. In addition, a high-volume percentage of the $Nd_2Fe_{14}B$ phase, a low oxygen content, a small amount of non-ferromagnetic

material and a small crystallite size, close to the single-domain size (~ 250 nm), is desirable [13]. Besides the sintering of magnetically pre-aligned particles, the hot-deformation (HD) process is a method in which the grain-boundary migration and sliding of crystal planes are induced by plastic deformation [11, 12, 14]. In 1985, Lee et al. and Tang et al. [15-17] produced HD magnets having an ultrafine microstructure with an average grain size from 300 nm to 400 nm from melt-spun Nd-Fe-B ribbons. The rapidly solidified powder with randomly orientated nanocrystals was transformed into textured, closely packed, plate-like grains with a high degree of *c*-axis alignment along the pressing direction during the HD process, resulting in a large $\mu_0 M_r$ [18, 19]. Recently, Tang et al. prepared ribbons with a small addition of Nb (0.29 wt.%) and performed the HD process at 850°C to obtain a HD magnet with a 75% height reduction and a $\mu_0 M_r$ of 1.45 T, which is comparable to the values of sintered magnets [11, 20].

The coercivity ($\mu_0 H_c$) of HD magnets greatly depends on the homogenous distribution of Nd-rich phases around the $Nd_2Fe_{14}B$ grains [21]. Sufficient magnetic isolation effectively enhances the value of the coercivity with a reduction of the exchange coupling between the $Nd_2Fe_{14}B$ grains [21, 22]. Furthermore, it acts as a barrier to prevent domain-wall motion during the magnetization-reversal process [12, 23, 24]. However, detailed microstructure investigations by Lewis et al. and Liu et al. showed that the Nd-rich intergranular phase contains up to 50 at.% ferromagnetic elements (pure metals of Fe and Co), which suggests the ferromagnetic nature of the isolation phase and consequently the exchange coupling between $Nd_2Fe_{14}B$ grains [21, 25, 26]. Consequently, Liu et al. showed that heavy-rare-earth-free HD magnets could have a $\mu_0 H_c$ only up to 1430 kAm^{-1} at room temperature (RT) [21].

In addition to the microstructure characteristics, processing conditions have a significant impact on the magnetic properties of HD magnets. According to Hioki et al., both the reduction ratio and hot-deformation temperature define the final $\mu_0 M_r$, $\mu_0 H_c$, and $(BH)_{max}$ [27]. The value of $\mu_0 M_r$ is closely related to the reduction ratio, as established by Korent et al. [28]. The increase in $\mu_0 M_r$ is proportional to the reduction ratio, due to the higher degree of texture and a predominant c-plane growth of the $Nd_2Fe_{14}B$ grains [12, 27]. Additionally, the working temperature is important in terms of grain growth as it causes a deterioration of the magnetic properties [27].

Typically, HD magnets are hot-pressed (HP) (Figure 1a) with heating rates that are rather low, i.e., 5–10°C min^{-1} [29]. Usually, the system includes a coil and the heating is based on induction or electrical resistance [30]. Another option for similar processing is the spark-plasma sintering (SPS) method (Figure 1b), in which the densification process is simultaneously applied by a uniaxial pressure and a large pulse of direct current (DC) [29]. The application of a mechanical force is like that in the HP process. Meanwhile, the heating rates, up to 1000°C min^{-1}, are much higher in comparison to HP magnets [29]. Efficient and rapid densification in the SPS method occurs through a combination of Joule heating, the action of spark discharge, the plastic-deformation effect, and the diffusion of material [31]. However, according to Chawake et al., Joule heating is the primary source of heat during the densification of metal powders [32]. The heating occurs due to the electrical resistance, which is most significant during the contact between the particles [32]. Consequently, the SPS process enables ultra-fast sintering at low temperatures and short holding times to achieve full material density, which preserves the magnetic properties and reduces the power consumption of the process itself [33, 34].

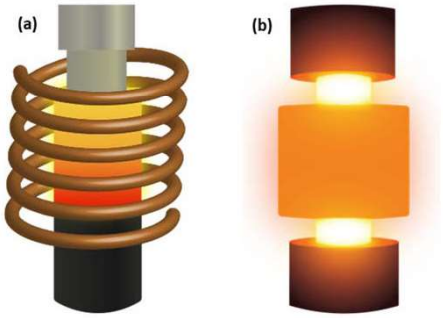

Figure 1. *Schematic of (a) HP method and (b) SPS method.*

In this work, the SPS method was used to fabricate a fully dense HD Nd-Fe-B magnet with a high deformation ratio based on the low-energy processing (LEP) SPS method. The microstructure and its influence on the final magnetic properties were studied and the results obtained were compared to the microstructure of a HD magnet produced using the high-energy processing (HEP) SPS method.

2. Experimental

Commercial (MQU-F) Nd-Fe-B melt-spun ribbons with the nominal composition $Nd_{30.1}Pr_{0.4}Fe_{62.0}Co_{6.1}Ga_{0.5}B_{0.9}$ (wt.%) were used for the HD process. MQU-F ribbons were first HP into a fully dense magnet using a SPS furnace (Fuji Electronic Industrial Dr Sinter SPS Syntex 3000). The magnet was compacted in a 10-mm graphite mold at 675°C under a uniaxially applied pressure of 50 MPa in a vacuum (≈ 5×10^{-2} mbar). The SPS temperature was controlled by a K-type thermocouple inserted into the graphite mold at the level of the sample. The thickness of the graphite wall splitting the thermocouple from the sample was minimal (≈1 mm). A 12:2 an on-off DC pulse sequence was applied to heat the sample. After the sintering process was finished, the pressure was immediately released and the mold with the sample was cooled to RT with water circulating through the system. The density of the HP magnet was determined using a bulk-density measurement system (Densitec, Exelia AG, Switzerland).

International Journal of Materials Science and Applications 2021; 10(5): 98-107 100

The HP magnets were subsequently HD in a 20-mm graphite mold at two different maximum SPS temperatures in a vacuum. The temperatures below are the nominal temperatures and serve as an SPS processing parameter to determine the energy consumption through the deformation process. The SPS settings and measurement were equal to the HP process described in the previous paragraph. For processing the LEP HD magnet, the SPS temperature was set to a nominal 350°C, and for the HEP HD magnet, at a nominal 680°C. In the first case (LEP HD magnet) the heating rate from RT to the nominal temperature of 300°C was 100°Cmin^{-1}, followed by a lower heating rate to the final temperature to minimize the overshoot. In the last minute, the temperature was maintained at the target temperature. The higher pressure was initially applied at a nominal temperature of 250°C, and within 3.5 min it increased to a maximum pressure of 90 MPa. After the target temperature was reached, the sintering process was stopped immediately and the pressure was released. Meanwhile, in the second case (HEP HD magnet), the heating rate from RT to 600°C was 75°Cmin^{-1}, followed by a lower heating rate to the final temperature to prevent the overshoot. In the last minute, the temperature was maintained at the target temperature, and the maximum pressure of 90 MPa was applied during this holding time. As prepared, the HD magnets were subjected to a post-annealing process at 650°C for 120 min in a vacuum. The magnetic properties of both HP spark-plasma-sintered HD magnets before and after annealing were measured with a permeameter (Steingroever EP2) at RT. The deformation ratio of the LEP HD magnet was 71%, and that of the HEP HD magnet, 75%. The deformation ratio (%) is defined as:

$$DR = ((h_{HP}-h_{HD})/h_{HP})\cdot 100\% \quad (1)$$

where DR represents the deformation ratio (%) and h_{HP}, h_{HD} are the heights of the HP, HD magnet (mm).

The X-ray powder-diffraction data were collected from the sample's surface perpendicular to the pressing direction with a Malvern Panalytical Empyrean X-ray diffractometer (XRD) using monochromated X-rays, produced by a Cu target tube (0.15406 nm). The scan range in Bragg angle was from 10° to 90° (2θ). The XRD data were analyzed with HighScore Plus XRD Analysis Software. The microstructural characterization using scanning electron microscopy (SEM) was performed to study the influence of the SPS temperature and pressure on the HD process. The samples were cut into smaller square blocks, and the surface parallel to the pressing direction was metallographically polished. After polishing, the surface was chemically etched with 3-M Cyphos solution for 10 s and then intensively washed with ethanol. For the SEM microstructural characterization, samples were analyzed using a high-resolution, field-emission-gun SEM (FEG-SEM) Thermo Fisher, Verios G4 HP. The acquired images were statistically processed using the ImageTool program to determine the difference in the grain size and aspect ratio, as measured between the long and short axes of the anisotropic $Nd_2Fe_{14}B$ grains of the HD magnets. Detailed microstructural investigations of the samples were performed with transmission electron microscopy (TEM) using a 200-kV microscope (TEM; JEM-2100, Jeol, Japan). For the TEM bulk-sample investigations, the sample was cut into square blocks of 1.8 × 1.8 mm^2, perpendicular and parallel to the pressing direction. The blocks were fitted into 3-mm brass cylinders using epoxy glue to improve the strength. The TEM specimen was ground to a thickness of 100 µm and dimpled down to 15 µm at the disc center (Dimple grinder, Gatan Inc., Warrendale PA, USA). The TEM specimen was finally ion-milled (PIPS, Precision Ion Polishing System, Gatan Inc., USA) using 3-kV Ar^{+} ions at an incidence angle of 8° until perforation.

3. Results

3.1. LEP Vs HEP HD Magnet

Two differently prepared HD magnets could be distinguished based on the energy consumption for the deformation process. Figure 2 shows the electrical power (P) consumption during the SPS process of the LEP and HEP HD magnets. The energy consumption is the time integral of the electrical power, and its value was obtained from the area below the curves. During the deformation process of the LEP HD magnet, the consumed energy was 0.37 MJ, which is more than three-times less than the 1.2 MJ consumed in the HEP HD process.

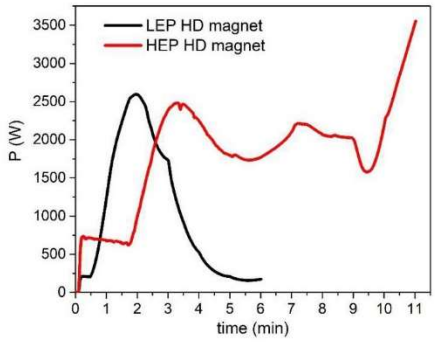

Figure 2. *Electrical power (P) consumption during the SPS process of LEP HD magnet (black curve) and HEP HD magnet (red curve). The area under the curve was obtained from a numerical integration* $\int_0^{t_{end}} P \cdot dt$. *The calculated energy consumptions are 0.37MJ for the LEP hot-deformation process and 1.2 MJ for HEP hot-deformation process.*

3.2. Magnetic Properties

Figure 3 shows the demagnetization curves of the LEP and HEP HD magnets before and after the post-annealing treatment at 650°C for 120 min. Note that the magnets were fully magnetized in a pulse magnetizer with 6 T before each measurement.

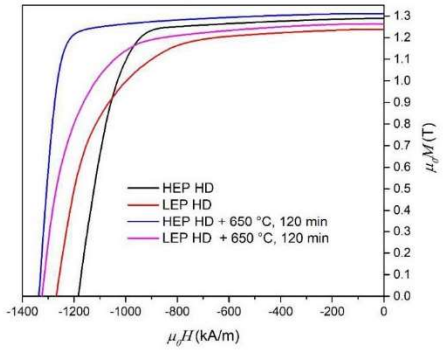

Figure 3. *Demagnetization curves of LEP HD magnet (red curve) and HEP HD magnet (black curve) and demagnetization curves of LEP (purple curve) and HEP (blue curve) HD magnets after the post-annealing process at 650°C for 120 min.*

The magnetic properties and the squareness (Q) of the demagnetization curves of each HD magnet are collected in Table 1. The $\mu_0 M_r$ of the LEP HD magnet was enhanced with the post-annealing treatment from 1.24 T to 1.27 T, and $\mu_0 H_c$ from 1271 kAm^{-1} to 1327 kAm^{-1}. A similar improvement after post-annealing in $\mu_0 M_r$, from 1.29 T to 1.31 T, was also observed in the HEP HD magnet. Meanwhile, the enhancement in coercivity of the HEP HD magnet after the post-annealing process was more significant—from 1184 kAm^{-1} to 1337 kAm^{-1}. The squareness of the demagnetizing curves was also improved after additional heating. In the case of the LEP HD magnet, the squareness was enhanced from 70% to 77%, and in the case of the HEP HD magnet from 82% to 91%. The squareness is defined as:

$$Q = \mu_0 H_k / \mu_0 H_c \cdot 100\% \quad (2)$$

where $\mu_0 H_k$ is a field value corresponding to the location of the knee point in the intrinsic curve at 90% of $\mu_0 M_r$ [35].

Table 1. *Magnetic properties ($\mu_0 H_c$, $\mu_0 M_r$, $(BH)_{max}$) and Q of the demagnetizing curves of LEP, HEP HD magnets and of LEP, HEP HD magnets after the post-annealing process at 650°C for 120 min.*

	LEP HD magnet	HEP HD magnet	LEP HD magnet + 650°C, 120 min	HEP HD magnet + 650°C, 120 min
$\mu_0 H_c$ (kAm^{-1})	1271	1184	1325	1337
$\mu_0 M_r$ (T)	1.24	1.29	1.27	1.31
$(BH)_{max}$ (kJm^{-3})	295	320	310	335
Q (%)	70	82	77	91

3.3. Microstructural Characterization

Figure 4 shows the XRD patterns of the LEP and HEP HD magnets after the post-annealing process. The analysis was performed on the surface perpendicular to the pressing direction. The characteristic peaks with directions (004), (105), (006), and (008) of the anisotropic microstructure are labelled in the chart.

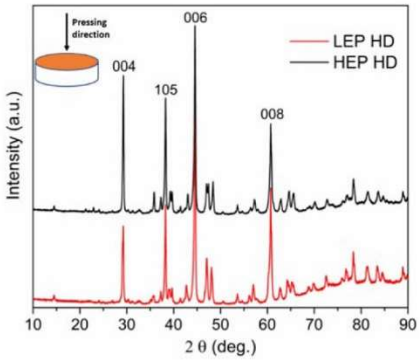

Figure 4. *XRD patterns of LEP and HEP HD magnets after the post-annealing process at 650°C for 120 min.*

A backscattered-electron (BSE) SEM characterization was performed on the central part of the LEP and HEP HD magnets, to understand the influence of microstructure on the magnetic properties. Figure 5 shows cross-section images of (a) the LEP and (b) the HEP HD magnets after the post-annealing process, where the direction of the *c*-axis is the same as the pressure direction. Note, that the BSE SEM results of the LEP and HEP HD magnets prior to the annealing process gave identical results. In both images, coarse grains and grains with random orientations can be seen, especially in the LEP HD magnet. The main difference between those two magnets is in the microstructure texturing. A HEP HD magnet has a stronger *c*-axis alignment of the $Nd_2Fe_{14}B$ grains along the pressing direction than the LEP HD magnet, which will be confirmed later with more detailed information about the shape and orientation of the grains.

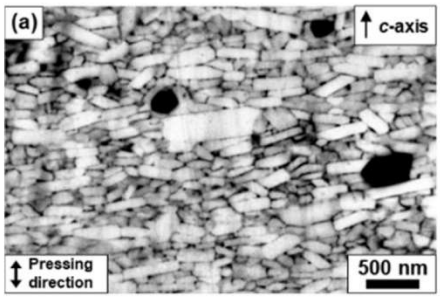

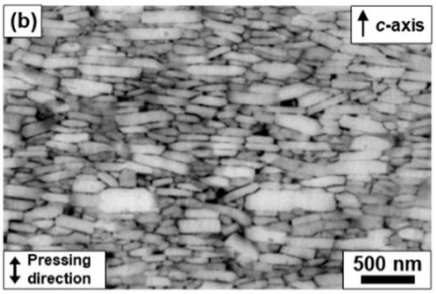

Figure 5. *BSE SEM images of (a) LEP and (b) HEP HD magnet. (The SEM analyses were performed after the post-annealing process at 650°C for 120 min.).*

Based on the BSE SEM images, histograms and standard-distribution curves were obtained by counting the width and height of 200 characteristic grains that are not overlapped by others. Figure 6 shows the height and width distribution of the post-annealed LEP HD magnet (a, b) and HEP HD magnet (c, d). The LEP HD magnet has a broader grain-height distribution with an average height of 63 nm (Figure 6a), compared to the HEP HD magnet with an average height of 67 nm (Figure 6c). In the LEP HD magnet, 5% of the grains are larger than 160 nm, whereas in the HEP HD magnet this is not the case. In contrast, the width-distribution curve of the HEP HD magnet (Figure 6d) is broader, with a more significant number of long grains and an average width of 348 nm. Almost 100 nm lower, the average grain width of 252 nm is observed in the LEP HD magnet (Figure 6b).

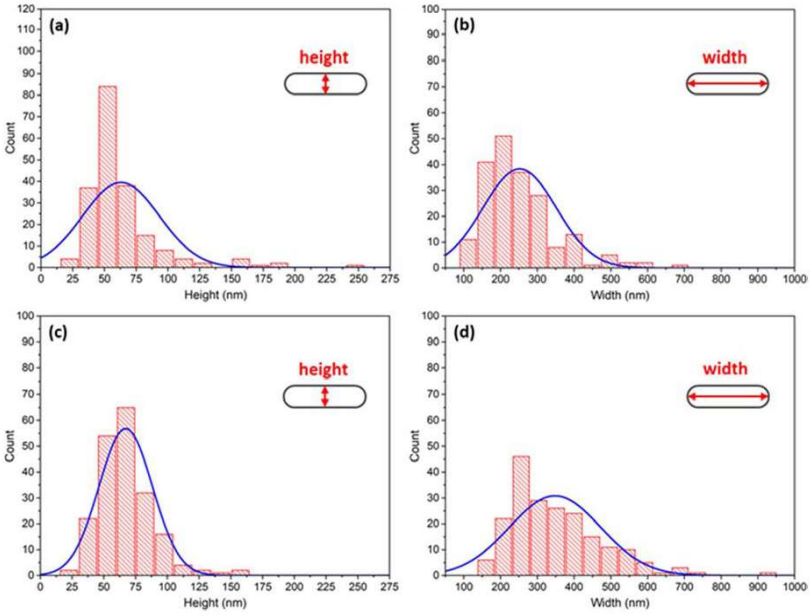

Figure 6. *Statistical distribution of the height and width of 200 grains of the (a), (b) LEP and (c), (d) HEP HD magnets. (All statistical distributions were performed on the samples after the post-annealing process at 650°C for 120 min.).*

The aspect ratio (width/height) was calculated based on each grain's width and height. Figures 7 a, c presents the histograms and distributions of aspect ratios of 200 grains, where (a) illustrates the LEP and (c) the HEP HD magnets after post-annealing. The standard distribution curve of the analyzed grains from the HEP HD sample is broader, with an average aspect ratio of ~5.3. The LEP HD sample possesses grains with an aspect ratio between 2 and 6.5 and subsequently has a narrower distribution curve. The average aspect ratio is consequently lower, at ~4.2. Figure 7 also shows the angle between the pressing direction and the c-axes of the grains of (b) the LEP and (d) the HEP HD samples after post-annealing. In this case, the LEP HD sample's grain-distribution curve is broad, which means that many grains have an orientation out of the pressing direction. The average deviation angle is 8.3°. The HEP HD sample has a narrower distribution curve and a smaller number of grains with a high deviation angle from the pressing direction. The average deviation angle is 7.4°, which is almost 1° lower than in the LEP HD sample.

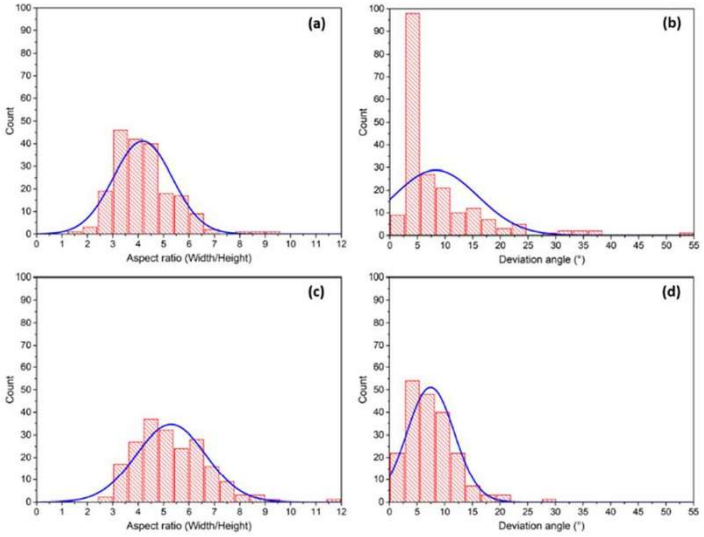

Figure 7. *Statistical distribution of the aspect ratio (width/height) and deviation angle of 200 grains of (a), (b) LEP and (c), (d) HEP HD magnet. (All statistical distributions were performed after the post-annealing process at 650°C for 120 min.).*

Detailed TEM analysis (Figure 8) with selected-area electron-diffraction (SAED) patterns were performed parallel and perpendicular to the pressing direction of the LEP and HEP HD samples after the post-annealing process. Figures 8 (a, b) shows grains parallel to the *c*-axis. The low-magnification images show the size and shape of anisotropic grains that correspond to the SEM findings. Analysis of the grains determined a misalignment of ± 2–3 degrees from the preferential plane. From a detailed analysis of the diffraction patterns, we confirmed that the preferred orientation of the grains is in the (0-10) direction for both the LEP and HEP HD magnets.

Figures 8 (c, d) shows grains perpendicular to the *c*-axis. Low-magnification images of the LEP and HEP HD samples revealed the idiomorphic shape of the grains with a diameter of 0.1–0.8 µm. Analyses of the grains determined a misalignment of ±1–2 degrees from a preferential plane. Detailed analyses of the diffraction patterns show the preferential [001] plane of the grains that are related to the XRD analysis.

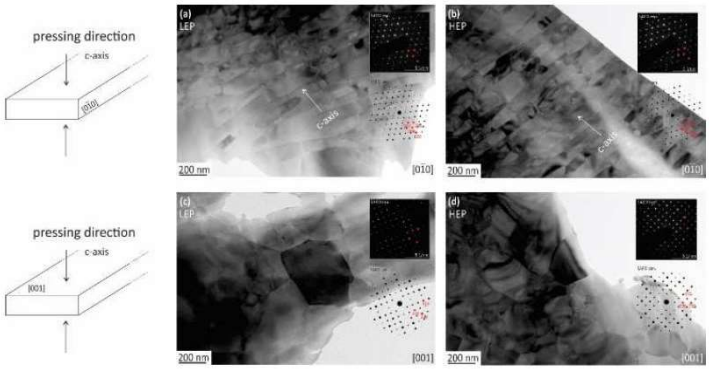

Figure 8. *TEM analyses and SAED diffraction patterns (experimental and simulated) of (a) and (c) LEP HD and (b) and (d) HEP HD samples. The analyses were performed parallel and perpendicular to the c-axis (pressing direction). (TEM analyses were performed after the post-annealing process at 650°C for 120 min.).*

International Journal of Materials Science and Applications 2021; 10(5): 98-107 104

4. Discussion

The amount of energy transferred to the sample influences the temperature gradient in the hot-deformation process. Less energy should be reflected in a lower average temperature of the sample, which in the experiment is compensated by applying a specific pressure regime, so making the desired microstructure transformations possible.

The HEP HD magnet was processed at a nominal temperature comparable to previously set temperatures using the same technique and material. For example, S. Liu et al. produced a HD magnet at 700°C [36] and Z. H. Hu et al. at 650–750°C [37]. We showed that the energy consumed during the deformation process is strongly related to the temperature regime, which indicates that a large amount of energy is consumed in a typical hot-deformation process. If the deformation temperature is lower, a large amount of energy can be saved. In our case during the LEP HD magnet's deformation process, the 0.37 MJ of energy was consumed, while the HEP HD magnet's processing consumed three-times more energy. Moreover, assuming an average working power of 8 kW running for approximately 10 min, a conventional hot-pressing machine consumes at least 10-times more energy for the hot-deformation process compared to LEP SPS.

We performed the XRD analysis perpendicular to the *c*-axis on the LEP and HEP HD magnets to confirm the *c*-axis crystallographic alignment. The XRD patterns of the LEP and HEP HD magnets after the post-annealing process show the enhanced intensity of the characteristic peaks (004), (006), (008), and (105), which indicates the development of the *c*-axis crystallographic alignment [38]. In parallel with the XRD, a TEM analysis was performed. The LEP and HEP HD samples' diffraction patterns coincide with the XRD results, which is an additional indicator of an anisotropic microstructure. From the perspective of magnetic properties, we achieved a high deformation of ~71% in the LEP HD magnet and ~75% in the HEP HD magnet. Hioki et al. showed that the $\mu_0 M_r$ of a HD magnet changed between 70% and 75% of height reduction by only 0.02 T, and it remained unchanged above 75% [27]. Consequently, we can assume that in our case, height reduction has a partial influence on $\mu_0 M_r$ for HD magnets. However, despite the considerable height reduction in the HD magnets, there is still a visible difference of 0.05 T in $\mu_0 M_r$ between the LEP HD magnet (1.24 T) and the HEP HD magnet (1.29 T), which can be attributed to the uniformity of the grain shape and orientation. The texture-formation mechanism for plate-like grain growth and alignment can be described by a solution-precipitation-creep model with the assistance of the Nd-rich phase [39-41]. Leonowicz et al. considered that liquid Nd-rich grain-boundary phases induce the sliding of grains under an applied shear stress, which results in the magnets' deformation and texture formation [42]. To understand the origin of the difference in magnetic properties between the LEP and HEP HD magnets, the shape and orientation of particular grains in the microstructure were investigated. In the case of the HEP HD magnet, the plate-like grains have a relatively uniform shape and orientation of the *c*-axis parallel to the pressing direction. On the other hand, in the LEP HD magnet, the plate-like grains have a less-uniform shape and more scattered orientation. Castle et al. [43] reported that the reason for the uniform microstructure of the HD magnet is a more even temperature distribution across the powder flakes during the sintering. This implies that in the case of processing the LEP HD magnet, the temperature was uneven throughout the sample, which caused the non-uniformity in the final microstructure.

The above-described findings were supported by the counted data, where the results showed a higher aspect ratio between the width and the height of grains in the HEP HD magnet's microstructure. The average aspect ratio of ~5.3 was significantly higher than that for the LEP HD magnet (~4.2). The aspect ratio is closely connected to the degree of deformation, which gives a partial explanation for the higher $\mu_0 M_r$ and lowers the $\mu_0 H_c$ of the HEP HD magnet [12, 40]. To better understand the difference in $\mu_0 M_r$, we also measured the angle between the grains' *c*-axes and the pressing direction for 200 grains from each HD magnet. Just as with the aspect ratio, the result showed a better grain orientation in the HEP HD magnet. The average deviation angle from the pressing direction is almost 1° lower than for the LEP HD magnet, 8.3°. This indicates better grain orientation for the HEP HD magnet and, consequently, higher $\mu_0 M_r$ and higher $(BH)_{max}$ [40]. From this set of analyzed data, we can also infer the shape of the demagnetization curve. Diverse grain shapes and their more imperfect orientations have a crucial impact on the reduced squareness of the LEP HD magnet [35].

From the perspective of $\mu_0 H_c$, the MQU-F ribbons were chosen for the deformation process due to their rich Nd content. There is 30.1 wt.% Nd in the material composition, which is 4.1 wt.% above the stoichiometric point. Liu et al. showed that within ribbons with a high Nd content, the fraction of Nd-rich phase increased along the grain boundaries [21]. Due to the increase in the Nd content and the decrease of the Fe and Co content in the grain boundaries, better isolation of the $Nd_2Fe_{14}B$ grains is established, which results in a higher value of $\mu_0 H_c$ [21]. The value of $\mu_0 H_c$ is higher for the LEP HD magnet, 1271 kAm^{-1}, compared to the value for the HEP HD magnet, 1184 kAm^{-1}. After the additional post-annealing step at 650°C for 120 min, all the magnetic properties were enhanced, presumably due to the removal of internal stress and/or defects [44]. The $\mu_0 M_r$ and $\mu_0 H_c$ of the LEP HD magnet were increased by 0.3 T and 54 kAm^{-1} compared to those of the HEP HD magnet, 0.2 T and 153 kAm^{-1}. According to Yin et al., the inherited crystalline orientation and improved texture promote the remanent magnetization after the post-annealing process [45].

Meanwhile, the post-annealing process's coercivity promotion is mainly related to the Nd-rich phase's enhanced distribution at the grain boundaries and the ribbon boundaries [45]. The LEP HD magnet's squareness was improved from 70% to 77%, and the HEP HD magnet from

82% to 91%. The microstructure homogeneity through the grain size distribution, grain shape, grain surface, and spatial distribution is improved by a post-annealing process, which is also the main reason for the enhanced squareness [35, 46]. Based on the statistical analyses, BSE SEM and TEM images, the HEP HD magnet's microstructure is more homogenous than the microstructure of the LEP HD magnet, which leads to a better squareness of the HEP HD magnet. Given the magnetic properties figure of merit improvement, both HD magnets exhibited ~5% higher value of $(BH)_{max}$ after the post-annealing process.

5. Conclusions

LEP and HEP HD magnets were processed using an SPS technique, which uses less energy than the typical hot-deformation process. The microstructural and magnetic properties of the LEP and HEP HD magnets were investigated, and a detailed analytical comparison was performed. Prior to the characterization, the post-annealing step of both HD magnets was performed to further enhance the magnetic properties. The LEP HD magnet had a just 0.04 T lower remanent magnetization than the HEP HD magnet (1.31 T). After post-annealing, both magnets' coercivities are similar: 1325 kAm^{-1} for the LEP HD and 1337 kAm^{-1} for the HEP HD. A minor deficiency in the magnetic properties for the LEP HD magnet was revealed by statistical analyses, which showed a better texture orientation for the HEP HD magnet. The results indicated a slightly lower remanent magnetization and reduced squareness for the LEP HD magnet.

A hot-deformed magnet with a significantly lower energy consumption can be produced if a proper fabrication method is applied. Further studies are underway to resolve the mechanism of texture formation during low-energy processing and to generate even better magnetic properties for the HD magnets.

Acknowledgements

This work was supported by projects ID PR-08336 and P2-0084 of the Slovenian Research Agency.

References

[1] M. Sagawa, K. Hiraga, H. Yamamoto, and Y. Matsuura, "Permanent magnet materials based on the rare earth-iron-boron tetragonal compounds (invited)," *IEEE Trans. Magn.*, vol. 20, no. 5, pp. 1584–1589, 1984, doi: 10.1109/TMAG.1984.1063214.

[2] J. J. Croat, J. F. Herbst, R. W. Lee, and F. E. Pinkerton, "High-energy product Nd-Fe-B permanent magnets," *Appl. Phys. Lett.*, vol. 44, no. 1, pp. 148–149, 1984, doi: 10.1063/1.94584.

[3] Yanglong Hou and David J. Sellmyer, *Magnetic nanomaterials: Fundamentals synthesis and applications*. Wiley-VCH Verlag GmbH, 2017.

[4] T. Zhang *et al.*, "Hot-deformed Nd-Fe-B magnets fabricated by dynamic loading with a high maximum energy product," *Intermetallics*, vol. 73, pp. 67–71, 2016, doi: 10.1016/j.intermet.2016.04.001.

[5] T. Saito, M. Fujita, T. Kuji, K. Fukuoka, and Y. Syono, "The development of high performance Nd-Fe-Co-Ga-B die upset magnets," *J. Appl. Phys.*, vol. 83, no. 11, pp. 6390–6392, 1998, doi: 10.1063/1.367522.

[6] K. Hono and H. Sepehri-Amin, "Strategy for high-coercivity Nd-Fe-B magnets," *Scr. Mater.*, vol. 67, no. 6, pp. 530–535, 2012, doi: 10.1016/j.scriptamat.2012.06.038.

[7] M. Yue, M. Tian, J. X. Zhang, D. T. Zhang, P. L. Niu, and F. Yang, "Microstructure and magnetic properties of anisotropic Nd-Fe-B magnets produced by spark plasma sintering technique," *Mater. Sci. Eng. B Solid-State Mater. Adv. Technol.*, vol. 131, no. 1–3, pp. 18–21, 2006, doi: 10.1016/j.mseb.2005.11.010.

[8] U. M. R. Seelam *et al.*, "Coercivity of the Nd-Fe-B hot-deformed magnets diffusion-processed with low melting temperature glass forming alloys," *J. Magn. Magn. Mater.*, vol. 412, pp. 234–242, 2016, doi: 10.1016/j.jmmm.2016.04.005.

[9] M. Soderžnik, M. Korent, K. Žagar Soderžnik, M. Katter, K. Üstüner, and S. Kobe, "High-coercivity Nd-Fe-B magnets obtained with the electrophoretic deposition of submicron TbF3 followed by the grain-boundary diffusion process," *Acta Mater.*, vol. 115, pp. 278–284, 2016, doi: 10.1016/j.actamat.2016.06.003.

[10] D. Givord, H. S. Li, and J. M. Moreau, "Magnetic properties and crystal structure of $Nd_2Fe_{14}B$," *Solid State Commun.*, vol. 50, no. 6, pp. 497–499, 1984, doi: 10.1016/0038-1098(84)90315-6.

[11] X. Tang, H. Sepehri-Amin, T. Ohkubo, and K. Hono, "Suppression of non-oriented grains in Nd-Fe-B hot-deformed magnets by Nb doping," *Scr. Mater.*, vol. 147, pp. 108–113, 2018, doi: 10.1016/j.scriptamat.2017.12.032.

[12] Y. H. Hou, Y. L. Huang, Z. W. Liu, D. C. Zeng, S. C. Ma, and Z. C. Zhong, "Hot deformed anisotropic nanocrystalline NdFeB based magnets prepared from spark plasma sintered melt spun powders," *Mater. Sci. Eng. B Solid-State Mater. Adv. Technol.*, vol. 178, no. 15, pp. 990–997, 2013, doi: 10.1016/j.mseb.2013.06.009.

[13] O. Gutfleisch, "Controlling the properties of high energy density permanent magnetic materials by different processing routes," *J. Phys. D. Appl. Phys.*, vol. 33, no. 17, 2000, doi: 10.1088/0022-3727/33/17/201.

[14] R. K. Mishra, E. G. Brewer, and R. W. Lee, "Grain growth and alignment in hot deformed Nd-Fe-B magnets," *J. Appl. Phys.*, vol. 63, no. 8, pp. 3528–3530, 1988, doi: 10.1063/1.340731.

[15] R. W. Lee, "Hot-pressed neodymium-iron-boron magnets," *Appl. Phys. Lett.*, vol. 46, no. 8, pp. 790–791, 1985, doi: 10.1063/1.95884.

[16] R. W. Lee, E. G. Brewer, and N. A. Schaffel, "MAGNETS," *IEEE Trans. Magn.*, vol. M, no. 5, pp. 1958–1963, 1985.

[17] X. Tang *et al.*, "Relationship between the thermal stability of coercivity and the aspect ratio of grains in Nd-Fe-B magnets: experimental and numerical approaches," *Acta Mater.*, 2019, doi: 10.1016/J.ACTAMAT.2019.11.038.

[18] J. Liu *et al.*, "Grain size dependence of coercivity of hot-deformed Nd-Fe-B anisotropic magnets," *Acta Mater.*, vol. 82, pp. 336–343, 2015, doi: 10.1016/j.actamat.2014.09.021.

[19] X. D. Xu *et al.*, "Comparison of coercivity and squareness in hot-deformed and sintered magnets produced from a Nd-Fe-B-Cu-Ga alloy," *Scr. Mater.*, vol. 160, pp. 9–14, 2019, doi: 10.1016/j.scriptamat.2018.09.028.

[20] H. Sepehri-Amin, Y. Une, T. Ohkubo, K. Hono, and M. Sagawa, "Microstructure of fine-grained Nd-Fe-B sintered magnets with high coercivity," *Scr. Mater.*, vol. 65, no. 5, pp. 396–399, 2011, doi: 10.1016/j.scriptamat.2011.05.006.

[21] J. Liu *et al.*, "Effect of Nd content on the microstructure and coercivity of hot-deformed Nd-Fe-B permanent magnets," *Acta Mater.*, vol. 61, no. 14, pp. 5387–5399, 2013, doi: 10.1016/j.actamat.2013.05.027.

[22] M. Soderžnik, B. Ambrožič, K. Žagar Soderžnik, and M. Korent, "Limits of grain boundary engineering in nanocrystalline Nd-Fe-B melt-spun ribbons," *Mater. Lett.*, vol. 264, pp. 20–22, 2020, doi: 10.1016/j.matlet.2020.127338.

[23] J. Liu, H. Sepehri-Amin, T. Ohkubo, K. Hioki, A. Hattori, and K. Hono, "Microstructure evolution of hot-deformed Nd-Fe-B anisotropic magnets," *J. Appl. Phys.*, vol. 115, no. 17, pp. 15–18, 2014, doi: 10.1063/1.4867960.

[24] M. Soderžnik *et al.*, "Magnetization reversal process of anisotropic hot-deformed magnets observed by magneto-optical Kerr effect microscopy," *J. Alloys Compd.*, vol. 771, pp. 51–59, 2019, doi: 10.1016/j.jallcom.2018.08.231.

[25] L. H. Lewis, Y. Zhu, D. O. Welch, and L. Henderson, "Evidence for reversal by nucleation in REFeB dieupset magnets Evidence for reversal by nucleation in RE-Fe-B die-upset," vol. 6235, no. 1994, pp. 9–12, 2012, doi: 10.1063/1.358291.

[26] H. Sepehri-Amin *et al.*, "Microstructure and temperature dependent of coercivity of hot-deformed Nd-Fe-B magnets diffusion processed with Pr-Cu alloy," *Acta Mater.*, vol. 99, pp. 297–306, 2015, doi: 10.1016/j.actamat.2015.08.013.

[27] K. Hioki, T. Takano, and T. Yamamoto, "Influence of Process Conditions on the Magnetic Properties for Hot Deformed Magnets," *Denki-Seiko [Electric Furn. Steel]*, vol. 79, no. 2, pp. 119–125, 2008, doi: 10.4262/denkiseiko.79.119.

[28] M. Korent *et al.*, "Magnetic properties and microstructure evolution of hot-deformed Nd-Fe-B magnets produced by low-pressure spark-plasma sintering," *J. Magn. Magn. Mater.*, vol. 515, no. July, pp. 2–7, 2020, doi: 10.1016/j.jmmm.2020.167279.

[29] J. Trapp and B. Kieback, "Fundamental principles of spark plasma sintering of metals: part I–Joule heating controlled by the evolution of powder resistivity and local current densities," *Powder Metall.*, vol. 62, no. 5, pp. 297–306, 2019, doi: 10.1080/00325899.2019.1653532.

[30] J. W. Carson and B. H. Pittenger, "Advanced Aluminum Powder Metallurgy Alloys and Composites," *ASM Handb. Vol. 7 Powder Met. Technol. Appl.*, vol. 7, pp. 287–301, 1998, doi: 10.1361/asmhba00015.

[31] Z. H. Zhang, Z. F. Liu, J. F. Lu, X. B. Shen, F. C. Wang, and Y. D. Wang, "The sintering mechanism in spark plasma sintering - Proof of the occurrence of spark discharge," *Scr. Mater.*, vol. 81, pp. 56–59, 2014, doi: 10.1016/j.scriptamat.2014.03.011.

[32] N. Chawake, L. D. Pinto, A. K. Srivastav, K. Akkiraju, and B. S. Murty, "On Joule heating during spark plasma sintering of metal powders," *Scr. Mater.*, vol. 93, pp. 52–55, 2014, doi: 10.1016/j.scriptamat.2014.09.003.

[33] X. Q. Li, L. Li, K. Hu, Z. C. Chen, S. G. Qu, and C. Yang, "Microstructure and magnetic properties of anisotropic Nd-Fe-B magnets prepared by spark plasma sintering and hot deformation," *Trans. Nonferrous Met. Soc. China (English Ed.*, vol. 24, no. 10, pp. 3142–3151, 2014, doi: 10.1016/S1003-6326(14)63453-1.

[34] T. Tomše *et al.*, "A spark-plasma-sintering approach to the manufacture of anisotropic Nd-Fe-B permanent magnets," *J. Magn. Magn. Mater.*, vol. 502, no. October 2019, 2020, doi: 10.1016/j.jmmm.2020.166504.

[35] Y. Zhang *et al.*, "Squareness factors of demagnetization curves for multi-main-phase Nd-Ce-Fe-B magnets with different Ce contents," *J. Magn. Magn. Mater.*, vol. 487, no. May, 2019, doi: 10.1016/j.jmmm.2019.165355.

[36] S. Liu, N. H. Kang, L. Feng, S. H. Lee, J. H. Yu, and J. G. Lee, "Anisotropic Nanocrystalline Nd-Fe-B-Based Magnets Produced by Spark Plasma Sintering Technique," *IEEE Trans. Magn.*, vol. 51, no. 11, pp. 18–21, 2015, doi: 10.1109/TMAG.2015.2439672.

[37] Z. H. Hu, J. Li, L. H. Chu, and Y. Liu, "Effect of hot deformation temperature on the magnetic and mechanical properties of NdFeB magnets prepared by spark plasma sintering," *J. Magn. Magn. Mater.*, vol. 323, no. 1, pp. 104–107, 2011, doi: 10.1016/j.jmmm.2010.08.040.

[38] X. Tang, H. Sepehri-Amin, T. Ohkubo, K. Hioki, A. Hattori, and K. Hono, "Coercivities of hot-deformed magnets processed from amorphous and nanocrystalline precursors," *Acta Mater.*, vol. 123, pp. 1–10, 2017, doi: 10.1016/j.actamat.2016.10.026.

[39] F. Wang, W. Shen, J. Fan, J. Du, K. Chen, and J. P. Liu, "Strong texture in nanograin bulk Nd-Fe-B magnets via slow plastic deformation at low temperatures," *Nanoscale*, vol. 11, no. 13, pp. 6062–6071, 2019, doi: 10.1039/C9NR00107G.

[40] M. Zhu and W. Li, "Texture formation mechanism and constitutive equation for anisotropic thermorheological rare-earth permanent magnets," *AIP Adv.*, vol. 7, no. 5, 2017, doi: 10.1063/1.4978700.

[41] L. Li and C. D. Graham, "The Origin of Crystallographic Texture Produced During Hot Deformation in Rapidly-Quenched NdFeB Permanent Magnets," *IEEE Trans. Magn.*, vol. 28, no. 5, pp. 2130–2132, 1992, doi: 10.1109/20.179419.

[42] M. Leonowicz and H. A. Davies, "Effect of Nd content on induced anisotropy in hot deformed FeNdB magnets," *Mater. Lett.*, vol. 19, no. 5–6, pp. 275–279, 1994, doi: 10.1016/0167-577X(94)90170-8.

[43] E. Castle, R. Sheridan, W. Zhou, S. Grasso, A. Walton, and M. J. Reece, "High coercivity, anisotropic, heavy rare earth-free Nd-Fe-B by Flash Spark Plasma Sintering," *Sci. Rep.*, vol. 7, no. 1, pp. 1–12, 2017, doi: 10.1038/s41598-017-11660-9.

[44] H. R. Cha, K. W. Jeon, J. H. Yu, H. W. Kwon, Y. Do Kim, and J. G. Lee, "Coercivity enhancement of hot-deformed Nd-Fe-B magnet by grain boundary diffusion process using the reaction of NdHxand Cu nanopowders," *J. Alloys Compd.*, vol. 693, pp. 744–748, 2017, doi: 10.1016/j.jallcom.2016.09.167.

[45] W. Yin, R. Chen, X. Tang, J. Ju, and A. Yan, “Effect of pressless heat treatment on the magnetic performance and microstructure of hot-deformed Nd-Fe-B magnet,” *J. Magn. Magn. Mater.*, vol. 482, no. September 2018, pp. 9–13, 2019, doi: 10.1016/j.jmmm.2019.03.045.

[46] E. A. Périgo, H. Takiishi, C. C. Motta, and R. N. Faria, “Microstructure and squareness factor: A quantitative correlation in (Nd, Pr)FeB sintered magnets,” *J. Appl. Phys.*, vol. 102, no. 11, 2007, doi: 10.1063/1.2821756.

4.3 Paper "Significant Coercivity Enhancement of Hot-Deformed Nd-Fe-B Bulk Magnets by Two-Step Diffusion Process Using a Minimal Amount of Dy"

The next paper, entitled "Significant coercivity enhancement of hot-deformed Nd-Fe-B bulk magnets by two-step diffusion process using a minimal amount of Dy" and authored by M. Korent, X. Tang, H. Sepehri-Amin, K. Hioko, K.Z. Soderžnik, S. Kobe, A. Hattori, T. Ohkubo, K. Hono was published in Scripta Materialia, vol. 205, 2021, p.114207, (https://doi.org/10.1016/j.scriptamat.2021.114207).

Recently, Tang et al. introduced a novel method, the so-called two-step eutectic grain boundary diffusion process, where they treated a 5.6-mm thick HD magnet, and obtained a uniform microstructure [161]. In the first step, the HD magnet was GBDP with the addition of a low-melting-point $Nd_{40}Tb_{20}Dy_{10}Cu_{10}$ diffusion source, followed by 2nd step eutectic GBDP using $Nd_{80}Cu_{20}$. Due to the uniform microstructure, they improved the demagnetization curve's squareness, enhanced the processed magnet's coercivity from 0.91 T (725 kA/m) to 2.43 T (1934 kA/m), and the preserved the high remanence close to 1.3 T [161].

In this work, the main question was if in a two-step diffusion process comparable magnetic properties without using expensive Tb and minimum use of Dy can be obtained or not? The potential of a two-step grain boundary diffusion process was further exploited, using the $Nd_{50}Dy_{30}Cu_{20}$ alloy as the 1st step diffusion source followed by Nd-Cu diffusion as the 2nd step diffusion. The ICP-OES analysis showed that the final two-step diffusion processed HD magnet contained only 0.45 wt.% of Dy.

Measurements of the magnetic properties showed a significant enhancement of coercivity from 1.1 T (875 kA/m) to 2.5 T (1990 kA/m), while maintaining a large remanent magnetization of 1.32 T. The magnetic properties were compared to HRE and HRE-free HD Nd-Fe-B magnets and to commercially available HRE-alloyed and HRE-GBD processed sintered Nd-Fe-B magnets. The benchmark figure revealed that the magnetic properties of our two-step diffusion-processed HD magnet are close to the trend of commercially available Tb grain boundary diffusion processed sintered magnet and superior to the trend of the commercial Dy-alloyed sintered magnets. Besides, excellent magnetic properties at room temperature, the HD magnet possessed good thermal stability of coercivity (β= –0.413 %/°C), which is better than that of HRE-GBD processed sintered magnets (β= –0.5 %/°C) [174]–[177].

The microstructure characterization after the 1st step diffusion of $Nd_{50}Dy_{30}Cu_{20}$ revealed the formation of the Dy-rich layer at the grain surface and thick (H)RE-rich intergranular phases at the surface of the bulk magnet, which was attributed to the high coercivity [177]. In the 2nd step the diffusion of Nd-Cu not only made a more uniform distribution of Dy, but also led to stronger exchange-decoupling of the grains by the formation of Nd-Dy-rich intergranular phase through the entire volume of the magnets. Due to the uniform microstructure, a further improvement of the coercivity and its thermal stability was reached.

In the end, this work made a significant step forward with the two-step diffusion process in terms of economic issues and showed great industrial interest.

Scripta Materialia 205 (2021) 114207

Contents lists available at ScienceDirect

Scripta Materialia

journal homepage: www.elsevier.com/locate/scriptamat

Significant coercivity enhancement of hot-deformed bulk magnets by two-step diffusion process using a minimal amount of Dy

M. Korent[a,c,e], Xin Tang[a,b,*], H. Sepehri-Amin[a], K. Hioki[d], K.Ž. Soderžnik[c], S. Kobe[c,e], T. Ohkubo[a], K. Hono[a,1]

[a] Elements Strategy Initiative Center for Magnetic Materials, National Institute for Materials Science, Tsukuba 305-0047, Japan
[b] International Center for Young Scientists, National Institute for Materials Science, Tsukuba 305-0047, Japan
[c] Jožef Stefan Institute, Department for Nanostructured Materials, Ljubljana, Slovenia
[d] Daido Corporate Research & Development Center, Daido Steel Co., Ltd., Nagoya 457-8545, Japan
[e] Jožef Stefan International Postgraduate School, Jamova cesta 39, Ljubljana, Slovenia

ARTICLE INFO

Article history:
Received 21 June 2021
Revised 10 August 2021
Accepted 10 August 2021
Available online 24 August 2021

Keywords:
Permanent magnet
Hot-deformed magnets
Nd-Fe-B
Coercivity
Remanence

ABSTRACT

This work has demonstrated that a high coercivity of 2.5 T can be achieved in a 5.6-mm-thick Nd-Fe-B anisotropic magnet by applying the two-step diffusion process using $Nd_{50}Dy_{30}Cu_{20}$ and $Nd_{80}Cu_{20}$ eutectic alloys to a Dy-free Nd-Fe-B hot-deformed magnet. This is in contrast to the fact that about 5 wt.% Dy was needed to reach this coercivity level in sintered magnets. The overall Dy concentration in the sample was determined to be only 0.45 wt.% Dy, which is about 10 % of that used in the conventional Dy-alloyed sintered magnets with a comparable coercivity. Due to the low Dy concentration, a relatively high remanence of 1.32 T is retained even after the two-step diffusion process with an excellent temperature coefficient of coercivity of −0.41 %/°C.

(Nd,Dy)-Fe-B sintered magnets are currently used in the traction motors of hybrid/electric vehicles [1,2]. The Dy is needed to maintain the coercivity of Nd-Fe-B sintered magnets at their operating temperature of ~160°C. However, limited natural resource of Dy has urged researchers to develop Dy-free or Dy-less high-coercivity Nd-Fe-B permanent magnets. One way to increase the coercivity with a minimum usage of Dy is to enrich Dy only at the regions with reduced magnetocrystalline anisotropy, i.e., grain boundaries [3,4]. Based on this concept, the heavy-rare-earth (HRE = Dy or Tb)-grain boundary diffusion (GBD) process was invented for Nd-Fe-B sintered magnets [5–7]. In this method, the surface of the magnet is coated by a HRE compound in the form of vapor, oxides, or fluorides followed by high-temperature annealing at ~900°C for a long period of time, like 10 hs. After this process, $(Nd,HRE)_2Fe_{14}B$ shell with large magnetocrystalline anisotropy forms while the core region of grains remains as $Nd_2Fe_{14}B$ [6,7]. Hence, the usage of HRE elements can be saved. However, the upper limit of coercivity for Dy-GBD processed Nd-Fe-B sintered magnets was reported to be ~2.0 T and larger coercivity can be achieved only by alloying Dy in the initial sintered magnets [8]. Hence, a large content of Dy (~ 7.7 wt. %) is still used in the Dy-diffusion processed Nd-Fe-B sintered magnets with $\mu_0 H_c$~3.0 T [8]. If one can develop a method to enhance the coercivity to ~3 T without Dy alloying to the initial sample, the usage of Dy will be further reduced.

Another approach to increase the coercivity of Nd-Fe-B based magnets is to reduce the grain size [1,3]. Anisotropic hot-deformed magnets, first developed by Lee et al. [9], consist of platelet-shaped grains with an average size of ~300 nm in width and ~100 nm in height. Owning to the ultra-fine grain size, a large coercivity of above 2.5 T was expected; however, the maximum coercivity reported in the anisotropic hot-deformed Nd-Fe-B magnets was ~1.8 T [10]. Liu et al. showed this low coercivity was attributed to the strong intergranular exchange coupling due to the large amount of Fe in the intergranular phase [10,11]. Sepehri-Amin et al. reported a large coercivity of 2.3 T in the anisotropic hot-deformed Nd-Fe-B magnets infiltrated with a low-melting-point $Nd_{70}Cu_{30}$ eutectic alloy [12]. Thereafter, various diffusion sources have been tried to improve the coercivity to as large as ~2.5 T [13]. Sepehri-Amin et al. and Liu et al. [14,15] reported that the coercivity can be further increased to 2.6 T and 2.75 T if Dy is alloyed with NdCu and NdAl eutectic alloys for the diffusion source. This method not only

* Corresponding author.
E-mail address: TANG.Xin@nims.go.jp (X. Tang).

[1] Kazuhiro Hono was an Editor of the journal during the review period of the article. To avoid a conflict of interest, Kazuhiro Hono was blinded to the record and another editor processed this manuscript.

https://doi.org/10.1016/j.scriptamat.2021.114207
1359-6462/

modifies the chemistry of the intergranular phase but also introduces $(Nd,Dy)_2Fe_{14}B$ shell at the outer surface of platelet-shaped $Nd_2Fe_{14}B$ grains [15]. Note that the conventional HRE GBD process developed for sintered magnets cannot be applied to the hot-deformed magnets because substantial grain coarsening occurs at the processing temperature as high as 900°C for the GBD process. Hence, the eutectic diffusion process is the only way to localize the HRE at GBs in hot-deformed magnets.

Until recently, all these large coercivities were realized only in rather small samples with ~2 mm in thickness while a larger thickness above 5 mm is needed for practical applications. In order to overcome this limitation, Tang et al. have demonstrated the two-step diffusion process, which includes the diffusion of Nd-HRE-Cu and the subsequent Nd-Cu diffusion process [16]. They reported a large coercivity of 2.43 T with a remanent magnetization of 1.3 T in 5.6-mm-thick bulk hot-deformed magnets [16]. However, they used a Nd-(Tb,Dy)-Cu diffusion source for the first step and the final magnet contained 1.38 wt.%Tb and 1.06 wt.% Dy [16]. Since Tb is rather expensive element, it is strongly desired to achieve a high coercivity only with a minimum usage of Dy. In this study, we further exploited the potential of the two-step diffusion process and demonstrated that 2.5 T coercivity can be achieved with a minimum usage of 0.45 wt. % Dy with the remanent magnetization of 1.32 T and excellent temperature coefficient of coercivity of −0.41 %/°C.

The two-step eutectic alloy grain boundary diffusion process was applied to the hot-deformed (HD) magnet with a nominal composition of $Fe_{77.26}Pr_{3.06}Nd_{9.45}Co_{3.82}Ga_{0.46}B_{5.95}$ (at. %) with a dimension of 7 × 7 × 5.6 (*c*-axis) mm^3. $Nd_{50}Dy_{30}Cu_{20}$ (at. %) and $Nd_{80}Cu_{20}$ (at. %) alloy powders were prepared by the melt-spinning technique, and they were subsequently ground into powders with a particle size of ~100-300 μm. The powders were uniformly pasted on all six surfaces of the HD magnet using a polymer based glue and wrapped into a tantalum foil. The melting points of $Nd_{50}Dy_{30}Cu_{20}$ and $Nd_{80}Cu_{20}$ alloys were measured using DTA-TG to be 634°C and 512°C, respectively. Here, we optimized the diffusion temperature of the 1st step diffusion process. As shown in Fig. S1, the 1st step diffusion process at 800°C for 1.5 h resulted in the largest coercivity. Hence, we selected this as the optimum diffusion process condition for the 1st step. The 1st step diffusion process is carried out in a vacuum and 100 μm from the sample surface was polished to remove the remaining infiltration source after finishing the process. Thereafter, all six surfaces of the sample were again covered by 4 wt.% of $Nd_{80}Cu_{20}$ eutectic alloy, followed by annealing at 650°C for 9 h in vacuum. After the 2nd step annealing, a 100 μm of sample surface was also polished to remove the residual $Nd_{80}Cu_{20}$. The magnetic measurements were carried out using a BH-tracer after pre-magnetizing the sample at 5 T. A superconducting quantum interference device vibrating sample magnetometer (SQUID-VSM) was used to determine temperature-dependent coercivities. The overall microstructure was studied by scanning electron microscope (SEM, Carl Zeiss CrossBeam 1540 ESB). A more detailed microstructure investigation was carried out using aberration-corrected transmission electron microscopy (TEM, Titan G2 80-200).

Fig. 1(a) shows the demagnetization curves of the as hot-deformed and eutectic diffusion-processed samples – $Nd_{50}Dy_{30}Cu_{20}$ processed in the 1st step and $Nd_{80}Cu_{20}$ processed in the 2nd step. After the 1st step diffusion process, μ_0H_c of the sample is enhanced from 1.13 T to 2.27 T and remanent magnetization is decreased from 1.50 to 1.36 T. The squareness factor Q of the demagnetization curves, which is defined as μ_0H_k/μ_0H_c, where μ_0H_k is the external field value corresponding to the location of the knee point in the demagnetization curve at 90 % of μ_0M_r, deteriorates after the 1st step of the diffusion process from 98 % to 83 %. The poor squareness is a consequence of the non-uniform distribution of the intergranular phase in the sample from the surface toward the center as shown in Fig. S2. After the 2nd step diffusion using $Nd_{80}Cu_{20}$, the squareness factor is substantially enhanced from 83 % to 92 %. μ_0H_c is also further increased to 2.50 T with a slight decrease of remanent magnetization (μ_0M_r=1.32 T).

Fig. 1(b) shows the temperature dependence of μ_0H_c of as-deformed and eutectic diffusion processed samples. The temperature dependence of μ_0H_c is characterized by a temperature coefficient of coercivity (β), which is defined as $\Delta H_c/H_c\Delta T$ in the range of 27-227°C. After the two-step diffusion process, β was improved from −0.470 %/°C to −0.413%/°C. The thermal stability of μ_0H_c of the diffusion processed sample is not as good as that of the Nd-Tb-Cu diffusion processed HD magnet (β = −0.33 %/°C) reported by Li et al. [13], because the initial magnet in the present study is a commercial HD magnet that contains a slight amount of Pr in the initial composition, which substitutes for Nd and consequently deteriorates the thermal stability of μ_0H_c in the Nd-Fe-B magnets [17].

Fig. 2(a–c) shows low-magnification backscattered (BSE) SEM images of as-deformed sample, surface and center of the two-step diffusion processed sample, respectively. The areal fraction of the intergranular phase was calculated based on the bright contrast in the SEM images. The areal fraction of the RE-rich phase increases from 0.82 % for as-deformed sample to 18.5 % near the surface and 10.4 % in the center of the two-step diffusion processed sample. The Dy-rich shells are clearly observed in the high magnification BSE-SEM image near the surface of the sample in Fig. 2(e); how-

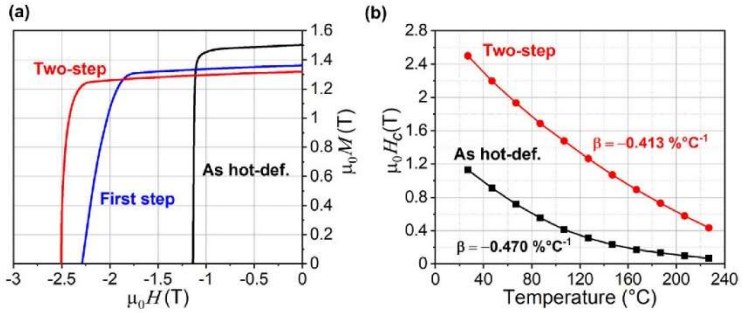

Fig. 1. (a) Demagnetization curves and (b) temperature dependences of coercivities of HD and diffusion-processed HD magnets.

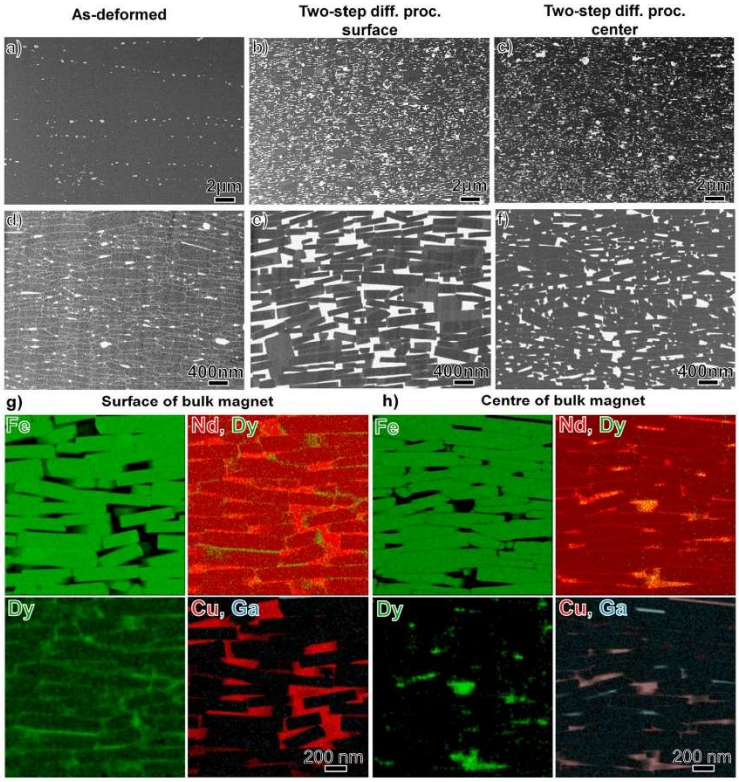

Fig. 2. Low and high magnification BSE-SEM image of (a and d) as-deformed magnet, (b and e) surface region and (c and f) center region of two-step diffusion processed magnet; cross-sectional EDS STEM maps of Fe, Nd | Dy, Dy, Cu - Ga obtained at the surface (g) and center (h) of two-step diffusion processed HD magnet.

ever, it is not discernible in the center region of the two-step diffusion processed sample as shown in Fig. 2(f). Fig. 2(g–h) show energy-dispersive X-ray spectroscopy (EDS) STEM maps observed near the surface and the center of the two-step diffusion processed sample, respectively. STEM-EDS maps near the surface of the sample (Fig. 2(g)) show the formation of thick intergranular phase, which is depleted from Fe and enriched with Nd and Cu. A Dy-rich layer is formed either on the *c*-plane surface or along the side plane surface. In contrast, toward the magnet center, the thickness of the Nd-rich intergranular phase becomes thinner as compared to the surface region. Instead of the formation of a Dy-rich shell in the grains, the Dy appears to be within the intergranular phase in the center of the two-step diffusion processed magnet. As a consequence, no Dy-rich shell is visible in the center region of the magnet. The thick *c*-plane RE-rich intergranular phase has formed near the surface region of the samples as shown in Fig. 2, indicating stronger exchange decoupling through the *c*-axis direction.

In order to determine the composition of the Dy-rich shell and thin intergranular phase from Fig. 2(e), the high-magnification STEM image and EDS maps on the surface of the bulk magnet are shown in Fig. 3(a). A ~ 10-nm-thick Dy-rich shell is visible near the intergranular phase of the two step-diffusion processed sample. Note that the formation of the Dy-rich shell is only at one side of the intergranular phase. This asymmetric feature of the HRE-rich shell formation was explained by Kim et al. based on the chemically-induced liquid film migration (CILFM) mechanism [18]. Fig. 3(b) shows high magnification of HAADF-STEM image from the center region, where only a RE-enriched intergranular phase is observed without Dy-rich shell. Detection of Dy in the center part of the magnets implies that the 2nd step diffusion by Nd-Cu delivers Dy from the surface to the center of magnets [16].

In the present work, we applied the two-step grain boundary diffusion process to a Nd-Fe-B hot-deformed magnet using $Nd_{50}Dy_{30}Cu_{20}$ alloy for the 1st step and $Nd_{80}Cu_{20}$ alloy for the 2nd step, and achieved a coercivity of 2.5 T while maintaining a relatively large remanent magnetization of 1.32 T. The overall Dy concentration in the magnet was measured to be 0.45 wt. % Dy, which is substantially lower than that for commercial sintered magnets with Dy alloying. Fig. 4 shows the remanent magnetization, $\mu_0 M_r$ versus coercivity, $\mu_0 H_c$ of Dy-free, HRE free diffusion processed [19,20], Dy-alloyed [21] and two-step diffusion processed (Tb and Dy) HD magnet. For comparison, the magnetic properties of commercially available Dy-alloyed sintered magnets and Tb diffusion processed sintered magnets are also included in Fig. 4. The properties of the Dy-diffusion processed magnet in this work are close to the trend of Tb-diffusion processed sintered magnets and su-

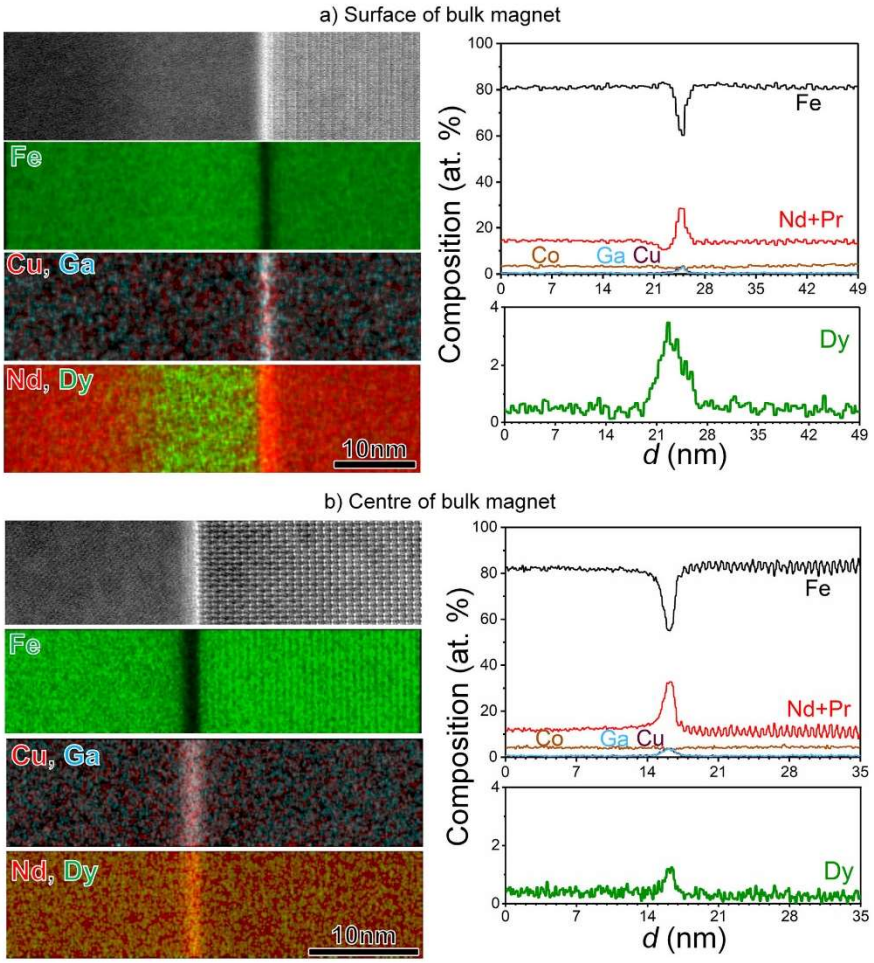

Fig. 3. High magnification STEM images and STEM-EDS maps of Fe, Cu, Ga, Nd, Dy of two-step diffusion processed HD magnet and their compositional profiles from Nd-Fe-B core to the intergranular phase in the (a) surface region and (b) centre region.

perior to that of 5 wt.% Dy-containing commercial sintered magnets, Substantial reduction of the Dy usage from 5-6 wt.% to 0.45 wt.% is of a great economic impact of the two-step diffusion processed magnet ignoring the process cost. Moreover, owning to the ultra-fine grain size of the hot-deformed magnets in this work, dilution of magnetism of the intergranular phase by the dissolution of Dy, which antiferromagnetically couples with Fe, and the formation of Dy-rich shell, a good thermal stability of $\mu_0 H_c$ (β = −0.413 %/°C) [23,24] is achieved, which is superior to that of HRE-GBD processed sintered magnets (β = −0.5 %/°C) [25,26]. As shown in Fig. 4, a Dy-containing hot-deformed magnet can have similar properties to the sample demonstrated in this work but with a much larger Dy content (above 3wt.% of Dy). The formation of the Dy-rich shell with thick RE-rich intergranular phases near the surface region is attributed to the high coercivity [16] after the 1st step diffusion using the $Nd_{50}Dy_{30}Cu_{20}$ alloy. In the 2nd step diffusion, the infiltration of $Nd_{80}Cu_{20}$ not only makes the distribution of Dy more uniform but also leads to stronger exchange-decoupling of grains by the formation of Dy- and Nd-enriched intergranular phase through the entire volume of magnets. This further improved the coercivity and its thermal stability.

In this study, we performed a two-step grain boundary diffusion process on thick (5.6 mm) hot-deformed Nd-Fe-B magnets using $Nd_{50}Dy_{30}Cu_{20}$ eutectic alloy as a diffusion source for the 1st step and $Nd_{80}Cu_{20}$ for the 2nd step. A coercivity of 2.50 T, which has never been achieved by the conventional GBD process applied to Dy-free Nd-Fe-B sintered magnets, was achieved without alloying Dy in the starting sample. The overall Dy concentration in the sam-

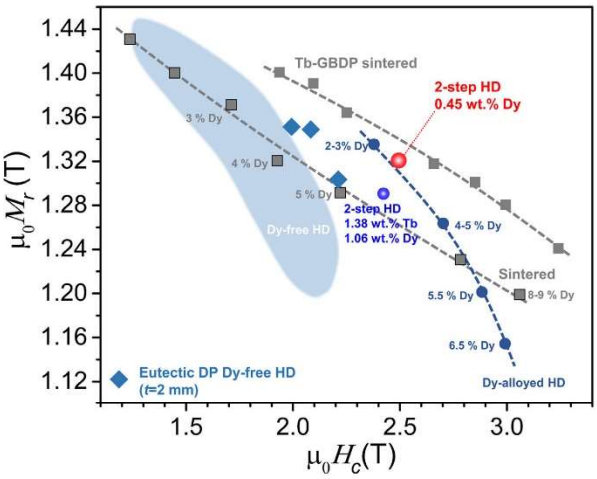

Fig. 4. Benchmark of $\mu_0 H_c$ and $\mu_0 M_r$ measured at RT including Dy-free, HRE free diffusion processed [19–20], Dy-alloyed [21] and two-step diffusion processed (Tb and Dy) HD magnets. For comparison, the properties of Tb GBDP [22] and Dy-alloyed sintered magnets are also included.

ple was measured to be 0.45 wt.% Dy, substantially lower than ~ 5 wt.% Dy for sintered magnets and above 3 wt.% for a Dy-alloyed hot-deformed magnet with the same coercivity level [21]. Because of the small amount of Dy, a relatively high remanent magnetization of 1.32 T was achieved. Moreover, the thermal stability of coercivity (β) was improved to −0.413 %/°C, which is superior to that of Dy GBD processed sintered magnets (~ −0.5 %/°C [25,26]). This work demonstrated 2.5 T class coercivity can be achieved by the 2step diffusion process using a small amount of Dy without alloying Dy in the starting material.

Declaration of Competing Interest

The authors declare that they have no known competing financial interests or personal relationships that could have appeared to influence the work reported in this paper.

Acknowledgement

This work was supported by the Elements Strategy Initiative Center for Magnetic Materials (ESICMM) of MEXT (Grant Number 12016013), through the Ministry of Education, Culture, Sports, Science, and Technology (MEXT) and in-part supported by projects ID PR-08336 and P2-0084, of the Slovenian Research Agency. Xin Tang acknowledges ICYS for the provision of ICYS fellowship.

Supplementary materials

Supplementary material associated with this article can be found, in the online version, at doi:10.1016/j.scriptamat.2021.114207.

References

[1] K. Hono, H. Sepehri-Amin, Scr. Mater. 67 (2012) 530–535.
[2] O. Gutfleisch, M.A. Willard, E. Brück, C.H. Chen, S.G. Sankar, J.P. Liu, Adv. Mater. 23 (2011) 821–842.
[3] J. Li, H. Sepehri-Amin, T. Sasaki, T. Ohkubo, K. Hono, Sci. Technol. Adv. Mater. 22 (2021) 386–403.
[4] S. Hirosawa, K. Tokuhara, Y. Matsuura, S. Fujimura, M. Sagawa, J. Magn. Magn. Mater. 61 (1986) 363–369.
[5] K.T. Park, K. Hiraga, M. Sagawa, in: Proc. 16th Int. Work. Rare-Earth Perm. Magnets Their Appl., Sendai, Japan, 2000, pp. 264–267.
[6] H. Nakamura, K. Hirota, T. Minowa, M. Honshima, INTERMAG ASIA 2005 Dig. IEEE Int. Magn. Conf. 41 (2005) 476.
[7] K. Hirota, H. Nakamura, T. Minowa, M. Honshima, IEEE Trans. Magn. 42 (2006) 2909–2911.
[8] T.H. Kim, T.T. Sasaki, T. Ohkubo, Y. Takada, A. Kato, Y. Kaneko, K. Hono, Acta Mater. 172 (2019) 139–149.
[9] R.W. Lee, Appl. Phys. Lett. 46 (1985) 790–791.
[10] J. Liu, H. Sepehri-Amin, T. Ohkubo, K. Hioki, A. Hattori, T. Schrefl, K. Hono, Acta Mater. 61 (2013) 5387–5399.
[11] A. Sakuma, T. Suzuki, T. Furuuchi, T. Shima, K. Hono, Appl. Phys. Express 9 (2016) 013002-1013002-4.
[12] H. Sepehri-Amin, T. Ohkubo, S. Nagashima, M. Yano, T. Shoji, A. Kato, T. Schrefl, K. Hono, Acta Mater. 61 (2013) 6622–6634.
[13] J. Li, L. Liu, H. Sepehri Amin, X. Tang, T. Ohkubo, N. Sakuma, T. Shoji, A. Kato, T. Schrefl, K. Hono, Acta Mater. 161 (2018) 171–181.
[14] H. Sepehri Amin, J. Liu, T. Ohkubo, K. Hioki, A. Hattori, K. Hono, Scr. Mater. 69 (2013) 647–650.
[15] L. Liu, H. Sepehri-Amin, T. Ohkubo, M. Yano, A. Kato, N. Sakuma, T. Shoji, K. Hono, Scr. Mater. 129 (2017) 44–47.
[16] X. Tang, J. Li, H. Sepehri-Amin, T. Ohkubo, K. Hioki, A. Hattori, K. Hono, Acta Mater. 203 (2021) 116479.
[17] H. Sepehri-Amin, L. Liu, T. Ohkubo, M. Yano, T. Shoji, A. Kato, T. Schrefl, K. Hono, Acta Mater. 99 (2015) 297–306.
[18] T.H. Kim, T.T. Sasaki, T. Koyama, Y. Fujikawa, M. Miwa, Y. Enokido, T. Ohkubo, K. Hono, Scr. Mater. 178 (2020) 433–437.
[19] X. Tang, J. Li, Y. Miyazaki, H. Sepehri Amin, T. Ohkubo, T. Schrefl, K. Hono, Acta Mater. 183 (2020) 408–417.
[20] L. Liu, H. Sepehri-Amin, T.T. Sasaki, T. Ohkubo, M. Yano, N. Sakuma, A. Kato, T. Shoji, K. Hono, AIP Adv. 8 (2018) 056205.
[21] K. Hioki, Sci. Technol. Adv. Mater. 22 (2021) 72–84.
[22] http://www.shinetsu rare earth magnet.jp/e/products/data_nd.html.
[23] J. Li, X. Tang, H. Sepehri-Amin, T. Ohkubo, K. Hioki, A. Hattori, K. Hono, Acta Mater. 199 (2020) 288–296.
[24] X. Tang, S.Y. Song, J. Li, H. Sepehri-Amin, T. Ohkubo, K. Hono, Acta Mater. 190 (2020) 8–15.
[25] W. Tang, K.W. Dennis, M.J. Kramer, I.E. Anderson, R.W. McCallum, J. Appl. Phys. 111 (2012) 1–4.
[26] F. Chen, L. Zhang, Y. Jin, Y. Cheng, Mater. Charact. 144 (2018) 547–553.

Supplementary data

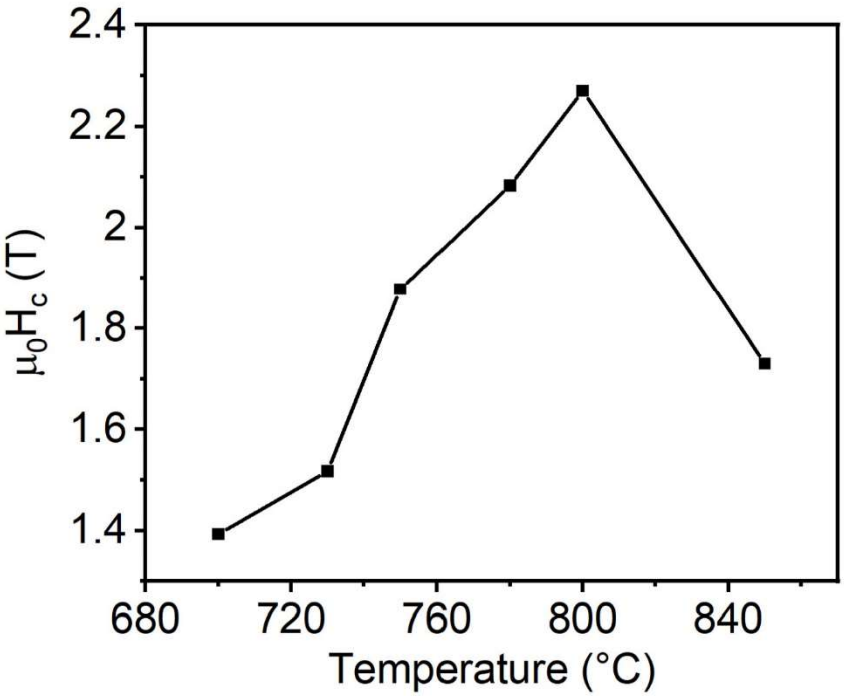

Fig. S1. The coercivity dependence of the 1st step diffusion process temperature.

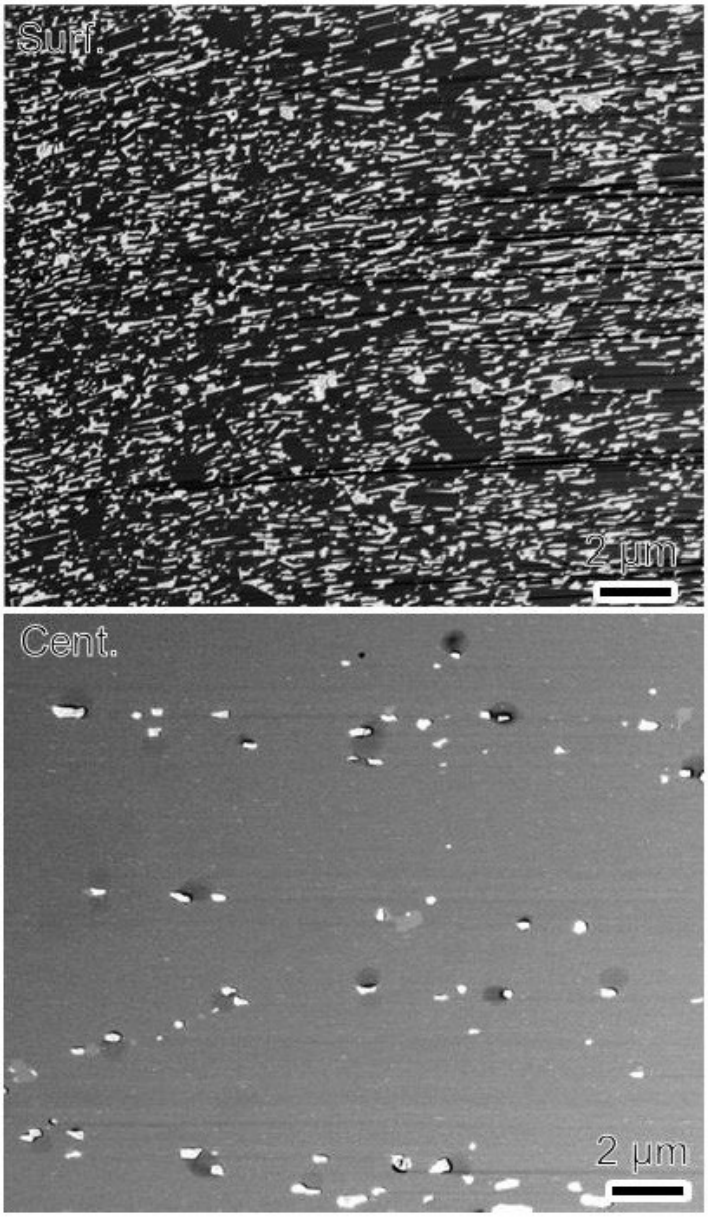

Fig. S2. The SEM figures of distribution of the intergranular phase in the sample from the surface toward the center.

4.4 A Process for Improving the Magnetic Properties of Commercial Nd-Fe-B Magnetic Ribbons with a Small Proportion of Intergranular Phase and a Process for Producing Polymer-Bonded Magnets from These Melt-Spun Ribbons

In this section, an invention that relates to the improvement of the magnetic properties (coercivity) of a commercial magnetic melt-spun Nd-Fe-B ribbons with a small intergranular phase fraction and a process for the production of polymer-bonded magnets by diffusion of a low-temperature eutectic alloy (Nd-Cu) is presented. The coercivity of the commercial Nd-Fe-B powder is not satisfactory for certain applications, while commercial powders for the fabrication of polymer-bonded magnets with high coercivity are significantly more expensive due to the added HRE. This invention presented an improvement of the magnetic properties (coercivity) of economically more favourable melt-spun Nd-Fe-B ribbons with a very small proportion of intergranular phase. The solution for coercivity enhancement was the diffusion of the low-temperature eutectic alloy (Nd-Cu), which resulted in a 15 % coercivity improvement of the final polymer-bonded magnet compared to that prepared from a standard, low-cost magnetic melt-spun Nd-Fe-B ribbons [168].

4.4.1 Selection of material for GBD processing

Usually, the initial selection of the material for the GBDP of sintered Nd-Fe-B magnets is a HRE element (Tb or Dy), due to the significant improvement of the coercivity via diffusion processing. However, in the case of working with melt-spun Nd-Fe-B ribbons, the HRE-GBDP is not an appropriate approach for coercivity enhancement. Soderžnik et al. [118] explained the backwards of the HRE-GBDP of melt-spun Nd-Fe-B powder. There, the GBDP was initiated by electrophoretic deposition (EPD) with different amounts of DyF_3 on the melt-spun Nd-Fe-B ribbons.

The coercivities of the melt-spun Nd-Fe-B ribbons ($Nd_{30.1}Pr_{0.4}Fe_{62.0}Co_{6.1}Ga_{0.5}B_{0.9}$) (wt.%) with the addition of various amounts of DyF_3 heat-treated at 650 °C for different times are shown in Figure 4.1. From the chart, the highest coercivity enhancement from 2.03 T (1615 kA/m) to 2.19 T (1742 kA/m) was achieved by the addition of 0.5 wt.% of DyF_3 and heat treatment at 650 °C for 60 min in vacuum. Besides, with the addition of a higher amount of DyF_3 the coercivity enhancement was lower, which was already observed by Žagar et al., who proved that a larger addition of HRE does not necessarily provide a higher $\mu_0 H_c$ [178]. They found that the drop of $\mu_0 H_c$ is related to the formation of NdF_3, which negatively affects the diffusion along the grain boundaries and the substitution of Dy for Nd in the $Nd_2Fe_{14}B$ matrix phase. To understand how the microstructural feature is related to the magnetic properties of improved melt-spun Nd-Fe-B powder with the addition of DyF_3 and heat treated at 650 °C for 60 min, a detailed microstructural analysis was performed [118].

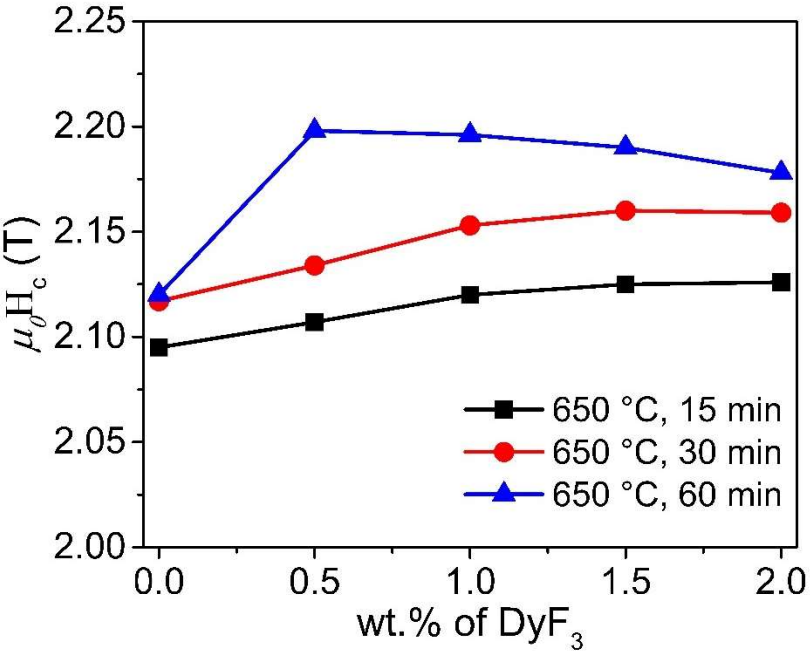

Figure 4.1: Coercivity dependence on the amount of DyF_3 and heat-treatment time [118].

Figure 4.2 (a) shows bright-field transmission electron microscopy (BF-TEM) image of TEM lamella, (b) region with single $Nd_2Fe_{14}B$ grain where the EDS analysis was performed, and (c) corresponding qualitative EDS line scan analysis. The latter showed the increased concentration of Dy at the surface layer of the $Nd_2Fe_{14}B$ matrix grain, which implies the formation of Dy-shell with a large magnetocrystalline anisotropy [140]. The thickness of the Dy-rich shell, detected by EDS analysis, was, however, rather small ~ 4 nm [118]. After the diffusion of Dy from the surface toward the center along the GBs, there were two possible mechanisms for the formation of the Dy-rich shell at the surface layer of $Nd_2Fe_{14}B$ matrix grain – either by the exchange of Nd for Dy below the melting point of the ternary eutectic temperature (~ 685 °C) or by cooling from the melting point of the ternary eutectic temperature [150], [151], [179].

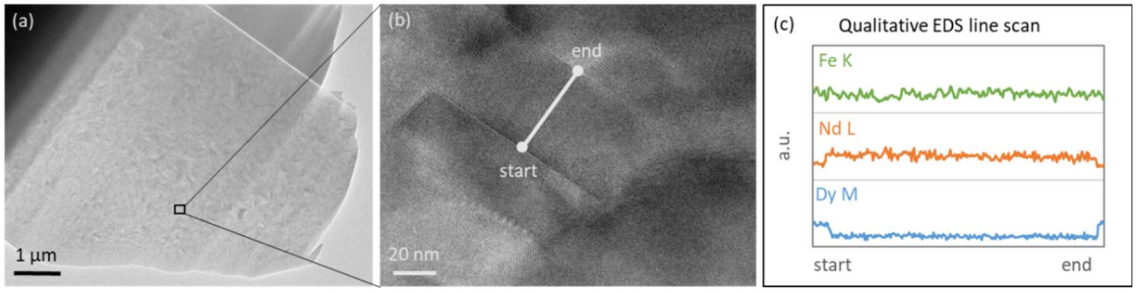

Figure 4.2: (a) BF-TEM image of GBDP melt-spun Nd-Fe-B powder with the addition of DyF_3, (b) region with single $Nd_2Fe_{14}B$ grain, showing where the EDS line scan analysis was performed, and (c) chart with qualitative EDS line scan [118].

To answer the question about the efficiency of the GBDP, the thickness of the GBs of sintered Nd-Fe-B magnets (Figure 4.3 (a),(b)) was compared with the thickness of the GBs of melt-spun Nd-Fe-B ribbons (Figure 4.3 (c),(d)). From the image, it can be seen as a

rather thick Nd-rich GB phase in sintered Nd-Fe-B magnet, while thin and dry GBs were found in melt-spun Nd-Fe-B powder. Straumal et al. [180] studied the phenomena of the wetting and contact angle, which are modified with the addition of DyF_3 in the GBs. Especially, GB wetting appeared to be a pseudopartial type after the addition of Dy [181]. In the end, our microstructural characterizations suggested that for an effective diffusion process and reaching high coercivities via Dy-rich shell formation, a sufficient GB phase should be present in the structure. Consequently, the commercial melt-spun Nd-Fe-B ribbons cannot fully utilize the potential of HRE-GBDP, due to their microstructural limiting factors – thin and dry GBs [118].

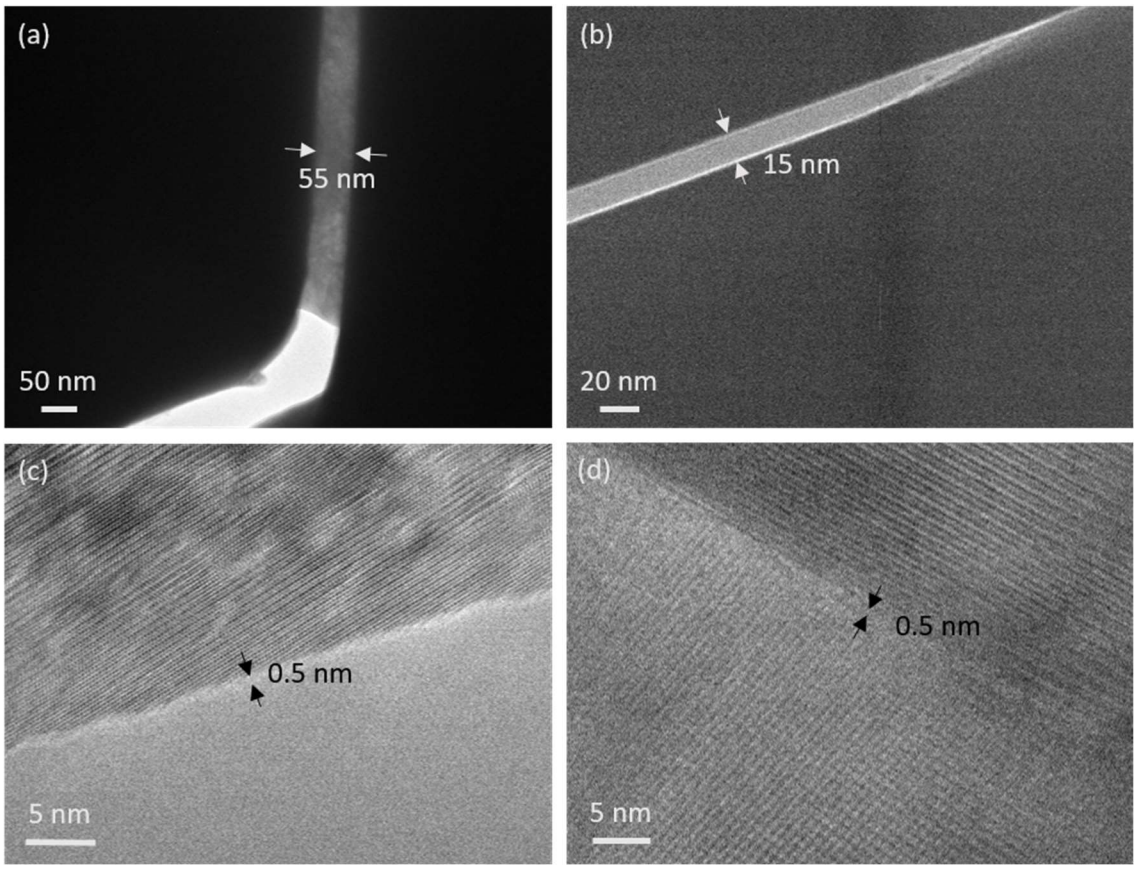

Figure 4.3: BF-TEM images with labelled grain-boundary thickness of (a) and (b)GBDP sintered Nd-Fe-B magnet with the addition of DyF_3 and, (c) and (d) GBDP melt-spun Nd-Fe-B ribbons with the addition of DyF_3 [118].

The thin and dry GBs of melt-spun are not the only reason not to choose the HRE-GBDP in our invention. This method is well developed in the field of commercial sintered Nd-Fe-B magnets. However, as mentioned in the Introduction, the conventional HRE-GBDP [128], [130] is hard to apply in the case of the melt-spun Nd-Fe-B ribbons since high-temperature annealing (above 900 °C) is required, which results in substantial grain growth of ultrafine-grained melt-spun powder and consequently deterioration of magnetic properties [114], [136]. Figure 4.4 shows the demagnetization curves of melt-spun Nd-Fe-B ribbons with the addition of 2 wt.% of DyF_3 heat-treated at 650 °C and 700 °C for 60 min in vacuum. It can be seen that the deterioration of coercivity at 700 °C, which implies that already this temperature was the edge temperature for diffusion processing of melt-spun Nd-Fe-B ribbons with this composition.

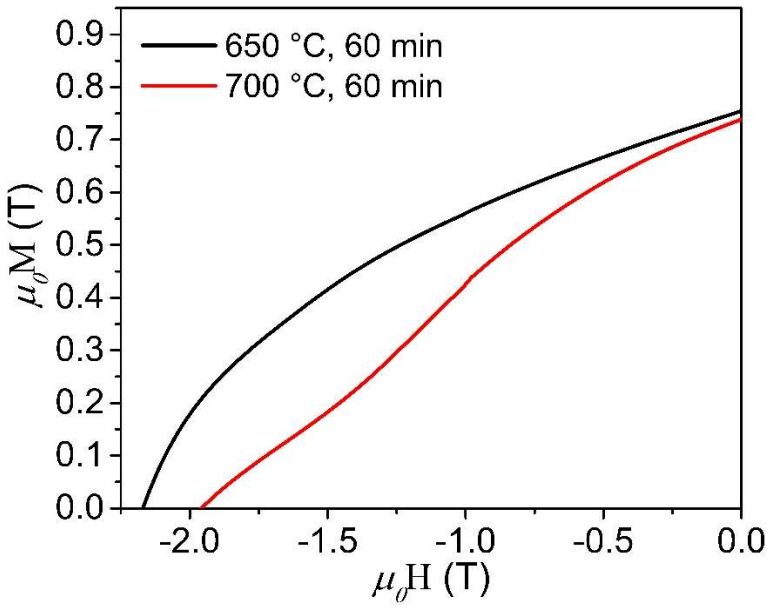

Figure 4.4: Demagnetization curves of melt-spun Nd-Fe-B ribbons with the addition of 2 wt.% of DyF_3 heat-treated at 650 °C and 700 °C for 60 min in vacuum.

Even though we used in our invention melt-spun Nd-Fe-B ribbons with a different composition, the temperatures used for conventional HRE-GBDP are still too high. That is why another way to enhance the room-temperature coercivity had to be found. To bypass the grain coarsening, Sepehri-Amin et al. presented a solution with the engineering of GB phase by low-temperature GBDP in HD Nd-Fe-B magnets that were developed to improve the coercivity of HDDR powder [135], [163]. He used low-temperature eutectic alloy (Nd-Cu) without HRE in order to form a non-ferromagnetic phase in GBs and increase the coercivity without inducing grain coarsening [39], [163]. Based on the above-mentioned reasons, in this work, we decided to use low-temperature GBDP to increase the coercivity of commercial melt-spun Nd-Fe-B ribbons. The non-ferromagnetic alloy used for the diffusion process was Nd-Cu, with eutectic composition $Nd_{70}Cu_{30}$ (at.%) and melting temperature 520 °C [167].

4.4.2 Magnetic properties of improved melt-spun Nd-Fe-B powder and final polymer-bonded magnets

Based on the coercivity improvement of melt-spun Nd-Fe-B ribbons and economically efficient diffusion processing, we determined the processing time of 30 min and selected between three different temperatures shown in Figure 4.5. The graph shows that 700 °C was the most appropriate temperature for diffusion processing because even for the small addition of Nd-Cu alloy (3 wt.%), the coercivity is enhanced by almost 14 % [168].

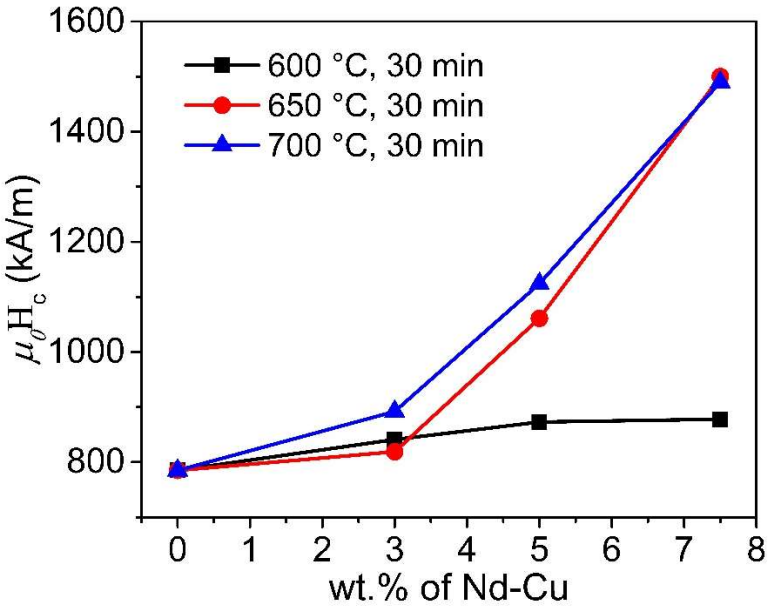

Figure 4.5: Coercivity dependence on the amount of Nd-Cu and heat-treatment temperature.

Figure 4.6 shows a comparison of the demagnetization curves of commercial melt-spun Nd-Fe-B ribbons with nominal composition $Nd_{26.4}Fe_{67.6}Co_{5.0}B_{1.0}$ (wt.%) and of commercial melt-spun Nd-Fe-B ribbons with the addition of various amounts of $Nd_{70}Cu_{30}$ eutectic alloy diffusion processed at 700 °C for 30 min in vacuum. The shape of the demagnetization proves that during the processing a reaction and the formation of a new phase occurred. There are two different phases present, after the diffusion process confirmed by the knee or bend in the demagnetization curve, which was already reported in many previous studies [182]–[184]. The highest coercivity, close to 1500 kA/m (1.88 T), was achieved by the addition of 7.5 wt.% of Nd-Cu alloy. However, this coercivity enhancement is achieved at the expense of remanence. In the case of the addition of 7.5 wt.% of Nd-Cu, the remanence decrease by 17 % due to the infiltration of the non-ferromagnetic phase (Nd-Cu) into the system and consequently an increase of the volume fraction of the non-ferromagnetic phase, which leads to the dilution of ferromagnetic phase [103], [159], [185]. To minimize the reduction of remanence, the volume fraction of the non-ferromagnetic intergranular phase was optimized. In the end, we choose the addition of 3 wt.% of Nd-Cu for further processing of polymer-bonded magnets. In this case, the coercivity increased by almost 14 %, meanwhile, the remanence decreased by less than 6 % [168].

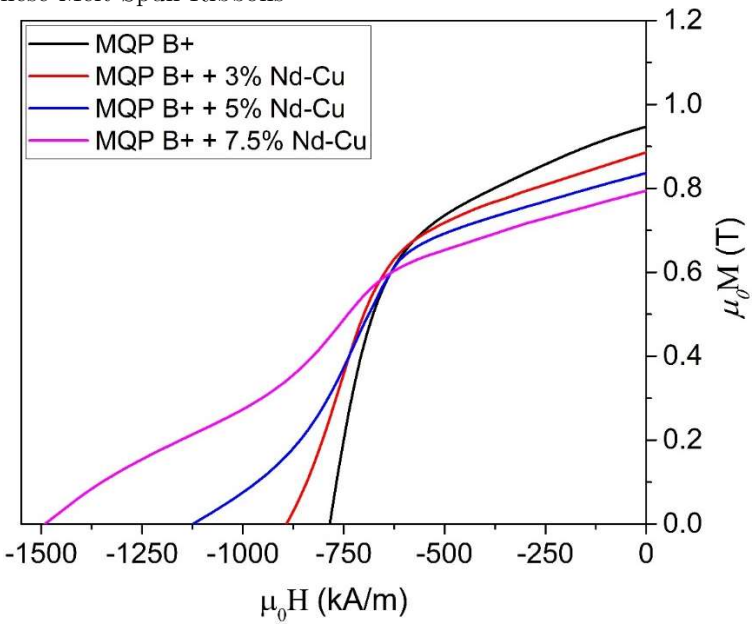

Figure 4.6: Demagnetization curves of melt-spun Nd-Fe-B ribbons and melt-spun Nd-Fe-B ribbons with the addition of various amounts of $Nd_{70}Cu_{30}$ eutectic alloy diffusion processed at 700 °C for 30 min in vacuum [168].

Figure 4.7 shows demagnetization curves of the Nd-Fe-B polymer-bonded magnet and of Nd-Fe-B polymer-bonded magnets with the addition of 3 wt.% of $Nd_{70}Cu_{30}$ processed by laboratory and industrial processes. The polymer-bonded magnet prepared from the standard melt-spun powder was industry processed and shows very similar properties to one prepared in the laboratory. The coercivity of laboratory-processed improved polymer-bonded magnet was enhanced from 750 kA/m (0.95 T) to 855 kA/m (1.08 T) and the remanence decreased by only ≈ 7 % (from 0.52 T to 0.48 T). On the other hand, industry processed improved polymer-bonded magnet showed an even higher increase of coercivity from 750 kA/m (0.95 T) to 900 kA/m (1.13 T), while the remanence decreased slightly more – from 0.52 T to 0.43 T. However, the origin of the difference of magnetic properties is not in the way of processing the polymer-bonded magnet, but in the composition of the melt-spun Nd-Fe-B ribbons after diffusion processing, which is not homogeneous anymore. Due to the different particle sizes of melt-spun Nd-Fe-B ribbons and Nd-Cu powder, and uneven distribution of both powders after mixing them, the diffusion of Nd-Cu did not take place uniformly over the whole sample of melt-spun Nd-Fe-B ribbons. The result was a small fluctuation in the magnetic properties, which was not decisive, as all samples showed at least a ≈ 14 % enhancement of coercivity [168].

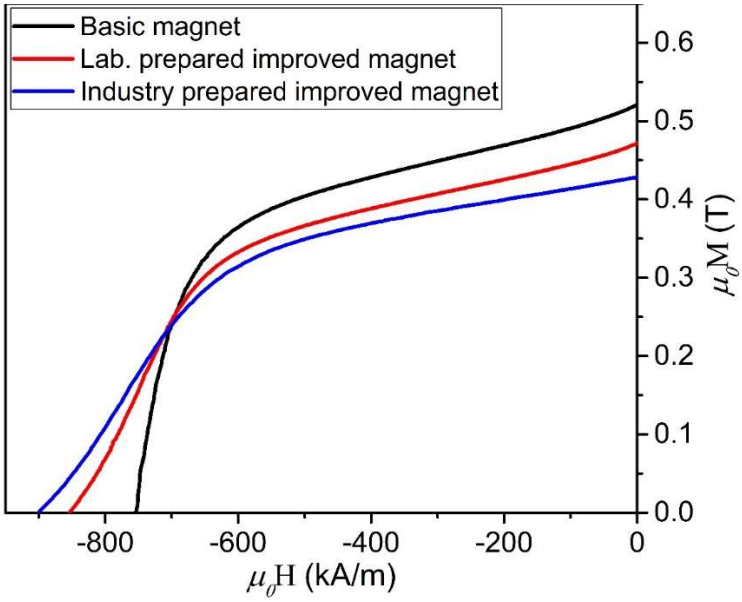

Figure 4.7: Demagnetization curves of Nd-Fe-B polymer-bonded magnet and of Nd-Fe-B polymer-bonded magnets with the addition of 3 wt.% of $Nd_{70}Cu_{30}$ processed in laboratory and in the industrial process [168].

4.4.3 Microstructure characterization of improved melt-spun Nd-Fe-B ribbons

The SEM image at low magnification was employed to check whether the diffusion processing of Nd-Cu was working properly. Figure 4.8 shows the microstructure of a 60-µm melt-spun Nd-Fe-B particle diffusion processed at 700 °C – above the melting point of $Nd_{70}Cu_{30}$ eutectic alloy (520 °C) [167]. The image proves that Nd-Cu diffusion took place during heat treatment since the Nd-Cu alloy enveloped almost half of the melt-spun Nd-Fe-B particle [168].

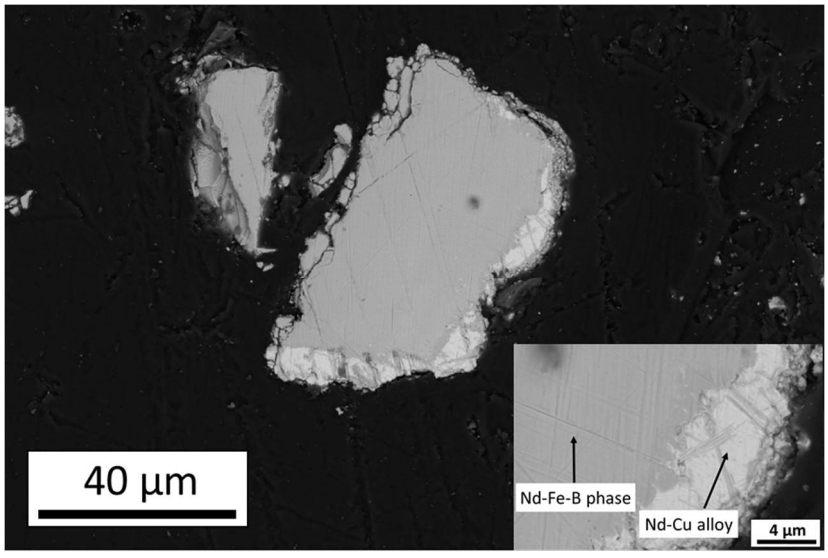

Figure 4.8: The microstructure of melt-spun Nd-Fe-B ribbons with the addition of Nd-Cu eutectic alloy [168].

Figure 4.9 shows the FIB-SEM image of the microstructure at higher magnification, where the diffusion of Nd-Cu into the interior of the particle is visible. After the diffusion process the melt-spun Nd-Fe-B particle is assembled of fine $Nd_2Fe_{14}B$ grains and large $Nd_2F_{14}B$ grains and we have two explanations for this phenomenon. Li et al. reported that the grain growth of large grains was attributed to Nd-Cu alloy which became liquid at diffusion processing temperature 700 °C [186]. During the diffusion processing, the liquid Nd-Cu alloy diffused into the melt-spun Nd-Fe-B particle along the grain boundaries and promotes the grain growth at the outer part of the particle due to higher diffusion efficiency in the liquid alloy [186]. On the other hand, the two distinct grain zones after heat treatment of melt-spun Nd-Fe-B ribbons have also been reported by Fujimoto et al. [187]. They claim that the solidification velocity during melt spinning is faster on the wheel side than on the free side, resulting in more lattice defects such as vacancies at the wheel side. During the heat treatment, such defects migrate and assist in a rapid diffusion, which promotes the faster growth of grains on the roll side [187].

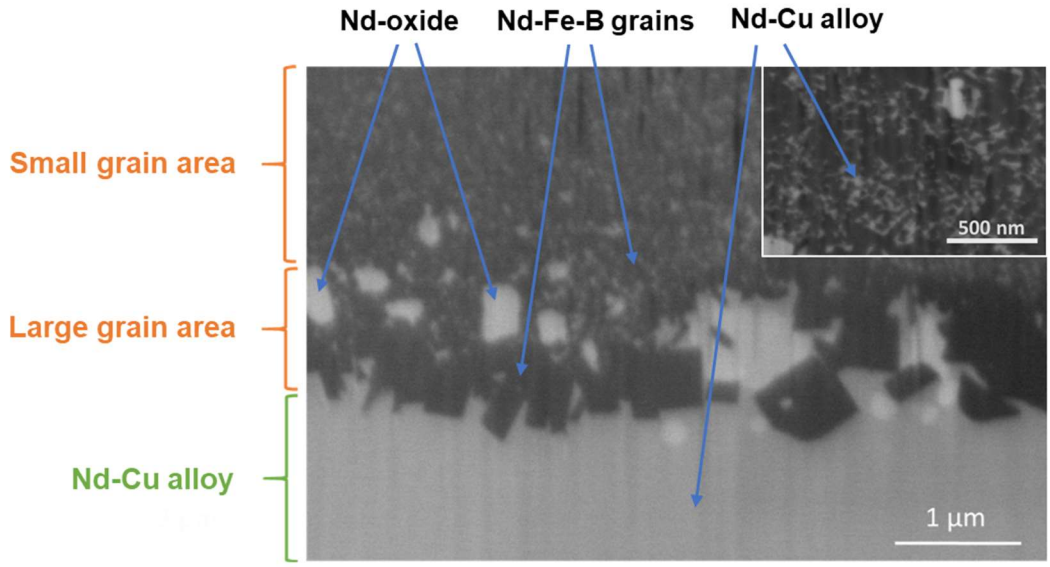

Figure 4.9: The microstructure of melt-spun Nd-Fe-B ribbons with the addition of Nd-Cu eutectic alloy at high magnification [168].

A detailed analysis of the microstructure of HD magnets prepared from melt-spun Nd-Fe-B ribbons showed that the intergranular phase is composed of more than 50 at.% of Fe and Co as pure metals, which indicates that this phase is ferromagnetic [107].

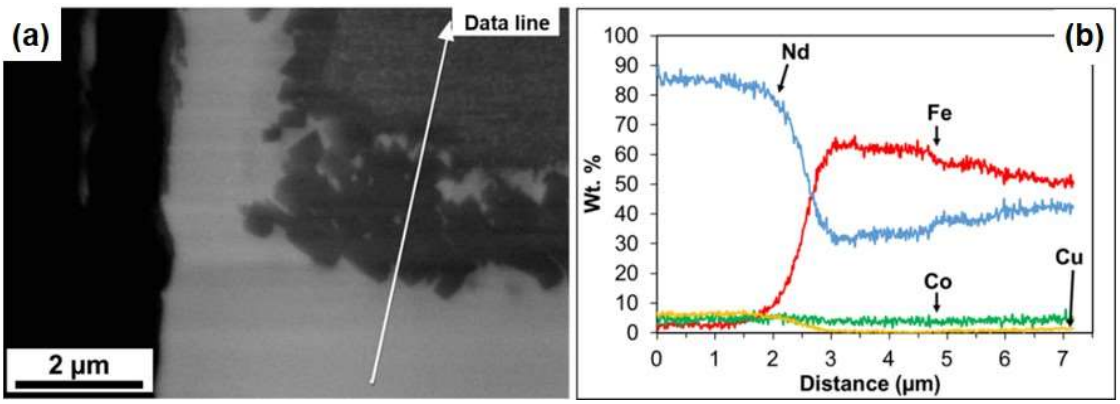

Figure 4.10: (a) The region of the microstructure of melt-spun Nd-Fe-B ribbons with the addition of Nd-Cu eutectic alloy, showing where the EDS analysis was performed, (b) corresponding qualitative EDS line scan [168].

Figure 4.10 (a) shows a FIB-SEM image of diffusion processed melt-spun Nd-Fe-B particle where the region of interest for EDS analysis (Figure 4.10 (b)) was selected. The EDS quantitative analysis showed increased concentration of Nd inside of the melt-spun Nd-Fe-B particle. This implies that the intergranular phase after the diffusion process became thicker and Nd-rich, which changed its composition and reduced the amount of ferromagnetic elements [163]. This microstructural change increased the depinning field which implies that a decreased concentration of ferromagnetic elements greatly enhanced the pinning strength of the intergranular phase and consequently increased the coercivity [163]. In other words, coercivity was effectively increased by adding a non-ferromagnetic isolation phase around the ferromagnetic grains, which weakened the intergrain exchange coupling [188].

Chapter 5

Conclusions

In this thesis, four different topics with one common point, i.e., the initial material, are individually presented. The first section shows an alternative way of producing a HD magnet with good magnetic properties using a low-pressure, unconventional, spark-plasma sintering technique, in analogy with PLP. The hot-deformed (HD) Nd-Fe-B magnets were processed from commercial melt-spun Nd-Fe-B ribbons at 680 °C under a low pressure of 40 MPa. This method enabled the production of HD magnets in a short processing time, which means that the grain growth of the HD magnet was inhibited. With moderate temperature and low pressure, a uniform non-ferromagnetic grain-boundary phase around the $Nd_2Fe_{14}B$ matrix grains was obtained. The final HD magnet with a deformation of 75 % showed a remanent magnetization of 1.29 T and a coercivity of 1077 kA/m (1.35 T) and a maximum energy product of 313 kJ/m^3, which is comparable with conventional HD methods, where high pressure and high temperature are needed. To understand the behaviour of the magnetic properties and microstructure evolution in the initial stages of the deformation process, HD magnets with different deformation ratios (23 %, 34 %, 46 %, 57 % and 75 %) were produced and their dependence of remanence on the deformation ratio was determined. The magnetic properties of HD magnets with different height reductions showed an enhancement of the remanent magnetization and deterioration of the coercivity with increasing deformation ratio. FIB BS microstructure characterization showed three different zones with a gradual texturing from the top toward the bottom in a cone-like shape HD magnet. In parallel with the experimental data, a simple Stoner-Wohlfarth model was employed to interpret the reciprocity between the positive effect of the HD process due to grain alignment and the negative impact of grain-boundary deterioration.

By continuing with HD processing, in the second section LEP (low energy processing) and HEP (high energy processing) HD magnets were processed using the same SPS technique, which is a significantly lower energy consumption technique regarding the conventional HD processing method. I investigated the microstructural and magnetic properties of LEP and HEP HD magnets and performed a detailed analytical comparison. Prior to the characterization, the post-annealing step of both HD magnets was performed to further enhance the magnetic properties. An LEP HD magnet inhibits just 0.04 T lower remanent magnetization than a HEP HD magnet (1.31 T). After post-annealing, both magnets' coercivity values are similar: 1325 kA/m (1.67 T) for the LEP HD and 1337 kA/m (1.67 T) for the HEP HD. A minor deficiency in magnetic properties in the LEP HD magnet was revealed by statistical analyses, which showed a better texture orientation for the HEP HD magnet. The results indicated a slightly lower remanent (1.27 T) magnetization and reduced squareness (77 %) for the LEP HD magnet.

In a collaboration with NIMS and Daido, I performed a recently developed two-step GBDP on thick (5.6 mm) HD Nd-Fe-B magnets. $Nd_{50}Dy_{30}Cu_{20}$ alloy as a diffusion source was used in the 1st step followed by the 2nd step of Nd-Cu diffusion. A coercivity of 2.50 T (1990 kA/m) with a remanent magnetization of 1.32 T was achieved with only the consumption of 0.45 wt.% Dy. The properties of the Dy-diffusion processed magnet in this work are close to the trend of Tb-diffusion processed sintered magnets and superior to that of commercial 5 wt.% Dy-containing commercial sintered magnets. Substantial reduction of Dy usage from 5-6 wt.% to 0.45 wt.% shows the great economic impact of a two-step diffusion process. Moreover, owing to the ultra-fine grain size of the developed HD magnets in this work, the non-ferromagnetic nature of the grain-boundary phase, and formation of Dy-rich shell, we have successfully realized the good thermal stability of coercivity (β = –0.413 %/°C), which is superior to that of HRE-GBD processed sintered magnets (β = –0.5 %/°C). The detailed microstructure analysis of two-step diffusion processed HD magnet revealed the formation of Dy-rich $(Nd_{1-x}Dy_x)_2Fe_{14}B$ grain with thick (H)RE-rich intergranular phases at the surface of the bulk magnet, which were attributed to high coercivity after the 1st step diffusion of Dy-Nd-Cu. In the 2nd step diffusion of Nd-Cu not only made a more uniform distribution of Dy but also led to stronger exchange-decoupling of grains by the formation of Dy-Nd-rich intergranular phase through the entire volume of magnets and further improving the coercivity to 2.50 T and thermal stability of coercivity (β = –0.413 %/°C). This work made the two-step diffusion process a significant step forward in terms of economic issue and showed great industrial interest.

The possibility of the coercivity improvement is not only by the GBDP in the final bulk magnet but also by the GBDP in initial melt-spun Nd-Fe-B ribbons. In collaboration with Kolektor Group d.o.o and Kolektor KFH d.o.o, an invention that relates to an improvement of the magnetic properties (coercivity) of a commercial magnetic melt-spun Nd-Fe-B powder with a small intergranular phase fraction and a process for the production of polymer-bonded magnets by GBDP of a low-temperature eutectic alloy (Nd-Cu) is presented. The coercivity of the commercial Nd-Fe-B ribbons is not satisfactory for certain applications, while commercial ribbons for the fabrication of polymer-bonded magnets with high coercivity are significantly more expensive due to the added Dy. This invention was therefore focusing on an improvement of the magnetic properties (coercivity) of a commercially significantly more favourable melt-spun Nd-Fe-B ribbons with a small proportion of intergranular phase, by low-temperature eutectic alloy (Nd-Cu) diffusion for manufacturing the polymer-bonded magnets with up to 15 % higher coercivity compared to that prepared from a standard low-cost magnetic melt-spun Nd-Fe-B ribbons. From an economic point of view, it is not only important the low processing temperature, but also the added amount of non-ferromagnetic alloy. Because it contains expensive and strategic RE elements, a more significant addition of low-temperature eutectic alloy can represent an additional cost. Therefore, the process was optimized so that the additive was as small as possible (3 wt.% of Nd-Cu alloy) with the desired coercivity improvement achieved.

References

[1] R. A. Meyers, *Encyclopedia of Physical Science and Technology. 3rd edition.*, 3rd ed. San Diego : Academic Press, ©2002, 2002.

[2] H. P. Schlemmer, "Vom magneteisenstein zum magnetresonanztomographen. Zur geschichte des magnetismus," *Radiologe*, vol. 45, no. 4, pp. 356–362, 2005, doi: 10.1007/s00117-005-1189-y.

[3] W. Gilbert, *On the loadstone and magnetic bodies, and on the great magnet the Earth*. New York: John Wiley & Sons, Inc., 1893.

[4] Karlsruhe Institute of Technology, "The invention of the electric motor 1856–1893." [Online]. Available: https://www.eti.kit.edu/english/1390.php. [Accessed: 24-May-2021].

[5] "The Electromagnet." [Online]. Available: http://physics.kenyon.edu/EarlyApparatus/Electricity/Electromagnet/Electromagnet.html. [Accessed: 24-May-2021].

[6] J. J. Stupak Jr., "Methods of Magnetizing Permanent Magnets," 2000. [Online]. Available: http://www.oersted.com/wp-content/uploads/2019/06/magnetizing.pdf. [Accessed: 24-May-2021].

[7] "Permanent magnets." [Online]. Available: https://ozank.gitbooks.io/ee361/content/magnetic_circuits/permanent_magnets.html. [Accessed: 20-May-2021].

[8] B. D. Cullity and C. D. Graham, *Introduction to Magnetic Materials*. Hoboken, NJ, USA: John Wiley & Sons, Inc., 2008.

[9] "High Quality High Performance AlNiCo Magnet." [Online]. Available: https://magnetsdm.en.made-in-china.com/product/dXtnSYQvhlhu/China-High-Quality-High-Performance-AlNiCo-Magnet.html. [Accessed: 24-May-2021].

[10] TDK, "Ferrite magnets." [Online]. Available: https://product.tdk.com/en/system/files?file=dam/doc/product/magnet/magnet/ferrite/datasheets/magnet_fb_summary_en.pdf. [Accessed: 24-May-2021].

[11] G. Hoffer and K. J. Strnat, "Magnetocrystalline Anisotropy of YCo5, and Y2Co17," *IEEE Trans. Magn.*, vol. 2, no. 3, pp. 478–489, 1966.

[12] J. fang LIU, P. Vora, and M. Walmer, "Overview of Recent Progress in Sm-Co Based Magnets," *J. Iron Steel Res. Int.*, vol. 13, no. SUPPL. 1, pp. 319–323, 2006, doi: 10.1016/S1006-706X(08)60202-2.

[13] S. Liu, "Sm-Co high-temperature permanent magnet materials," *Chinese Phys. B*, vol. 28, no. 1, 2019, doi: 10.1088/1674-1056/28/1/017501.

[14] K. M. Krishnan, *Fundamentals and Applications of Magnetic Materials*. Oxford University Press, 2016.

[15] G. Y. Chin *et al.*, "Easy Directions of Magnetization in Ternary R 2 (Co , Fe) ll 7 Phases," *Earth*, vol. 11, pp. 1971–1973, 1972.

[16] E. A. Nesbitt and J. H. Wernick, *Rare Earth Permanent Magnets*. Elsevier, 1973.

[17] J. F. Liu and M. H. Walmer, "Thermal stability and performance data for SmCo 2:17 high-temperature magnets on PPM focusing structures," *IEEE Trans. Electron Devices*, vol. 52, no. 5, pp. 899–902, 2005, doi: 10.1109/TED.2005.845868.

[18] O. Gutfleisch *et al.*, "Evolution of magnetic domain structures and coercivity in high-performance SmCo 2:17-type permanent magnets," *Acta Mater.*, vol. 54, no. 4, pp. 997–1008, 2006, doi: 10.1016/j.actamat.2005.10.026.

[19] J. J. Croat, *Rapidly solidified neodymium-iron-boron permanent magnets*. Elsevier, 2017.

[20] A. E. Clark, "High-field magnetization and coercivity of amorphous rare-earth-Fe 2 alloys," *Appl. Phys. Lett.*, vol. 23, no. 11, pp. 642–644, 1973, doi: 10.1063/1.1654777.

[21] J. J. Rhyne, J. H. Schelleng, and N. C. Koon, "Anomalous magnetization of amorphous TbFe2, GdFe2, and YFe2," *Phys. Rev. B*, vol. 10, no. 11, pp. 4672–4679, 1974, doi: 10.1103/PhysRevB.10.4672.

[22] J. J. Croat, "Preparation and coercive force of melt-spun Pr-Fe alloys," *Appl. Phys. Lett.*, vol. 37, no. 12, pp. 1096–1098, 1980, doi: 10.1063/1.91885.

[23] J. J. Croat, "Observation of large room-temperature coercivity in melt-spun Nd 0.4Fe0.6," *Appl. Phys. Lett.*, vol. 39, no. 4, pp. 357–358, 1981, doi: 10.1063/1.92728.

[24] J. J. Croat, "Magnetic hardening of Pr-Fe and Nd-Fe alloys by melt-spinning," *J. Appl. Phys.*, vol. 53, no. 4, pp. 3161–3169, 1982, doi: 10.1063/1.331014.

[25] I. Transactions and O. N. Magnetics, "Permanent Magnet Properties of Rapidly Quenched Rare Earth-Iron Alloys J. J. Croat Physics Department, General Motors Research Laboratories, Warren, MI," vol. M, no. 6, pp. 1442–1447, 1982.

[26] N. C. Koon and B. N. Das, "Magnetic properties of amorphous and crystallized (Fe0.82B 0.18)0.9Tb0.05La0.05," *Appl. Phys. Lett.*, vol. 39, no. 10, pp. 840–842, 1981, doi: 10.1063/1.92578.

[27] N. C. Koon, B. N. Das, and J. A. Geohegan, "Composition dependence of the coercive force and microstructure of crystallized amorphous (FexB1-x)0.9Tb0.05La0.05 alloys," *IEEE Trans. Magn.*, vol. 18, no. 6, pp. 1448–1450, 1982, doi: 10.1109/TMAG.1982.1061968.

[28] G. C. Hadjipanayis, R. C. Hazelton, and K. R. Lawless, "New iron-rare-earth based permanent magnet materials," *Appl. Phys. Lett.*, vol. 43, no. 8, pp. 797–799, 1983, doi: 10.1063/1.94459.

[29] G. C. Hadjipanayis, R. C. Hazelton, and K. R. Lawless, "Cobalt-free permanent magnet materials based on iron-rare-earth alloys (invited)," *J. Appl. Phys.*, vol. 55, no. 6, pp. 2073–2077, 1984, doi: 10.1063/1.333570.

[30] J. J. Croat, J. F. Herbst, R. W. Lee, and F. E. Pinkerton, "High-energy product Nd-Fe-B permanent magnets," *Appl. Phys. Lett.*, vol. 44, no. 1, pp. 148–149, 1984, doi: 10.1063/1.94584.

[31] J. J. Croat, J. F. Herbst, R. W. Lee, and F. E. Pinkerton, "Pr-Fe and Nd-Fe-based

materials: A new class of high-performance permanent magnets (invited)," *J. Appl. Phys.*, vol. 55, no. 6, pp. 2078–2082, 1984, doi: 10.1063/1.333571.

[32] M. Sagawa, S. Fujimura, N. Togawa, H. Yamamoto, and Y. Matsuura, "New material for permanent magnets on a base of Nd and Fe (invited)," *J. Appl. Phys.*, vol. 55, no. 6, pp. 2083–2087, 1984, doi: 10.1063/1.333572.

[33] D. Givord, H. S. Li, and J. M. Moreau, "Magnetic properties and crystal structure of Nd2Fe14B," *Solid State Commun.*, vol. 50, no. 6, pp. 497–499, 1984, doi: 10.1016/0038-1098(84)90315-6.

[34] J. F. Herbst, J. J. Croat, F. E. Pinkerton, and W. B. Yelon, "Relationships between crystal structure and magnetic properties in Nd2Fe14B," *Phys. Rev. B*, vol. 29, no. 7, pp. 4176–4178, 1984, doi: 10.1103/PhysRevB.29.4176.

[35] J. M. D. Coey, *Rare-earth Iron Permanent Magnets*. Oxford: Oxford University Press, 1996.

[36] S. Hirosawa, Y. Matsuura, H. Yamamoto, S. Fujimura, M. Sagawa, and H. Yamauchi, "Magnetization and magnetic anisotropy of R2Fe14B measured on single crystals," *J. Appl. Phys.*, vol. 59, no. 3, pp. 873–879, 1986, doi: 10.1063/1.336611.

[37] K. Hono and H. Sepehri-Amin, "Strategy for high-coercivity Nd-Fe-B magnets," *Scr. Mater.*, vol. 67, no. 6, pp. 530–535, 2012, doi: 10.1016/j.scriptamat.2012.06.038.

[38] T. Zhang *et al.*, "Hot-deformed Nd-Fe-B magnets fabricated by dynamic loading with a high maximum energy product," *Intermetallics*, vol. 73, pp. 67–71, 2016, doi: 10.1016/j.intermet.2016.04.001.

[39] J. Li, H. sepehri amin, T. Sasaki, T. Ohkubo, and K. Hono, "Most frequently asked questions about the coercivity of Nd-Fe-B permanent magnets," *Sci. Technol. Adv. Mater.*, 2021, doi: 10.1080/14686996.2021.1916377.

[40] J. Yamauchi, "Fundamentals of Magnetism," in *Nitroxides: Applications in Chemistry, Biomedicine, and Materials Science*, Wiley-VCH Verlag GmbH & Co. KGaA, 2008, pp. 1–45.

[41] J. M. D. Coey, "Basic Concepts in Magnetism." [Online]. Available: http://magnetism.eu/esm/2009/slides/coey-slides-2.pdf. [Accessed: 11-Aug-2021].

[42] T. Tomše, "Novel multicomponent Nd-Fe-B permanent magnets," Jožef Stefan International Postgraduate School, Jožef Stefan Institute, 2018.

[43] M. Soderžnik, "The development of an optimum core-shell microstructure for high-coercivity Nd-Fe-B magnets with minimum heavy-rare-earth content," Jožef Stefan International Postgraduate School, Jožef Stefan Institute, 2013.

[44] G. E. Uhlenbeck and S. Goudsmit, "Ersetzung der Hypothese vom unmechanischen Zwang durch eine Forderung bezüglich des inneren Verhaltens jedes einzelnen Elektrons," *Naturwissenschaften*, vol. 13, no. 47, pp. 953–954, 1925.

[45] N. A. Spaldin, *Magnetic materials: Fundamentals and applications*, vol. 9780521886697. Cambridge University Press, 2010.

[46] M. Getzlaff, *Fundamentals of magnetism*. Springer Berlin Heidelberg, 2008.

[47] J. M. D. Coey, *Magnetism and magnetic materials*, vol. 9780521816144. Cambridge University Press, 2010.

[48] C. Rudowicz and H. W. F. Sung, "Textbook treatments of the hysteresis loop for ferromagnets—Survey of misconceptions and misinterpretations," *Am. J. Phys.*, vol.

71, no. 10, pp. 1080–1083, 2003, doi: 10.1119/1.1583696.

[49] R. Skomski and D. J. Sellmyer, "Anisotropy of rare-earth magnets," *J. Rare Earths*, vol. 27, no. 4, pp. 675–679, 2009.

[50] "Magnetic Anisotropy." [Online]. Available: https://cse.umn.edu/irm/3-magnetic-anisotropy. [Accessed: 12-Aug-2021].

[51] MITOPENCOURSEWARE, "Hysteresis in Ferromagnetic Materials." [Online]. Available: https://ocw.mit.edu/courses/materials-science-and-engineering/3-024-electronic-optical-and-magnetic-properties-of-materials-spring-2013/lecture-notes/MIT3_024S13_2012lec25.pdf. [Accessed: 12-Aug-2021].

[52] S. Zhang and D. Zhao, *Advances in Magnetic Materials: Processing, Properties, and Performance*. CRC Press, 2017.

[53] D. Brown, B. M. Ma, and Z. Chen, "Developments in the processing and properties of NdFeb-type permanent magnets," *J. Magn. Magn. Mater.*, vol. 248, no. 3, pp. 432–440, 2002, doi: 10.1016/S0304-8853(02)00334-7.

[54] S. Zhang and D. Zhao, *Advances in Magnetic Materials*. 2017.

[55] G. H. Yan, R. J. Chen, Y. Ding, S. Guo, D. Lee, and A. R. Yan, "The preparation of sintered NdFeB magnet with high-coercivity and high temperature-stability," *J. Phys. Conf. Ser.*, vol. 266, no. 1, pp. 1–6, 2011, doi: 10.1088/1742-6596/266/1/012052.

[56] V. P. Menushenkov and A. G. Savchenko, "Effects of post-sintering annealing on magnetic properties of Nd-Fe-B sintered magnets," *J. Magn. Magn. Mater.*, vol. 258–259, pp. 558–560, 2003, doi: 10.1016/S0304-8853(02)01144-7.

[57] W. F. Li, T. Ohkubo, K. Hono, and M. Sagawa, "The origin of coercivity decrease in fine grained Nd-Fe-B sintered magnets," *J. Magn. Magn. Mater.*, vol. 321, no. 8, pp. 1100–1105, 2009, doi: 10.1016/j.jmmm.2008.10.032.

[58] T. Takeshita and R. Nakayama, "Magnetic properties and microstructures of the Nd-Fe-B magnet powder produced by hydrogen treatment," in *Proceedings of the 10th International Workshop on Rare Earth Magnets and Their Applications*, 1989, pp. 551–554.

[59] P. J. McGuiness, X. J. Zhang, X. J. Yin, and I. R. Harris, "Hydrogenation, disproportionation and desorption (HDD): An effective processing route for NdFeB-type magnets," *J. Less-Common Met.*, vol. 158, no. 2, pp. 359–365, 1990, doi: 10.1016/0022-5088(90)90071-Q.

[60] P. J. McGuiness, X. J. Zhang, H. Forsyth, and I. R. Harris, "Disproportionation in Nd16Fe76B8-type hydrides," *J. Less-Common Met.*, vol. 162, no. 2, pp. 379–387, 1990, doi: 10.1016/0022-5088(90)90353-L.

[61] T. Takeshita and K. Morimoto, "Anisotropic Nd-Fe-B bonded magnets made from HDDR powders (invited)," *J. Appl. Phys.*, vol. 79, no. 8 PART 2A, pp. 5040–5044, 1996, doi: 10.1063/1.361567.

[62] R. Nakayama, T. Takeshita, M. Itakura, N. Kuwano, and K. Oki, "Microstructures and crystallographic orientation of crystalline grains in anisotropic Nd-Fe-Co-B-(Ga or Zr) magnet powders produced by the hydrogenation-decomposition-desorption-recombination process," *J. Appl. Phys.*, vol. 76, no. 1, pp. 412–417, 1994, doi: 10.1063/1.357091.

[63] T. Takeshita and R. Nakayama, “Proceedings of the 10th International Workshop on Rare Earth Magnets and Their Applications,” 1989, p. 551.

[64] R. S. Sheridan, R. S. Sheridan, A. J. Williams, I. R. Harris, and A. Walton, “Improved HDDR processing route for production of anisotropic powder from sintered NdFeB type magnets Journal of Magnetism and Magnetic Materials Improved HDDR processing route for production of anisotropic powder from sintered NdFeB type magnets,” *J. Magn. Magn. Mater.*, vol. 350, no. January, pp. 114–118, 2014, doi: 10.1016/j.jmmm.2013.09.042.

[65] H. Nakamura, S. Sugimoto, T. Tanaka, M. Okada, and M. Homma, “Effects of additives on hydrogenation , disproportionation , desorption and recombination phenomena in Nd2Fe14B compounds,” vol. 222, pp. 136–140, 1995.

[66] G. Yi, J. N. Chapman, D. N. Brown, and I. R. Harris, “TEM studies of the e ! ects of Zr additions on some HDDR-processed , high boron , NdFeB-type powders and hot-pressed magnets,” vol. 220, pp. 115–123, 2000.

[67] P. J. Mcguiness and S. Kobe, “ADAPTING THE HDDR PROCESS AND NdFeB-BASED PERMANENT-MAGNET ALLOYS FOR FACTORY PRODUCTION,” vol. 35, no. 5, pp. 231–236, 2001.

[68] Y. Honkura, C. Mishima, N. Hamada, G. Drazic, and O. Gutfleisch, “Texture memory effect of Nd – Fe – B during hydrogen treatment,” vol. 291, pp. 1282–1285, 2005, doi: 10.1016/j.jmmm.2004.11.423.

[69] S. Sugimoto, O. Gutfleisch, and I. R. Harris, “Resistivity measurements on hydrogenation disproportionation desorpfion recombination phenomena in Nd-Fe-B alloys with Co, Ga and Zr additions,” vol. 260, pp. 284–291, 1997.

[70] R. W. Jech, T. J. Moore, T. K. Glasgow, and N. W. Orth, “Rapid Solidification Via Melt Spinning: Equipment and Techniques,” *JOM J. Miner. Met. Mater. Soc.*, vol. 36, no. 4, pp. 41–45, 1984, doi: 10.1007/BF03338425.

[71] E. J. Lavernia and T. S. Srivatsan, “The rapid solidification processing of materials: Science, principles, technology, advances, and applications,” *J. Mater. Sci.*, vol. 45, no. 2, pp. 287–325, 2010, doi: 10.1007/s10853-009-3995-5.

[72] T. Y. Chu, L. Rabenberg, and R. K. Mishra, “Evolution of the microstructure of rapidly solidified Nd-Fe-B permanent magnets,” *J. Appl. Phys.*, vol. 69, no. 8, pp. 6046–6048, Apr. 1991, doi: 10.1063/1.347765.

[73] A. I. Gusev, “Melt spinning technique.” [Online]. Available: https://eng.thesaurus.rusnano.com/wiki/article3657.

[74] F. E. Luborsky, *Amorphous Metallic Alloys*. Elsevier, 1983.

[75] D. J. Brangan, T. A. Hyde, C. H. Sellers, and R. W. McCallum, “Developing rare earth permanent magnet alloys for gas atomization,” *J. Phys. D. Appl. Phys.*, no. 29, pp. 2376–2385, 1996.

[76] T. Srivatsan and T. Sudarshan, *Rapid Solidification Technology: An Engineering Guide*. 1993.

[77] L. H. Lewis, C. H. Sellers, and V. Panchanathan, “Phase composition and magnetic characteristics of inert gas-atomized RE-Fe-B-based powders,” vol. 31, no. 6, pp. 3641–3643, 1995.

[78] V. E. Martin, C. E. Reitlinger, G. Wolf, E. Schubert, and H. W. Bergmann, “Hard

magnetic Nd-Fe-B powders produced by liquid gas atomization," vol. 158, pp. 51–53, 1996.

[79] J. Pérez-arbulu, N. Burgos, and J. M. Martín, "Optimisation of a Compression Moulding Process for Isotropic Bonded NdFeB Magnets Starting from Gas Atomised Powders," 2016.

[80] O. Gutfleisch, "Controlling the properties of high energy density permanent magnetic materials by different processing routes," *J. Phys. D. Appl. Phys.*, vol. 33, no. 17, 2000, doi: 10.1088/0022-3727/33/17/201.

[81] J. Ormerod, "Bonded Magnets: A versatile class of Permanent Magnets," 2015. [Online]. Available: https://magneticsmag.com/bonded-magnets-a-versatile-class-of-permanent-magnets/. [Accessed: 18-Mar-2021].

[82] G. C. Hadjipanayis, *Bonded Magnets*. 2003.

[83] D. Brown, "Recent development in bonded NdFeB magnets," vol. 8853, no. February, 2002, doi: 10.1016/S0304-8853(01)00609-6.

[84] S. Sugimoto, "Current status and recent topics of rare-earth permanent magnets," *J. Phys. D. Appl. Phys.*, vol. 44, no. 6, 2011, doi: 10.1088/0022-3727/44/6/064001.

[85] L. Li *et al.*, "Fabrication of highly dense isotropic Nd-Fe-B nylon bonded magnets via extrusion-based additive manufacturing," *Addit. Manuf.*, vol. 21, no. December 2017, pp. 495–500, 2018, doi: 10.1016/j.addma.2018.04.001.

[86] J. K. Sonber, C. Subramanian, T. S. R. C. Murthy, R. C. Hubli, and A. K. Suri, "Processing Methods for Ultra-High Temperature Ceramics," in *MAX Phases and Ultra-High Temperature Ceramics for Extreme Environments*, no. June 2016, Engineering Science Reference, 2013, pp. 181–202.

[87] M. Suarez *et al.*, "Challenges and Opportunities for Spark Plasma Sintering: A Key Technology for a New Generation of Materials," *Sinter. Appl.*, no. November 2017, 2013, doi: 10.5772/53706.

[88] P. Cavaliere, *Spark plasma sintering of materials: Advances in processing and applications*. 2019.

[89] J. Trapp, A. Semenov, M. Nöthe, T. Wallmersperger, and B. Kieback, "Fundamental principles of spark plasma sintering of metals: part III–densification by plasticity and creep deformation," *Powder Metall.*, vol. 63, no. 5, pp. 329–337, 2020, doi: 10.1080/00325899.2020.1834748.

[90] J. Trapp and B. Kieback, "Fundamental principles of spark plasma sintering of metals: part I–Joule heating controlled by the evolution of powder resistivity and local current densities," *Powder Metall.*, vol. 62, no. 5, pp. 297–306, 2019, doi: 10.1080/00325899.2019.1653532.

[91] Z. H. Zhang, Z. F. Liu, J. F. Lu, X. B. Shen, F. C. Wang, and Y. D. Wang, "The sintering mechanism in spark plasma sintering - Proof of the occurrence of spark discharge," *Scr. Mater.*, vol. 81, pp. 56–59, 2014, doi: 10.1016/j.scriptamat.2014.03.011.

[92] K. Inoue, "Electric discharge heat treatment of metals in electrolytes," US3198675, 1965.

[93] K. R. Anderson, J. R. Groza, M. Fendorf, and C. J. Echer, "Surface oxide debonding in field assisted powder sintering," *Mater. Sci. Eng. A*, vol. 270, no. 2, pp. 278–282,

1999, doi: 10.1016/S0921-5093(99)00197-5.

[94] N. Chawake, L. D. Pinto, A. K. Srivastav, K. Akkiraju, B. S. Murty, and R. S. Kottada, "On Joule heating during spark plasma sintering of metal powders," *Scr. Mater.*, vol. 93, pp. 52–55, 2014, doi: 10.1016/j.scriptamat.2014.09.003.

[95] T. Voisin, J. P. Monchoux, and A. Couret, *Near-net shaping of titanium-aluminum jet engine turbine blades by SPS*, no. July 2020. 2019.

[96] R. W. Lee, "Hot-pressed neodymium-iron-boron magnets," *Appl. Phys. Lett.*, vol. 46, no. 8, pp. 790–791, 1985, doi: 10.1063/1.95884.

[97] Y. H. Hou, Y. L. Huang, Z. W. Liu, D. C. Zeng, S. C. Ma, and Z. C. Zhong, "Hot deformed anisotropic nanocrystalline NdFeB based magnets prepared from spark plasma sintered melt spun powders," *Mater. Sci. Eng. B Solid-State Mater. Adv. Technol.*, vol. 178, no. 15, pp. 990–997, 2013, doi: 10.1016/j.mseb.2013.06.009.

[98] M. Korent *et al.*, "Magnetic properties and microstructure evolution of hot-deformed Nd-Fe-B magnets produced by low-pressure spark-plasma sintering," *J. Magn. Magn. Mater.*, vol. 515, no. July, pp. 2–7, 2020, doi: 10.1016/j.jmmm.2020.167279.

[99] R. K. Mishra, "Microstructure of hot-pressed and die-upset NdFeB magnets," *J. Appl. Phys.*, vol. 62, no. 3, pp. 967–971, 1987, doi: 10.1063/1.339709.

[100] K. Uestuener, M. Katter, and W. Rodewald, "Dependence of the Mean Grain Size and Coercivity of Sintered Nd-Fe-B Magnets on the Initial Powder Particle Size," *IEEE Trans. Magn.*, vol. 42, no. 10, pp. 2897–2899, 2006, doi: 10.1109/TMAG.2006.879889.

[101] R. K. Mishra, E. G. Brewer, and R. W. Lee, "Grain growth and alignment in hot deformed Nd-Fe-B magnets," *J. Appl. Phys.*, vol. 63, no. 8, pp. 3528–3530, 1988, doi: 10.1063/1.340731.

[102] M. Leonowicz and H. A. Davies, "Effect of Nd content on induced anisotropy in hot deformed FeNdB magnets," *Mater. Lett.*, vol. 19, no. 5–6, pp. 275–279, 1994, doi: 10.1016/0167-577X(94)90170-8.

[103] L. Liu *et al.*, "Coercivity enhancement of hot-deformed Nd-Fe-B magnets by the eutectic grain boundary diffusion process," *J. Alloys Compd.*, vol. 666, pp. 432–439, 2016, doi: 10.1016/j.jallcom.2015.12.227.

[104] Z. W. Liu *et al.*, "Microstructure and property evolution of isotropic and anisotropic NdFeB magnets fabricated from nanocrystalline ribbons by spark plasma sintering and hot deformation," *J. Phys. D. Appl. Phys.*, vol. 44, no. 2, 2011, doi: 10.1088/0022-3727/44/2/025003.

[105] W. Q. Liu *et al.*, "Structure and magnetic properties of magnetically isotropic and anisotropic Nd-Fe-B permanent magnets prepared by spark plasma sintering technology," *J. Appl. Phys.*, vol. 107, no. 9, pp. 1–4, 2010, doi: 10.1063/1.3339067.

[106] J. E. Krentz, R. W. Lee, and R. A. Waldo, "Die-upset rare-earth iron-boron ingot: Coercivity dependence on composition and heat treatment," *J. Appl. Phys.*, vol. 70, no. 10, pp. 6474–6476, 1991, doi: 10.1063/1.349935.

[107] J. Liu *et al.*, "Effect of Nd content on the microstructure and coercivity of hot-deformed Nd-Fe-B permanent magnets," *Acta Mater.*, vol. 61, no. 14, pp. 5387–5399, 2013, doi: 10.1016/j.actamat.2013.05.027.

[108] C. Jin *et al.*, "Mechanical Properties Study of Hot-Pressed and Hot-Deformed Nd-

Fe-B Magnets," vol. 50, no. 11, pp. 2–5, 2014.

[109] D. Li, S. Suzuki, T. Kawasaki, and K. I. Machida, "Grain interface modification and magnetic properties of Nd-Fe-B sintered magnets," *Jpn. J. Appl. Phys.*, vol. 47, no. 10 PART 1, pp. 7876–7878, 2008, doi: 10.1143/JJAP.47.7876.

[110] M. Yue, M. Tian, J. X. Zhang, D. T. Zhang, P. L. Niu, and F. Yang, "Microstructure and magnetic properties of anisotropic Nd-Fe-B magnets produced by spark plasma sintering technique," *Mater. Sci. Eng. B Solid-State Mater. Adv. Technol.*, vol. 131, no. 1–3, pp. 18–21, 2006, doi: 10.1016/j.mseb.2005.11.010.

[111] J. Pyrhönen, J. Nerg, P. Kurronen, J. Puranen, and M. Haavisto, "Permanent magnet technology in wind power generators," *19th Int. Conf. Electr. Mach. ICEM 2010*, no. September, 2010, doi: 10.1109/ICELMACH.2010.5608312.

[112] D. Prosperi *et al.*, "Performance comparison of motors fitted with magnet-to-magnet recycled or conventionally manufactured sintered NdFeB," *J. Magn. Magn. Mater.*, vol. 460, pp. 448–453, 2018, doi: 10.1016/j.jmmm.2018.04.034.

[113] R. T. Nguyen, D. D. Imholte, A. C. Matthews, and W. D. Swank, "NdFeB content in ancillary motors of U.S. conventional passenger cars and light trucks: Results from the field," *Waste Manag.*, vol. 83, pp. 209–217, 2019, doi: 10.1016/j.wasman.2018.11.017.

[114] J. Li *et al.*, "Coercivity and its thermal stability of Nd–Fe–B hot-deformed magnets enhanced by the eutectic grain boundary diffusion process," *Acta Mater.*, vol. 161, pp. 171–181, 2018, doi: 10.1016/j.actamat.2018.09.018.

[115] S. Sugimoto *et al.*, "Effect of the disproportionation and recombination stages of the HDDR process on the inducement of anisotropy in Nd-Fe-B magnets," *J. Alloys Compd.*, vol. 293, pp. 862–867, 1999, doi: 10.1016/S0925-8388(99)00376-X.

[116] V. V. Volkov and Y. Zhu, "Magnetic structure and microstructure of die-upset hard magnets RE13.75Fe80.25B6 (RE=Nd, Pr): A possible origin of high coercivity," *J. Appl. Phys.*, vol. 85, no. 6, pp. 3254–3263, 1999, doi: 10.1063/1.369668.

[117] R. Madugundo, D. Salazar-Jaramillo, J. Manuel Barandiaran, and G. C. Hadjipanayis, "Coercivity Enhancement of Nanostructured NdFeB Magnets by Grain Boundary Engineering," *J. Magn. Magn. Mater.*, vol. 400, no. March 2015, pp. 300–303, 2016, doi: 10.1016/j.jmmm.2015.07.019.

[118] M. Soderžnik, B. Ambrožič, K. Žagar Soderžnik, and M. Korent, "Limits of grain boundary engineering in nanocrystalline Nd-Fe-B melt-spun ribbons," *Mater. Lett.*, vol. 264, pp. 20–22, 2020, doi: 10.1016/j.matlet.2020.127338.

[119] H. Sepehri-Amin *et al.*, "Microstructure and magnetic properties of grain boundary modified recycled Nd-Fe-B sintered magnets," *J. Alloys Compd.*, vol. 694, pp. 175–184, 2017, doi: 10.1016/j.jallcom.2016.09.305.

[120] H. Sepehri-Amin, Y. Une, T. Ohkubo, K. Hono, and M. Sagawa, "Microstructure of fine-grained Nd-Fe-B sintered magnets with high coercivity," *Scr. Mater.*, vol. 65, no. 5, pp. 396–399, 2011, doi: 10.1016/j.scriptamat.2011.05.006.

[121] F. Vial, F. Joly, E. Nevalainen, M. Sagawa, K. Hiraga, and K. T. Park, "Improvement of coercivity of sintered NdFeB permanent magnets by heat treatment," *J. Magn. Magn. Mater.*, vol. 242–245, pp. 1329–1334, 2002, doi: 10.1016/S0304-8853(01)00967-2.

[122] T. G. Woodcock and O. Gutfleisch, "Multi-phase EBSD mapping and local texture analysis in NdFeB sintered magnets," *Acta Mater.*, vol. 59, no. 3, pp. 1026–1036, 2011, doi: 10.1016/j.actamat.2010.10.033.

[123] A. Kirchner, J. Thomas, O. Gutfleisch, D. Hinz, K. H. Müller, and L. Schultz, "HRTEM studies of grain boundaries in die-upset Nd-Fe-Co-Ga-B magnets," *J. Alloys Compd.*, vol. 365, no. 1–2, pp. 286–290, 2004, doi: 10.1016/S0925-8388(03)00661-3.

[124] T. D. Nguyen, K. M. Krishnan, L. H. Lewis, Y. Zhu, and D. O. Welch, "Microstructure and composition in rapidly quenched NdFeB-based hard magnet alloys," *J. Appl. Phys.*, vol. 79, no. 8 PART 2A, pp. 4848–4850, 1996, doi: 10.1063/1.361630.

[125] H. Sepehri-Amin, T. Ohkubo, and K. Hono, "The mechanism of coercivity enhancement by the grain boundary diffusion process of Nd-Fe-B sintered magnets," *Acta Mater.*, vol. 61, no. 6, pp. 1982–1990, 2013, doi: 10.1016/j.actamat.2012.12.018.

[126] M. Soderžnik, M. Korent, K. Žagar Soderžnik, M. Katter, K. Üstüner, and S. Kobe, "High-coercivity Nd-Fe-B magnets obtained with the electrophoretic deposition of submicron TbF3 followed by the grain-boundary diffusion process," *Acta Mater.*, vol. 115, pp. 278–284, 2016, doi: 10.1016/j.actamat.2016.06.003.

[127] Z. Samardžija, P. McGuiness, M. Soderžnik, S. Kobe, and M. Sagawa, "Microstructural and compositional characterization of terbium-doped Nd-Fe-B sintered magnets," *Mater. Charact.*, vol. 67, pp. 27–33, 2012, doi: 10.1016/j.matchar.2012.02.017.

[128] H. Nakamura, K. Hirota, T. Minowa, and M. Honshima, "Magnetic properties of extremely small Nd-Fe-B sintered magnet," *INTERMAG ASIA 2005 Dig. IEEE Int. Magn. Conf.*, vol. 41, no. 10, p. 476, 2005, doi: 10.1109/intmag.2005.1463904.

[129] M. Soderžnik, K. Ž. Rožman, S. Kobe, and P. McGuiness, "The grain-boundary diffusion process in Nd-Fe-B sintered magnets based on the electrophoretic deposition of DyF 3," *Intermetallics*, vol. 23, pp. 158–162, 2012, doi: 10.1016/j.intermet.2011.11.014.

[130] K. Hirota, H. Nakamura, T. Minowa, and M. Honshima, "Coercivity Enhancement by the Grain Boundary Diffusion Process to Nd-Fe-B Sintered Magnets," *IEEE Trans. Magn.*, vol. 42, no. 10, pp. 2909–2911, 2006, doi: 10.1109/TMAG.2006.879906.

[131] N. Watanabe, M. Itakura, N. Kuwano, D. Li, S. Suzuki, and K. I. Machida, "Microstructure analysis of sintered Nd-Fe-B magnets improved by Tb-vapor sorption," *Mater. Trans.*, vol. 48, no. 5, pp. 915–918, 2007, doi: 10.2320/matertrans.48.915.

[132] J. Liu *et al.*, "Grain size dependence of coercivity of hot-deformed Nd-Fe-B anisotropic magnets," *Acta Mater.*, vol. 82, pp. 336–343, 2015, doi: 10.1016/j.actamat.2014.09.021.

[133] R. Ramesh, G. Thomas, and B. M. Ma, "Magnetization reversal in nucleation controlled magnets. II. Effect of grain size and size distribution on intrinsic coercivity of Fe-Nd-B magnets," *J. Appl. Phys.*, vol. 64, no. 11, pp. 6416–6423, 1988, doi: 10.1063/1.342055.

[134] P. Nothnagel, K. H. Müller, D. Eckert, and A. Handstein, "The influence of particle size on the coercivity of sintered NdFeB magnets," *J. Magn. Magn. Mater.*, vol. 101, no. 1–3, pp. 379–381, 1991, doi: 10.1016/0304-8853(91)90786-A.

[135] H. Sepehri-Amin, T. Ohkubo, T. Nishiuchi, S. Hirosawa, and K. Hono, "Coercivity enhancement of hydrogenation-disproportionation-desorption- recombination processed Nd-Fe-B powders by the diffusion of Nd-Cu eutectic alloys," *Scr. Mater.*, vol. 63, no. 11, pp. 1124–1127, 2010, doi: 10.1016/j.scriptamat.2010.08.021.

[136] L. Liu *et al.*, "Coercivity enhancement of hot-deformed Nd-Fe-B magnets by the eutectic grain boundary diffusion process using Nd62Dy20Al18alloy," *Scr. Mater.*, vol. 129, pp. 44–47, 2017, doi: 10.1016/j.scriptamat.2016.10.020.

[137] P. Mcguiness *et al.*, "Replacement and Original Magnet Engineering Options (ROMEOs): A European Seventh Framework Project to Develop Advanced Permanent Magnets Without, or with Reduced Use of, Critical Raw Materials," *Jom*, vol. 67, no. 6, pp. 1306–1317, 2015, doi: 10.1007/s11837-015-1412-x.

[138] R. Ramesh and K. Srikrishna, "Magnetization reversal in nucleation controlled magnets. I. Theory," *J. Appl. Phys.*, vol. 64, no. 11, pp. 6406–6415, 1988, doi: 10.1063/1.342054.

[139] H. Kronmüller, "Theory of Nucleation Fields in Inhomogeneous Ferromagnets," *Phys. Status Solidi*, vol. 144, no. 1, pp. 385–396, 1987, doi: 10.1002/pssb.2221440134.

[140] H. Kronmuller, K.-D. Durst, and M. Sagawa, "Analysis of the magnetic hardening mechanism in RE-FeB permanent magnets," vol. 74, pp. 291–302, 1988.

[141] E. Adler and P. Hamann, "Contribution to the understanding of coercivity and its temperature dependence in sintered SmCo5 and Nd2Fe14B magnets," in *Proceedings of the 8th International Workshop on Rare Earth Magnets and their Applications*, 1985.

[142] M. Sagawa and S. Hirosawa, "COERCIVITY AND MICROSTRUCTURE OF R-Fe-B SINTERED PERMANENT MAGNETS," *Le J. Phys. Colloq.*, vol. 49, no. C8, pp. C8-617-C8-622, 1988, doi: 10.1051/jphyscol:19888282.

[143] M. Sagawa, "Development and prospect of the Nd-Fe-B sintered magnets," in *Proc. of the 21th Workshop on REPM and Their Applications*, 2010, pp. 183–186.

[144] M. Sagawa, "Toward ultimate Nd-Fe-B permanent magnets," in *Rare-earth Permanent Magnets and Their Applications*, 2012, p. 3.

[145] X. Tang, H. Sepehri-Amin, T. Ohkubo, and K. Hono, "Suppression of non-oriented grains in Nd-Fe-B hot-deformed magnets by Nb doping," *Scr. Mater.*, vol. 147, pp. 108–113, 2018, doi: 10.1016/j.scriptamat.2017.12.032.

[146] W. F. Li, T. Ohkubo, and K. Hono, "Effect of post-sinter annealing on the coercivity and microstructure of Nd-Fe-B permanent magnets," *Acta Mater.*, vol. 57, no. 5, pp. 1337–1346, 2009, doi: 10.1016/j.actamat.2008.11.019.

[147] G. Yan, P. J. McGuiness, J. P. G. Farr, and I. R. Harris, "Optimisation of the processing of Nd-Fe-B with dysprosium addition," *J. Alloys Compd.*, vol. 491, no. 1–2, pp. 20–24, 2010, doi: 10.1016/j.jallcom.2009.10.202.

[148] "Mineral Prices." [Online]. Available: https://mineralprices.com/rare-earth-metals/. [Accessed: 03-May-2021].

[149] M. Sagawa *et al.*, "Dependence of coercivity on the anisotropy field in the Nd

2Fe14B-type sintered magnets," *J. Appl. Phys.*, vol. 61, no. 8, pp. 3559–3561, 1987, doi: 10.1063/1.338725.

[150] K. Ž. Soderžnik *et al.*, "Microstructural insights into the coercivity enhancement of grain-boundary-diffusion-processed Tb-treated Nd-Fe-B sintered magnets beyond the core-shell formation mechanism," *J. Alloys Compd.*, vol. 864, p. 158915, 2021, doi: 10.1016/j.jallcom.2021.158915.

[151] U. M. R. Seelam, T. Ohkubo, T. Abe, S. Hirosawa, and K. Hono, "Faceted shell structure in grain boundary diffusion-processed sintered Nd-Fe-B magnets," *J. Alloys Compd.*, vol. 617, pp. 884–892, 2014, doi: 10.1016/j.jallcom.2014.07.166.

[152] T. H. Kim *et al.*, "Microstructure and coercivity of grain boundary diffusion processed Dy-free and Dy-containing Nd[sbnd]Fe[sbnd]B sintered magnets," *Acta Mater.*, vol. 172, pp. 139–149, 2019, doi: 10.1016/j.actamat.2019.04.032.

[153] T. H. Kim *et al.*, "Formation mechanism of Tb-rich shell in grain boundary diffusion processed Nd–Fe–B sintered magnets," *Scr. Mater.*, vol. 178, pp. 433–437, 2020, doi: 10.1016/j.scriptamat.2019.12.002.

[154] K. Loewe, D. Benke, C. Kübel, T. Lienig, K. P. Skokov, and O. Gutfleisch, "Grain boundary diffusion of different rare earth elements in Nd-Fe-B sintered magnets by experiment and FEM simulation," *Acta Mater.*, vol. 124, pp. 421–429, 2017, doi: 10.1016/j.actamat.2016.11.034.

[155] K. Löewe, C. Brombacher, M. Katter, and O. Gutfleisch, "Temperature-dependent Dy diffusion processes in Nd-Fe-B permanent magnets," *Acta Mater.*, vol. 83, pp. 248–255, 2015, doi: 10.1016/j.actamat.2014.09.039.

[156] N. Oono, M. Sagawa, R. Kasada, H. Matsui, and A. Kimura, "Production of thick high-performance sintered neodymium magnets by grain boundary diffusion treatment with dysprosium-nickel-aluminum alloy," *J. Magn. Magn. Mater.*, vol. 323, no. 3–4, pp. 297–300, 2011, doi: 10.1016/j.jmmm.2010.09.021.

[157] Y. Matsuura, S. Hirosawa, H. Yamamoto, S. Fujimura, M. Sagawa, and K. Osamura, "Phase diagram of the nd-fe-b ternary system," *Jpn. J. Appl. Phys.*, vol. 24, no. 8, pp. 635–637, 1985, doi: 10.1143/JJAP.24.L635.

[158] L. Liu *et al.*, "Coercivity enhancement of Nd-Fe-B hot-deformed magnets by the eutectic grain boundary diffusion process using Nd-Ga-Cu and Nd-Fe-Ga-Cu alloys," *AIP Adv.*, vol. 8, no. 5, pp. 1–8, 2018, doi: 10.1063/1.5006575.

[159] U. M. R. Seelam *et al.*, "Coercivity of the Nd-Fe-B hot-deformed magnets diffusion-processed with low melting temperature glass forming alloys," *J. Magn. Magn. Mater.*, vol. 412, pp. 234–242, 2016, doi: 10.1016/j.jmmm.2016.04.005.

[160] H. Sepehri-Amin, J. Liu, T. Ohkubo, K. Hioki, A. Hattori, and K. Hono, "Enhancement of coercivity of hot-deformed Nd-Fe-B anisotropic magnet by low-temperature grain boundary diffusion of Nd60Dy 20Cu20 eutectic alloy," *Scr. Mater.*, vol. 69, no. 9, pp. 647–650, 2013, doi: 10.1016/j.scriptamat.2013.07.011.

[161] X. Tang *et al.*, "Improved coercivity and squareness in bulk hot-deformed Nd–Fe–B magnets by two-step eutectic grain boundary diffusion process," *Acta Mater.*, 2020, doi: 10.1016/j.actamat.2020.11.021.

[162] T. G. Woodcock *et al.*, "Atomic-scale features of phase boundaries in hot deformed Nd-Fe-Co-B-Ga magnets infiltrated with a Nd-Cu eutectic liquid," *Acta Mater.*, vol.

77, pp. 111–124, 2014, doi: 10.1016/j.actamat.2014.05.045.

[163] H. Sepehri-Amin *et al.*, "High-coercivity ultrafine-grained anisotropic Nd-Fe-B magnets processed by hot deformation and the Nd-Cu grain boundary diffusion process," *Acta Mater.*, vol. 61, no. 17, pp. 6622–6634, 2013, doi: 10.1016/j.actamat.2013.07.049.

[164] M. Korent *et al.*, "A process for improving the magnetic properties of commercial Nd-Fe-B magnetic powder with a small proportion of intergranular phase and a process for producing polymer-bonded magnets from these magnetic powders," 2021.

[165] H. Sepehri-Amin, T. Ohkubo, M. Gruber, T. Schrefl, and K. Hono, "Micromagnetic simulations on the grain size dependence of coercivity in anisotropic Nd-Fe-B sintered magnets," *Scr. Mater.*, vol. 89, pp. 29–32, 2014, doi: 10.1016/j.scriptamat.2014.06.020.

[166] R. K. Mishra and R. W. Lee, "Microstructure, domain walls, and magnetization reversal in hot-pressed Nd-Fe-B magnets," *Appl. Phys. Lett.*, vol. 48, no. 11, pp. 733–735, 1986, doi: 10.1063/1.96704.

[167] M. M. Carnasciali, G. A. Costa, and E. A. Franceschi, "Phase equilibria in the Nd-Cu system," *J. Less-Common Met.*, vol. 92, no. 1, pp. 97–103, 1983, doi: 10.1016/0022-5088(83)90230-8.

[168] M. Korent *et al.*, "Postopek za izboljšanje magnetnih lastnosti magnetnih prahov MQP-B+ Nd-Fe-B z majhnim deležem intergranularne faze in postopek izdelave polimerno-vezanih magnetov iz teh magnetnih prahov," 2021.

[169] "Scanning Electron Microscopy." [Online]. Available: https://www.nanoscience.com/techniques/scanning-electron-microscopy/. [Accessed: 31-May-2021].

[170] S. Swapp, "Scanning Electron Microscopy (SEM)." [Online]. Available: https://serc.carleton.edu/research_education/geochemsheets/techniques/SEM.html. [Accessed: 31-May-2021].

[171] Y. I. Lee, G. Y. Huang, C. W. Shih, W. C. Chang, H. W. Chang, and J. S. You, "Coercivity enhancement in hot deformed Nd2Fe14B-type magnets by doping low-melting RCu alloys (R = Nd, Dy, Nd + Dy)," *J. Magn. Magn. Mater.*, vol. 439, pp. 1–5, 2017, doi: 10.1016/j.jmmm.2017.05.009.

[172] Y. H. Hou *et al.*, "Effects of Nd-rich phase on the improved properties and recoil loops for hot deformed Nd-Fe-B magnets," *Acta Mater.*, vol. 115, pp. 385–391, 2016, doi: 10.1016/j.actamat.2016.06.015.

[173] Q. Liu *et al.*, "Coercivity optimization of hot-deformed Nd-Fe-B magnets by addition of B19.23Fe80.77 particles," *J. Magn. Magn. Mater.*, vol. 498, no. November 2019, p. 166254, 2020, doi: 10.1016/j.jmmm.2019.166254.

[174] W. Tang, K. W. Dennis, M. J. Kramer, I. E. Anderson, and R. W. McCallum, "Studies of sintered MRE-Fe-B magnets by DyF 3 addition or diffusion treatment (MRE Nd y Dy)," *J. Appl. Phys.*, vol. 111, no. 7, pp. 1–4, 2012, doi: 10.1063/1.3679465.

[175] F. Chen, L. Zhang, Y. Jin, and Y. Cheng, "Simultaneous enhancement of the coercivity and remanence at high temperatures in a sintered Nd-Fe-B magnet after grain boundary diffusion with Dy60Co40 alloy," *Mater. Charact.*, vol. 144, no.

August, pp. 547–553, 2018, doi: 10.1016/j.matchar.2018.08.012.

[176] J. Li *et al.*, "On the temperature-dependent coercivities of anisotropic Nd-Fe-B magnet," *Acta Mater.*, vol. 199, pp. 288–296, 2020, doi: 10.1016/j.actamat.2020.08.040.

[177] X. Tang, S. Y. Song, J. Li, H. Sepehri-Amin, T. Ohkubo, and K. Hono, "Thermally-stable high coercivity Ce-substituted hot-deformed magnets with 20% Nd reduction," *Acta Mater.*, vol. 190, pp. 8–15, 2020, doi: 10.1016/j.actamat.2020.03.017.

[178] K. Žagar, A. Kocjan, and S. Kobe, "Magnetic and microstructural investigation of high-coercivity net-shape Nd-Fe-B-type magnets produced from spark-plasma-sintered melt-spun ribbons blended with DyF3," *J. Magn. Magn. Mater.*, vol. 403, pp. 90–96, 2016, doi: 10.1016/j.jmmm.2015.11.082.

[179] T. H. Kim *et al.*, "Anisotropic diffusion mechanism in grain boundary diffusion processed Nd-Fe-B sintered magnet," *Acta Mater.*, vol. 112, pp. 59–66, 2016, doi: 10.1016/j.actamat.2016.04.019.

[180] B. B. Straumal, A. A. Mazilkin, S. G. Protasova, G. Schütz, A. B. Straumal, and B. Baretzky, "Observation of Pseudopartial Grain Boundary Wetting in the NdFeB-Based Alloy," *J. Mater. Eng. Perform.*, vol. 25, no. 8, pp. 3303–3309, 2016, doi: 10.1007/s11665-015-1872-8.

[181] B. B. Straumal *et al.*, "Grain boundary phenomena in NdFeB-based hard magnetic alloys," *Rev. Adv. Mater. Sci.*, vol. 38, no. 1, pp. 17–28, 2014.

[182] J. Yu *et al.*, "A controllability investigation of magnetic properties for FePt alloy nanocomposite thin films," *Nanomaterials*, vol. 9, no. 1, pp. 1–9, 2019, doi: 10.3390/nano9010053.

[183] N. Tian, X. Zhang, C. You, H. Fu, and Q. Shen, "Crystallization and atomic diffusion behavior of high coercive Ta/Nd–Fe–B/Ta-based permanent magnetic thin film," *Appl. Phys. A Mater. Sci. Process.*, vol. 123, no. 6, pp. 1–5, 2017, doi: 10.1007/s00339-017-1038-7.

[184] W. Liu and Z. Zhang, "Anisotropic nanocomposite soft/hard multilayer magnets," *Chinese Phys. B*, vol. 26, no. 11, 2017, doi: 10.1088/1674-1056/26/11/117502.

[185] T. Akiya *et al.*, "Low temperature diffusion process using rare earth-Cu eutectic alloys for hot-deformed Nd-Fe-B bulk magnets," *J. Appl. Phys.*, vol. 115, no. 17, pp. 2013–2016, 2014, doi: 10.1063/1.4869062.

[186] J. Xie *et al.*, "Coercivity enhancement and thermal-stability improvement in the melt-spun NdFeB ribbons by grain boundary diffusion," *J. Magn. Magn. Mater.*, vol. 446, pp. 210–213, 2018, doi: 10.1016/j.jmmm.2017.08.047.

[187] T. Fujimoto and T. Mukai, "Oriented grain growth in rapidly quenched Nd-Fe-B ribbons," *J. Appl. Phys.*, vol. 70, no. 10, pp. 6588–6590, 1991, doi: 10.1063/1.349866.

[188] C. D. Fuerst and E. G. Brewer, "Enhanced coercivities in die-upset Nd-Fe-B magnets with diffusion-alloyed additives (Zn, Cu, and Ni)," *Appl. Phys. Lett.*, vol. 56, no. 22, pp. 2252–2254, 1990, doi: 10.1063/1.102934.

.

Bibliography

Publications Related to the Thesis

Journal Articles

M. Korent, M. Komelj, S. Šturm, K. Žužek Rožman, S. Kobe, K. Žagar and M. Soderžnik., "Magnetic properties and microstructure evolution of hot-deformed Nd-Fe-B magnets produced by low-pressure spark-plasma sintering", *Journal of Magnetism and Magnetic Materials*, vol. 515, pp.1-6, 2020.

-

M. Korent, M. Soderžnik, U. Ročnik. S. Drev, K. Žužek Rožman, S. Šturm, S. Kobe, K. Žagar Soderžnik, "Toward Low-Energy Spark-Plasma Sintering of Hot-Deformed Nd-B Magnets", *International Journal of Materials Science and Applications*, vol. 10, pp. 98-107, 2021.

M. Korent, Xin Tang, H. Sepehri-Amin, K. Hioki, K.Ž. Soderžnik, S. Kobe, A. Hattori, T. Ohkubo, K. Hono, "Significant coercivity enhancement of hot-deformed bulk magnets by two-step diffusion process using a minimal amount of Dy", *Scripta materialia,* vol 205., pp. 114207, 2021.

M. Soderžnik, B. Ambrožič, K. Žagar and M. Korent, "Limits of grain boundary engineering in nanocrystalline Nd-Fe-B melt-spun ribbons", *Materials letters*, vol. 264, pp. 127338-1-127338-3, 2020.

Patent

M. Korent, M. Soderžnik, U. Ročnik, K. Kosmač, Z. Samardžija, B. Saje, S. Kobe, "Postopek za izboljšanje magnetnih lastnosti prahov MQP-B+Nd-Fe-B z majhnim deležem intergranularne faze in postopek izdelave polimerno-vezanih magnetov iz teh magnetnih prahov". Patent application P-202100012, 2021.

Other Publications

Journal Articles

M. Soderžnik, M. Korent, K. Žagar, J.M. Dubois, P. Tozman, M. Venkatesan, J.M.D. COEY, S. KOBE, "Hot-compaction of $YCo_{4.8}Fe_{0.2}YCo_{4.8}Fe_{0.2}$ nanocrystals for metal-bonded magnets", *Journal of Magnetism and Magnetic Materials*, vol. 460, pp.401-408, 2018.

M. Soderžnik, M. Korent, K. Žagar, M. Katter, K. Üstüner, S. Kobe, "High-coercivity Nd-Fe-B magnets obtained with the electrophoretic deposition of submicron TbF_3 followed by the grain-boundary diffusion process", *Acta materialia*, vol. 115, pp.278-284, 2016.

Conference Paper

M. Soderžnik, M. Korent, S. Kobe, "The effect of diffusion process of heavy rare-earths on the magnetic properties of melt-spun Nd-Fe-B ribbons", Intermag, 24-28 April 2017, Dublin, Ireland. *Digest book*. Pp. 479, 2017.

M. Korent, K. Žagar, M. Soderžnik and S. Kobe, "Anisotropic nanocrystalline Nd-Fe-B magnets produced by spark plasma sintering", 10th Student Conference of the Jožef Stefan International Postgraduate School and 12th Day of Young Researchers (KMBO Conference), 10-11 May 2018, Piran, *Proceedings*, Ljubljana: Jožef Stefan International Postgraduate School: Jožef Stefan Institute, pp. 45, 2018.

M. Korent, K. Žagar, M. Soderžnik and S. Kobe, "Hot-deformed Nd-Fe-B magnets produced by SPS", The European School of Magnetism (ESM-2018), 17-28 September 2018, Krakow: Academic Centre for Materials and Nanotechnology, 2018.

M. Korent, K. Žagar, M. Soderžnik, "Effect of deformation ratio on texture development in hot-deformed Nd-Fe-B magnets", 27th International Conference on Materials and Technology, 16-18 October 2019, Portorož, Slovenia. *Programme and book abstracts.* Ljubljana: Inštitut za kovinske materiale in tehnologije, pp. 90, 2019.

M. Soderžnik, M. Korent, B. Saje, S. Kobe, "Infiltration effect on the coercivity of heavy Rare-Earth-Free Nd-Fe-B ribbons", 27th International Conference on Materials and Technology, 16-18 October 2019, Portorož, Slovenia. *Programme and book abstracts.* Ljubljana: Inštitut za kovinske materiale in tehnologije, pp. 166, 2019.

Biography

The author of this thesis Matic Korent was born on the 4th of February 1991 in Celje. He finished his B.Sc. study of Chemical Engineering in 2013 at Faculty of Chemistry and Chemical Engineering, Ljubljana, Slovenia. The research topic of his Bachelor Thesis was preparation and characterization of the method for oxide SOFC anode. He continued his M.Sc. at the Faculty of Chemistry and Chemical Engineering, Ljubljana, Slovenia, and finished it in 2017. The research topic of his Master Thesis was synthesis and characterization of butyl polyglucoside.

He enrolled in the doctoral study program Nanosciences and Nanotechnologies at the Jožef Stefan Postgraduate School in 2017. He is employed at the Department for Nanostructured Materials (K7) at Jožef Stefan Institute and researching under the supervision of dr. Kristina Žagar Soderžnik and prof. Spomenka Kobe.

He works on various topics with one common point melt-spun Nd-Fe-B powder. At the beginning, he shows a first author published paper, where an alternative way of producing a HD magnet with good magnetic properties using a low-pressure unconventional spark-plasma sintering technique. To understand the behavior of magnetic properties and microstructure evolution in initial stages of deformation process, a hot-deformed magnet with different deformation ratios were produced and their dependence of remanence on the deformation ratio was determined.

In another field of investigation, a LEP (low energy processing) and a HEP (high energy processing) hot-deformed magnets were processed using unconventional spark-plasma sintering technique, which is significantly lower energy consumption technique regarding the conventional hot-deformation processing method. We investigated the microstructural and magnetic properties of LEP and HEP HD magnets and performed detailed analytical comparison.

In a collaboration with NIMS and Daido in 2019, a second first author paper is presented, where we perform a two-step grain boundary diffusion process on thick hot-deformed Nd-Fe-B magnets. The significant enhancement of coercivity is achieved using minimal amount of Dy. The properties of the Dy-diffusion processed magnet in this work are close to the trend of Tb-diffusion processed sintered magnets and superior to that of commercial Dy-containing commercial sintered magnets, which makes the two-step diffusion process a significant step forward in terms of economic issue and shows great industrial interest.

In the scope of collaboration with Kolektor Group d.o.o and Kolektor KFH d.o.o in 2019 and 2020, he presents an invention which relates to the improvement of the magnetic properties (coercivity) of a commercial magnetic melt-spun Nd-Fe-B powder with a small intergranular phase fraction and a process for the production of polymer-bonded magnets by grain boundary diffusion of a low-temperature eutectic alloy.